NAVAL POSTGRADUATE SCHOOL

MONTEREY, CALIFORNIA

THESIS

COMPUTATIONAL ANALYSIS OF EFFECT OF TRANSIENT FLUID FORCE ON COMPOSITE STRUCTURES

by

Scott C. Knutton

December 2013

Thesis Advisor:	Young W. Kwon
Second Reader:	Garth V. Hobson

THIS PAGE INTENTIONALLY LEFT BLANK

REPORT DOCUMENTATION PAGE		Form Approved OMB No. 0704-0188

Public reporting burden for this collection of information is estimated to average 1 hour per response, including the time for reviewing instruction, searching existing data sources, gathering and maintaining the data needed, and completing and reviewing the collection of information. Send comments regarding this burden estimate or any other aspect of this collection of information, including suggestions for reducing this burden, to Washington headquarters Services, Directorate for Information Operations and Reports, 1215 Jefferson Davis Highway, Suite 1204, Arlington, VA 22202-4302, and to the Office of Management and Budget, Paperwork Reduction Project (0704-0188) Washington DC 20503.

1. AGENCY USE ONLY *(Leave blank)*	2. REPORT DATE December 2013	3. REPORT TYPE AND DATES COVERED Master's Thesis

4. TITLE AND SUBTITLE COMPUTATIONAL ANALYSIS OF EFFECT OF TRANSIENT FLUID FORCE ON COMPOSITE STRUCTURES	5. FUNDING NUMBERS
6. AUTHOR(S) Scott C. Knutton	
7. PERFORMING ORGANIZATION NAME(S) AND ADDRESS(ES) Naval Postgraduate School Monterey, CA 93943-5000	8. PERFORMING ORGANIZATION REPORT NUMBER
9. SPONSORING /MONITORING AGENCY NAME(S) AND ADDRESS(ES) N/A	10. SPONSORING/MONITORING AGENCY REPORT NUMBER

11. SUPPLEMENTARY NOTES The views expressed in this thesis are those of the author and do not reflect the official policy or position of the Department of Defense or the U.S. Government. IRB protocol number ____N/A____.

12a. DISTRIBUTION / AVAILABILITY STATEMENT Approved for public release; distribution is unlimited	12b. DISTRIBUTION CODE A

13. ABSTRACT (maximum 200 words)

This study investigated the peak pressure applied to a composite structure under various transient velocity profiles, fluid boundary conditions, as well as structural geometric configurations and material properties. Then, the resultant dynamic responses of the composite structures were investigated. The study was conducted by modeling fluid-structure interaction using the finite-element and finite-volume analysis technique. The results showed that the peak pressure and the resultant stresses in the composite structures are significantly dependent on the accelerating state as well as fluid boundary conditions. The peak stresses determined in this study were between three and 16 times larger than the steady state stress for the given fluid acceleration profile.

14. SUBJECT TERMS Fluid structure interaction, FSI, finite element, finite volume, ANSYS, E-glass, composite material, coupled interaction, Hamming, HPC, transient acceleration, transient fluid, transient velocity, transient stress.	15. NUMBER OF PAGES 125
	16. PRICE CODE

17. SECURITY CLASSIFICATION OF REPORT	18. SECURITY CLASSIFICATION OF THIS PAGE	19. SECURITY CLASSIFICATION OF ABSTRACT	20. LIMITATION OF ABSTRACT
Unclassified	Unclassified	Unclassified	UU

NSN 7540-01-280-5500

Standard Form 298 (Rev. 2-89)
Prescribed by ANSI Std. 239-18

THIS PAGE INTENTIONALLY LEFT BLANK

Approved for public release; distribution is unlimited

COMPUTATIONAL ANALYSIS OF EFFECT OF TRANSIENT FLUID FORCE ON COMPOSITE STRUCTURES

Scott C. Knutton
Lieutenant, United States Navy
B.S., New School University, 2006

Submitted in partial fulfillment of the
requirements for the degree of

MASTER OF SCIENCE IN MECHANICAL ENGINEERING

from the

NAVAL POSTGRADUATE SCHOOL
December 2013

Author: Scott C. Knutton

Approved by: Young W. Kwon
Thesis Advisor

Garth V. Hobson
Second Reader

Knox T. Millsaps
Chair, Department of Mechanical and Aerospace Engineering

THIS PAGE INTENTIONALLY LEFT BLANK

ABSTRACT

This study investigated the peak pressure applied to a composite structure under various transient velocity profiles, fluid boundary conditions, as well as structural geometric configurations and material properties. Then, the resultant dynamic responses of the composite structures were investigated. The study was conducted by modeling fluid-structure interaction using the finite-element and finite-volume analysis technique. The results showed that the peak pressure and the resultant stresses in the composite structures are significantly dependent on the accelerating state as well as fluid boundary conditions. The peak stresses determined in this study were between three and 16 times larger than the steady state stress for the given fluid acceleration profile.

THIS PAGE INTENTIONALLY LEFT BLANK

TABLE OF CONTENTS

I. INTRODUCTION....1
- A. OVERVIEW....1
- B. PREVIOUS RESEARCH....2
- C. OBJECTIVES....3

II. COMPUTER MODEL DEVELOPMENT....5

III. ANSYS VERIFICATION....7
- A. BASE MODEL COMPARISON AGAINST RIGID BODY MODEL....7
- B. BASE MODEL COMPARISON TO AN EMPIRICAL TEST....11

IV. COMPUTATIONAL MODELS....19
- A. BASE MODEL: CONSTANT ACCELERATION FOR 0.5 SECONDS....19
- B. VARIATION IN CONSTANT ACCELERATION....20
- C. VARIATION IN TERMINAL VELOCITY....21
- D. STEP ACCELERATION....22
- E. SIMULATED ACCELERATION....23
- F. GEOMETRIC VARIATION....24
- G. MATERIAL PROPERTY VARIATION....27
- H. DEPTH VARIATION....27

V. RESULTS....29
- A. BASE MODEL: CONSTANT ACCELERATION FOR 0.5 SECOND....29
- B. VARIATION IN CONSTANT ACCELERATION....34
- C. VARIATION IN TERMINAL VELOCITY....39
- D. STEP ACCELERATION....42
- E. SIMULATED ACCELERATION....47
- F. GEOMETRIC VARIATION....52
- G. MATERIAL PROPERTY VARIATION....58
- H. DEPTH VARIATION....63

VI. CONCLUSIONS AND RECOMMENDATIONS....73
- A. CONCLUSIONS....73
- B. RECOMMENDATIONS....75

APPENDIX A. BASE MODEL GENERATION....77

APPENDIX B. CFX-PRE SUPLEMENTAL FIGURES....83

APPENDIX C. SOLVING FSI SIMUATIONS WITH HPC....87
- A. HPC AND CPU COMPARISON....87
- B. SUBMITING ANSYS SIMULATIONS WITH FSI TO HPC....87

APPENDIX D. DEPTH VARIATION, NODAL DATA UPPER-MID, CENTER, LOWER-MID, AND LOWER....91

LIST OF REFERENCES....103

INITIAL DISTRIBUTION LIST....105

THIS PAGE INTENTIONALLY LEFT BLANK

LIST OF FIGURES

Figure 1. *USS Independence* (LCS-2) (from [1]). 1
Figure 2. Base Model at 0.09 sec. 8
Figure 3. Rigid Body at 0.09 sec. 8
Figure 4. Base Model at 0.58 sec. 9
Figure 5. Rigid Body at 0.58 sec. 9
Figure 6. Base Model at 2.0 sec. 10
Figure 7. Rigid Body at 2.0 sec. 10
Figure 8. Composite Plate Drag Force at 0.5 m/s Fluid Velocity. 12
Figure 9. Analytical Model Geometry with Rear View Callout. 13
Figure 10. Analytical Comparison Model Structural Mesh. 14
Figure 11. Analytical Comparison Model Fluid Mesh Cross-Section. 14
Figure 12. Analytical Comparison Model, CFX-Pre. 15
Figure 13. Analytical Plate Drag Force at 0.5 m/s Fluid Velocity. 16
Figure 14. Base Model Inlet Velocity Profile. 20
Figure 15. Variation in Constant Acceleration Inlet Velocity Profile. 21
Figure 16. Variation in Terminal Velocity Inlet Velocity Profile. 22
Figure 17. Step Acceleration Inlet Velocity Profile. 23
Figure 18. Simulated Acceleration Inlet Velocity Profile. 24
Figure 19. Cube, 0.5 Meter. 25
Figure 20. Cylinder, Flat Face. 26
Figure 21. Cylinder, Dome Face. 26
Figure 22. Cube at 2 Meters Depth. 28
Figure 23. Nodal Data Sample Locations. 29
Figure 24. Base Model 6-Node Strain Comparison. 30
Figure 25. Base Model Center Node Acceleration Versus Displacement. 32
Figure 26. Base Model, Pressure at Center Versus Average Pressure at Interface. 33
Figure 27. Variation in Constant Acceleration, Strain at Upper Node. 35
Figure 28. Variation in Constant Acceleration, Stress at Upper Node. 35
Figure 29. Variation in Constant Acceleration, Displacement at Center Node. 36
Figure 30. Variation in Constant Acceleration, Pressure at Center Node. 36
Figure 31. Variation in Constant Acceleration, Ratio Comparison. 38
Figure 32. Variation in Terminal Velocity, Strain at Upper Node. 39
Figure 33. Variation in Terminal Velocity, Stress at Upper Node. 39
Figure 34. Variation in Terminal Velocity, Displacement at Center node. 40
Figure 35. Variation in Terminal Velocity, Pressure at Center Node. 40
Figure 36. Variation in Terminal Velocity, Ratio Comparison. 42
Figure 37. Step Acceleration, Strain at Upper Node. 43
Figure 38. Step Acceleration, Stress at Upper Node. 43
Figure 39. Step Acceleration, Displacement at Center Node. 44
Figure 40. Step Acceleration, Pressure at Center Node. 44
Figure 41. Step Acceleration, Ratio Comparison. 47
Figure 42. Simulated Acceleration, Strain At Upper Node. 48

Figure 43. Simulated Acceleration, Stress At Upper Node. 48
Figure 44. Simulated Acceleration, Displacement At Center Node. 49
Figure 45. Simulated Acceleration, Pressure At Center Node. 49
Figure 46. Simulated Acceleration, Ratio Comparison. 51
Figure 47. Geometric Variation, Cube 0.5 Peak Stress Location. 53
Figure 48. Geometric Variation, Flat Face Peak Stress Location. 53
Figure 49. Geometric Variation, Cylinder Peak Stress Location. 54
Figure 50. Geometric Variation, Strain at Peak Node. 54
Figure 51. Geometric Variation, Stress at Peak Node. 55
Figure 52. Geometric Variation, Displacement at Center Node. 55
Figure 53. Geometric Variation, Pressure at Center Node. 56
Figure 54. Material Property Variation, Strain at Upper Node. 59
Figure 55. Material Property Variation, Stress at Upper Node. 59
Figure 56. Material Property Variation, Displacement at Center Node. 60
Figure 57. Material Property Variation, Pressure at Center Node. 60
Figure 58. Depth Variation, Nodal Evaluation Points. 63
Figure 59. Base Model, Peak Pressure with Interface Stress Callout. 64
Figure 60. 1-Meter Model, Peak Pressure with Interface Stress Callout. 65
Figure 61. 3-Meter Model, Peak Pressure with Interface Stress Callout. 65
Figure 62. Depth Variation, Strain at Upper Node. 66
Figure 63. Depth Variation, Stress at Upper Node. 66
Figure 64. Depth Variation, Displacement at Upper Node. 67
Figure 65. Depth Variation, Average Pressure at Interface. 67
Figure 66. Depth Variation, Normalized Interface Displacement. 70
Figure 67. Depth Variation, Ratio Comparison. 72
Figure 68. ANSYS Workbench, 2-Way FSI Connection. 77
Figure 69. E-Glass Engineering Data. 78
Figure 70. Base Model Geometry. 79
Figure 71. Transient Structural Mesh Configuration. 80
Figure 72. Transient Structural Mesh. 80
Figure 73. CFX Fluid Mesh. 81
Figure 74. Fluid Domain Interior-Exterior Interface. 82
Figure 75. CFX-Pre Analysis Basic Settings Tab. 83
Figure 76. CFX-Pre Interface FSIN Assignment. 84
Figure 77. CFX-Pre Interface Pressure Coefficient Setting. 85
Figure 78. CFX-Pre Solver Control Settings. 86
Figure 79. WinSCP Directory. 88
Figure 80. Example Script File. 89
Figure 81. Depth Variation, Strain at Upper-Mid Node. 91
Figure 82. Depth Variation, Stress at Upper-Mid Node. 91
Figure 83. Depth Variation, Displacement at Upper-Mid Node. 92
Figure 84. Depth Variation, Strain at Center Node. 92
Figure 85. Depth Variation, Stress at Center Node. 93
Figure 86. Depth Variation, Displacement at Center Node. 93
Figure 87. Depth Variation, Strain at Lower-Mid Node. 94

Figure 88. Depth Variation, Stress at Lower-Mid Node. 94
Figure 89. Depth Variation, Displacement at Lower-Mid Node.....95
Figure 90. Depth Variation, Strain at Lower Node. 95
Figure 91. Depth Variation, Stress at Lower Node. 96
Figure 92. Depth Variation, Displacement at Lower Node.....96

THIS PAGE INTENTIONALLY LEFT BLANK

LIST OF TABLES

Table 1. Analytical to Empirical Drag Force Comparison. 16
Table 2. Variation in Material Property. 27
Table 3. Base Model 6-Node Evaluation. 31
Table 4. Base Model Hydrodynamic Evaluation. 33
Table 5. Variation in Constant Acceleration, Case Summary. 37
Table 6. Variation in Terminal Velocity, Case Summary.....41
Table 7. Step Acceleration, Case Summary.....45
Table 8. Simulated Acceleration, Case Summary.....50
Table 9. Geometric Variation, Case Summary. 57
Table 10. Material Property Variation, Case Summary.....61
Table 11. Depth Variation, Stress and Strain Ratio Case Summary.....68
Table 12. Depth Variation, Displacement Case Summary. 69
Table 13. Depth Variation, Average Pressure at Interface Case Summary. 69
Table 14. Depth Variation, Centerline Displacement Area (mm^2). 71
Table 15. Depth Variation, Upper Node Case Summary.....97
Table 16. Depth Variation, Upper-Mid Node Case Summary.....98
Table 17. Depth Variation, Center Node Case Summary. 99
Table 18. Depth Variation, Lower-Mid Node Case Summary. 100
Table 19. Depth Variation, Lower Node Case Summary. 101

THIS PAGE INTENTIONALLY LEFT BLANK

LIST OF ACRONYMS AND ABBREVIATIONS

CAD	computer aided drafting
CFD	computational fluid dynamics
CPU	central processing unit
FEM	finite element method
FSI	fluid-structure interaction
HPC	high performance computing
LCS	littoral combat ship
LPD	landing platform dock
MAE	Mechanical and Aerospace Engineering
NPS	Naval Postgraduate School
UTS	ultimate tensile strength
UUV	unmanned underwater vehicle

THIS PAGE INTENTIONALLY LEFT BLANK

ACKNOWLEDGMENTS

While there are countless people responsible for my success at the Naval Postgraduate School (NPS), there are a few who deserve special credit. I would like to give my sincerest gratitude to Distinguished Professor Young Kwon. I first met Dr. Kwon during my course work, at which time he sparked my interests in solid mechanics. He eagerly viewed my non-technical background as an opportunity to mold me into a competent engineer, and I will always be grateful for that. His guidance and insight were instrumental to my success and he gave me free reign to explore different areas while keeping me on schedule. I would also like to thank Professor Garth Hobson for providing the necessary insight into the effective use of computational fluid dynamics (CFD) software, which formed the cornerstone of my graduate studies. Thank you to the faculty and staff of the Department of Mechanical and Aerospace Engineering for their diligent efforts in helping me acquire the critical thinking skills unique to an engineer. Their guidance has allowed me to thrive at the Naval Postgraduate School and provide a level of expertise vital to my future career as a Surface Warfare Officer.

Additionally, I would like to thank our east coast families who missed out on precious time with our infant daughter and endured the separation inherent to being on the other side of the country. Finally, I would like to my wife, Rachel, for patiently enduring long nights with the bedroom lights on and the grueling weekend hours required throughout this undertaking. She consistently made life fun even during the most stressful times and her promise to be the best wife, mother and friend anyone could ask for never wavered and for that I am forever grateful. Her support, insight and the thought provoking conversations we shared were the most important component in my success.

THIS PAGE INTENTIONALLY LEFT BLANK

I. INTRODUCTION

A. OVERVIEW

The Navy is seeking radical new vessel designs to meet high-speed and shallow-draft requirements that enable littoral zone operations. While propulsion systems play an obvious role in determining velocity, hull performance is equally as important. Standard Arleigh Burke class destroyer hull designs have deep drafts that reduce maximum speed and prevent entering more shallow waters. The U.S. Navy has developed the littoral combat ship (LCS) class specifically to operate in the littorals [1]. The *USS Independence* (LCS-2) is the second ship in its class but with the unique configuration of an all-aluminum trimaran hull (Figure 1).

Figure 1. *USS Independence* (LCS-2) (from [1]).

The U.S. Navy has experimented with aluminum and composite materials in its surface fleet since the 1970s, including the Avenger class mine countermeasures force and Ticonderoga class cruisers. However, these cruisers (and other classes) have experienced cracking throughout the aluminum superstructure resulting in costly repairs and reduced operational readiness. Aluminum has greater flexibility and corrosion resistance than steel but also has lower yield strength. LCS-2 was commissioned in 2010 and already has well-documented galvanic corrosion failures occurring where the aluminum hull meets components of the steel propulsion system. To address this

problem newer ships like the Zumwalt class DDG-1000 employ a composite-balsa wood superstructure similar to materials already in use in the San Antonio-class LPD.

Composite materials are generally less dense and therefore weigh less than metals. They are also less rigid and can have a Young's modulus below 150 GPa compared to steel whose value is 200 GPa. While there is a growing desire to increase use of composite materials in naval applications, these structures must still withstand the same hydraulic and impact forces withstood by steel and other commonly used materials. This poses a unique engineering challenge of designing a structure fabricated from a composite material to meet the rigorous demands of an open ocean vessel.

B. PREVIOUS RESEARCH

Mathematicians and finite element method (FEM) modelers alike have worked to find an accurate way to effectively model a fluid-structure interaction (FSI). One of the more common FSI solution methods utilizes an alternating solver that passes nodal data back and forth between fluid and structural domains. This represents a strongly coupled interaction that predicts the response of both domains with extreme precision and is the foundation for most FSI simulations.

Maritime, automotive, aeronautical and medical communities often encounter multi-physics problems that can best be solved using FSIs. Medical applications include the modeling of composite material blood vessels under continuous acceleration and deceleration of heart-induced blood flow, which causes transient stresses on the material [2]. Aeronautical research has used FSIs to model the forces induced on aircraft wings and resultant structural loading. Additionally, the automotive industry has countless applications such as the prediction of brake line expansion in motorcycles; however, fluid sloshing in tanker trucks is of particular interest to this study.

Tehrani, Rakheja and Sedaghati [3] reported that partially-filled tank trucks are at high risk for rollover due to the vehicle moments induced by transient hydraulic forces acting on tank walls. Their study focused on the peak forces created during transient fluid slosh compared to mean force values during the same transient. Although

dependent upon tank fill percentage, applied transient force and several other conditions, they concluded that peak transient forces could be as high as 1.57 times the mean transient force.

Water slam testing of composite materials is common in high-speed marine applications where lightweight vessels impact the surface while traveling at high velocities. Battley, Allen, Perhsen, Stenius and Rosen [4] conducted composite material drop tests to determine the maximum pressures applied. Their research on E-glass determined a maximum pressure of 250 kPa, well below the industry recognized ultimate tensile stress (UTS) of 100 MPa.

C. OBJECTIVES

The increased application of composite materials in U.S. Navy ships requires a detailed understanding of material response to a wide variety of forces. This study examined the hydrodynamic pressure loading on composite structures exposed to a fluid with transient acceleration. The objective of this study is to determine the hydrodynamic pressure loading on composite structures when the structures are in accelerating motions, as well as to examine the resultant stresses and strains in the structures. A series of parametric studies were conducted for various acceleration cases, deep or shallow water, structural geometric configurations and material properties using the finite element analysis of fluid-structure interaction.

THIS PAGE INTENTIONALLY LEFT BLANK

II. COMPUTER MODEL DEVELOPMENT

In this study a commercial program called ANSYS [5] was used for computational modeling. The fundamental analysis tool integrated within ANSYS is the finite element method (FEM), which divides the problem domain into smaller subdomains called finite elements. ANSYS offers an FSI tutorial [5] that details the basic steps necessary to configure a strongly coupled fluid – solid interaction, which was completed prior to designing the model used in this thesis.

The comparative base model used in this study was created using a process similar to the FSI Tutorial and detailed in Appendix A. The solid object used in the base model was a 1 m^3 box created using shell elements to simplify the mathematical problem and reduce simulation run times [2]. A hex-dominant structural mesh was used that had 3,458 nodes and 3,456 elements with an element length of 4.1 cm. The fluid domain was separated into inner and outer regions to ensure node-to-node connectivity at the FSI interface and resulted in 110,937 nodes and 100,744 elements.

Base model boundary conditions were set for full slip on all sides and zero surface roughness simulating an infinitely large fluid domain. Additional simulations had been completed to assess the influence of surface roughness. However, no significant differences in structural results were found and this variable was eliminated from this thesis.

The base model is founded upon a difference in relative motion. Unlike an actual ship whose motion moves through a presumed stationary fluid, the base model presents a stationary object in a moving fluid. A total time of 2 seconds with 0.01-second time step was used to allow accurate depiction of oscillatory response while reducing computational time.

Initial simulations were completed in the Naval Postgraduate School (NPS) Mechanical and Aeronautical Engineering (MAE) Department computer aided drafting (CAD) lab on a central processing unit (CPU) with Dual-Quad core, 2.13 GHz processors and 24 GB of RAM. However, the necessary time step and simulation time resulted in

excessive run times and large result files, which warranted use of NPS high performance computing (HPC) that facilitates use of node clusters to solve ANSYS simulations [6]. After a single comparative case was run on both HPC and a CPU that yielded identical results, HPC was used to complete all simulations completed during this research.

III. ANSYS VERIFICATION

FEM modeling is a powerful tool and expected step of most design methods, however without the proper input parameters, false results are possible. Prior to conducting an analysis, two separate methods were used to verify the model previously described in Chapter II. The first method was a side-by-side comparison of the base model with flexible interface to a modified base model with rigid interface. The second verification retained base model settings but involved an entirely new geometry to facilitate comparison with empirical data obtained by research at the Naval Postgraduate School.

A. BASE MODEL COMPARISON AGAINST RIGID BODY MODEL

The base model consisted of a one-meter cube fully submerged in fluid domain with full slip boundary conditions. The front face of the cube was an FSI side and allowed to flex when exposed to fluid flow, and the remaining five sides were set as rigid supports. However, in order to verify proper exchange of information between the structural and fluid domain solvers, a comparative rigid body model was considered. The rigid body model was an exact replica of the base model except for the inclusion of one additional rigid side, replacing the deformable side. The inlet velocity profile used in the base model was formulated from the equation $y = 4x$ for [0,0.5] seconds and then constant 2 m/s velocity until the simulation ended at 2 seconds.

After completing simulations for both trails, the base model center node yielded a maximum 45 mm inward displacement at 0.09 seconds, maximum 15 mm outward displacement at 0.58 seconds and a steady state 5 mm inward displacement at 2 seconds (Figure 2, 4 and 6). These local maximum and steady state displacement values should have the largest effect on fluid flow around the cube. The responses at time steps (0.09, 0.58 and 2 seconds) were then compared against the rigid body model at the same time steps (Figure 3, 5 and 7).

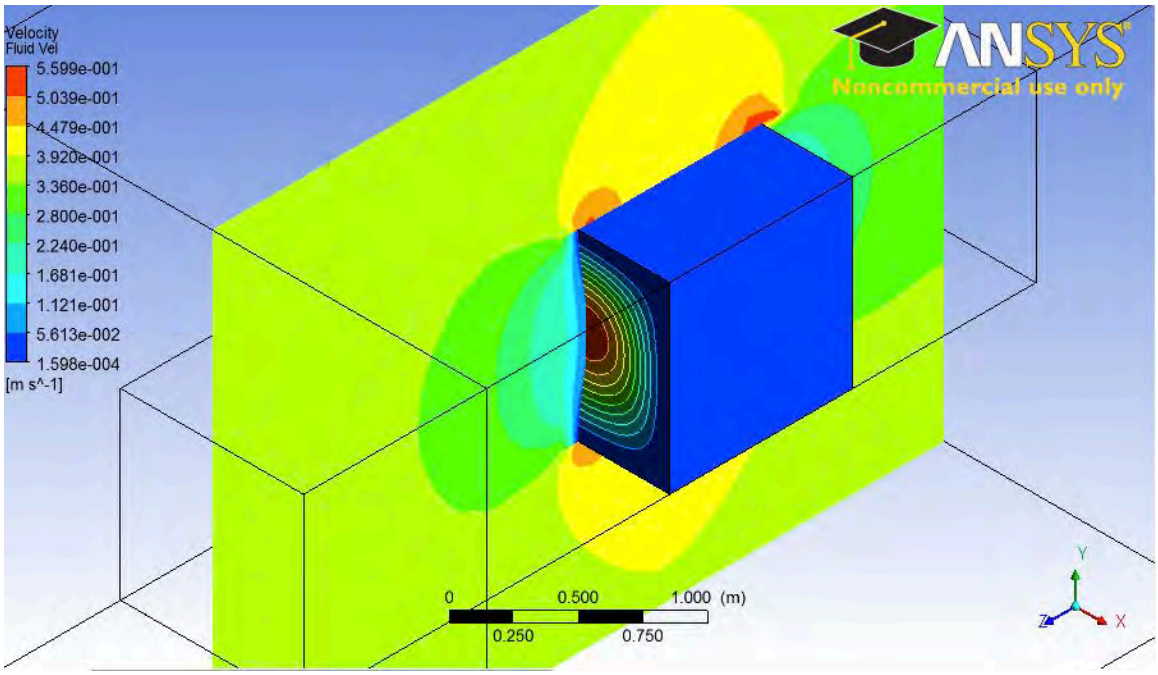

Figure 2. Base Model at 0.09 sec.

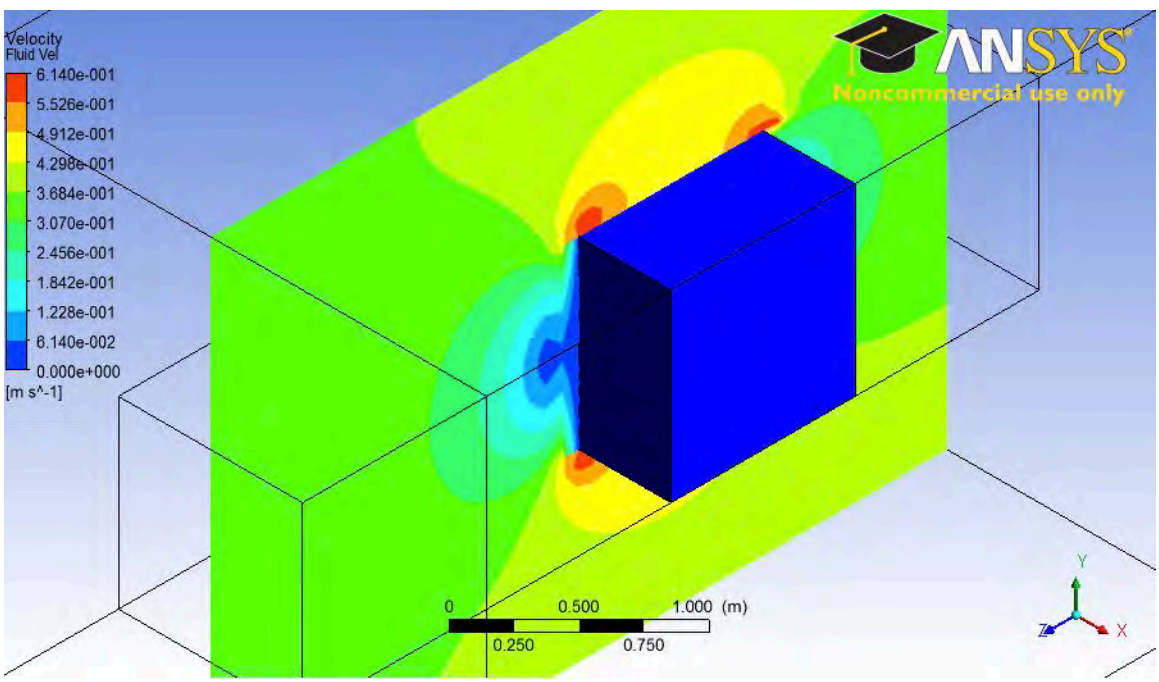

Figure 3. Rigid Body at 0.09 sec.

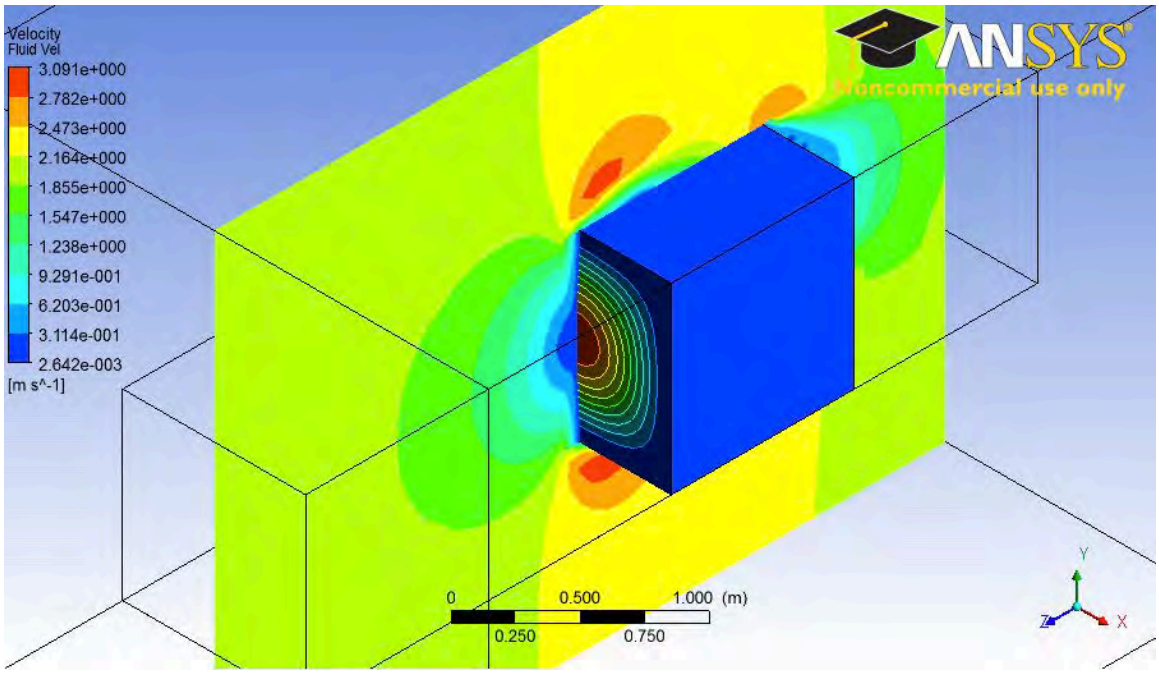

Figure 4. Base Model at 0.58 sec.

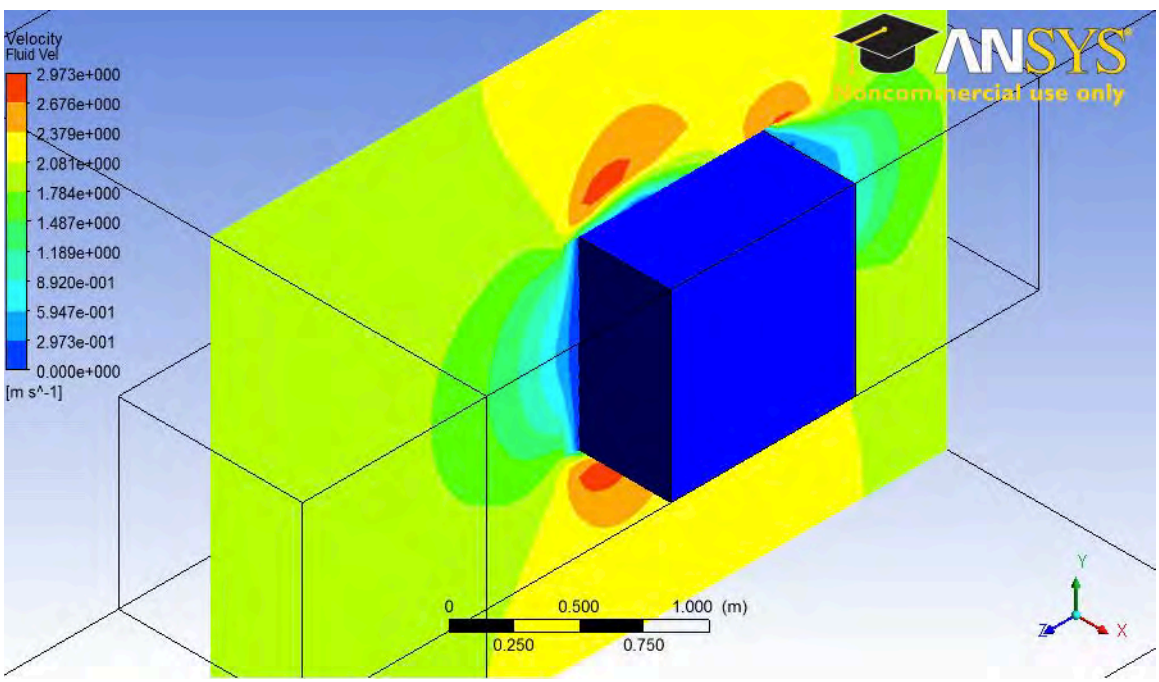

Figure 5. Rigid Body at 0.58 sec.

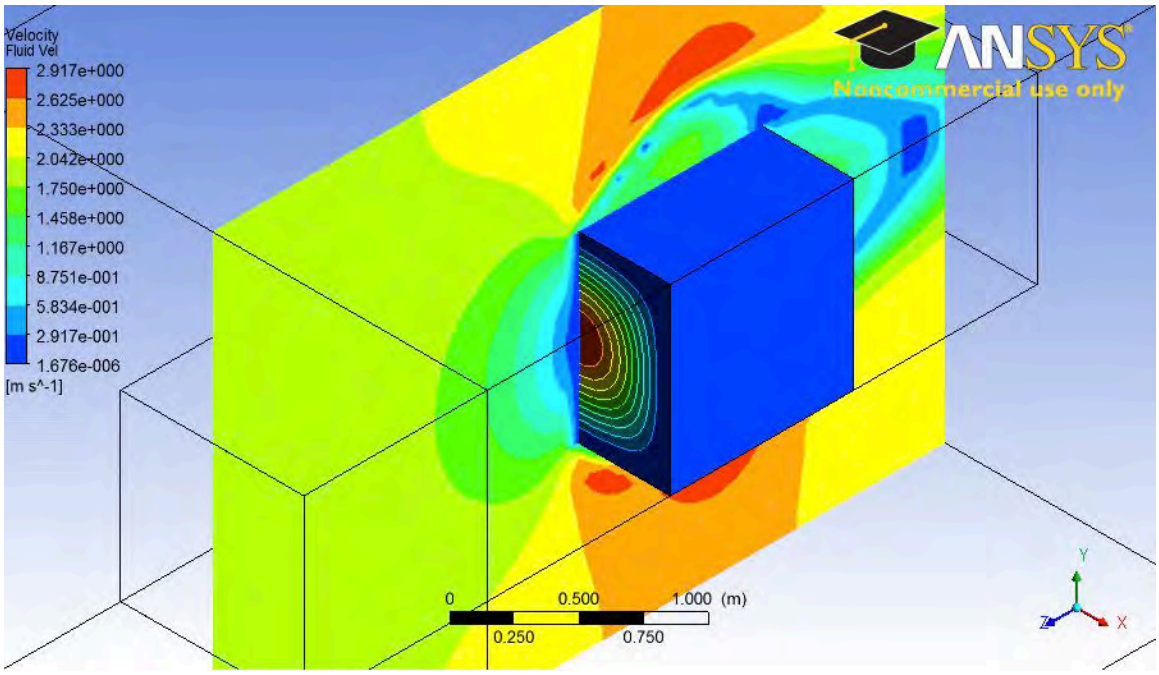

Figure 6. Base Model at 2.0 sec.

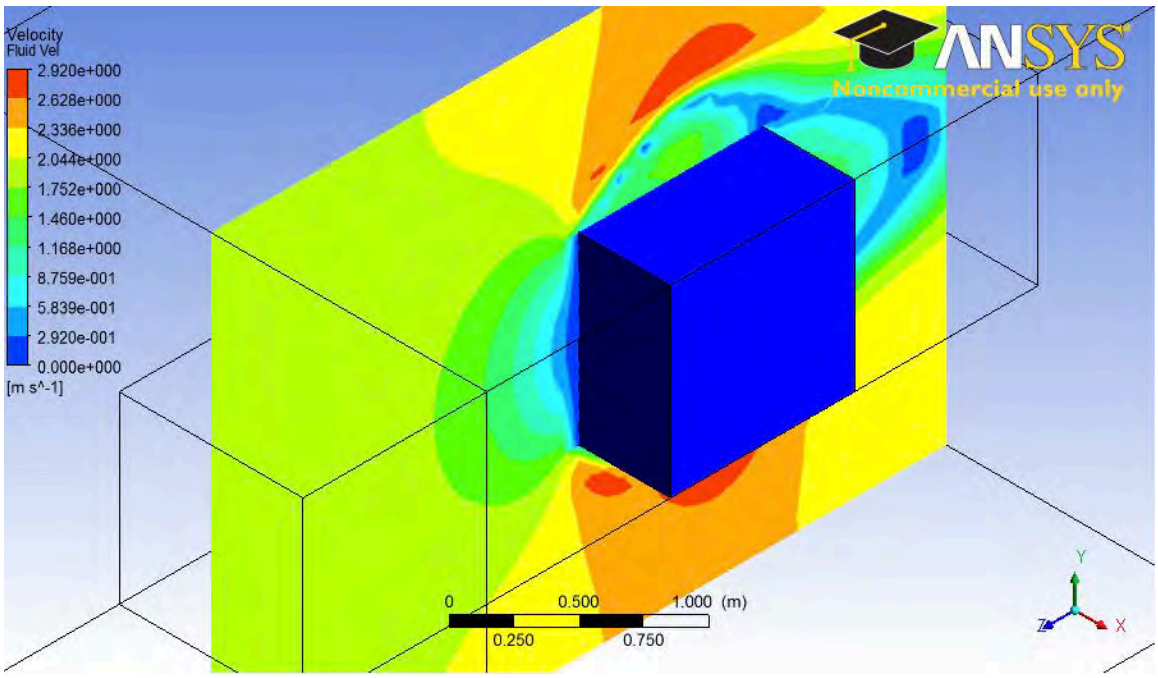

Figure 7. Rigid Body at 2.0 sec.

At the 0.09 second time step, the inward displacement of the base model deformable plate minimizes overall resistance on the upstream flow field and allows upstream fluid to progress at a faster average velocity of 0.36 m/s. The rigid body model had more resistance to upstream fluid flow and thus a greater impact on velocity. The rigid model upstream fluid velocity was 0.34 m/s and lower than the base (deformable) model.

The maximum outward displacement of the flexible plate occurred at the 0.58-second time step and gave the cube a slight streamlined effect that resulted in an average velocity around the cube of 2.32 m/s. The rigid body average fluid velocity around the cube at 0.58 seconds was 2.22 m/s and slower than the base (flexible) model.

The final time step compared occurred at 2 seconds under near steady state conditions. As expected, both fluid velocity profiles are virtually identical, with only minor velocity differences of approximately 0.002 m/s.

The differences between rigid and base models confirm the transfer of solution data between fluid and solid domains. The rigid body model prevented interface displacement and resulted in a change in fluid response. The comparative change in structural and fluid response validates the base model FSI.

B. BASE MODEL COMPARISON TO AN EMPIRICAL TEST

The Naval Postgraduate School utilizes a tow tank at its hydrodynamics laboratory for testing and research. The tow tank is 3 x 5 x 38 foot container that simulates open-water testing for a wide array of materials and configurations. A five horsepower motor pulls a carriage along the top of the tank exposing the object mounted below to equivalent speed fluid forces [7].

Another research project in progress at NPS evaluates the forces acting on a composite material plate exposed to a transient flow. In this evaluation, a 328 x 177.5 x 3 mm plate is comprised of 10 layers of E-glass and rigidly attached to the tow tank carriage assembly with a 26 x 2,178 x 26 mm aluminum bar that extended 26 mm past the top plane of the plate. A load cell affixed to the tow cable measures the forces

induced by the drag of the plate. Although the project by Millhouse [8] is ongoing, initial data has been obtained for the equivalent drag force of a 0.5 m/s velocity on the plate (Figure 8).

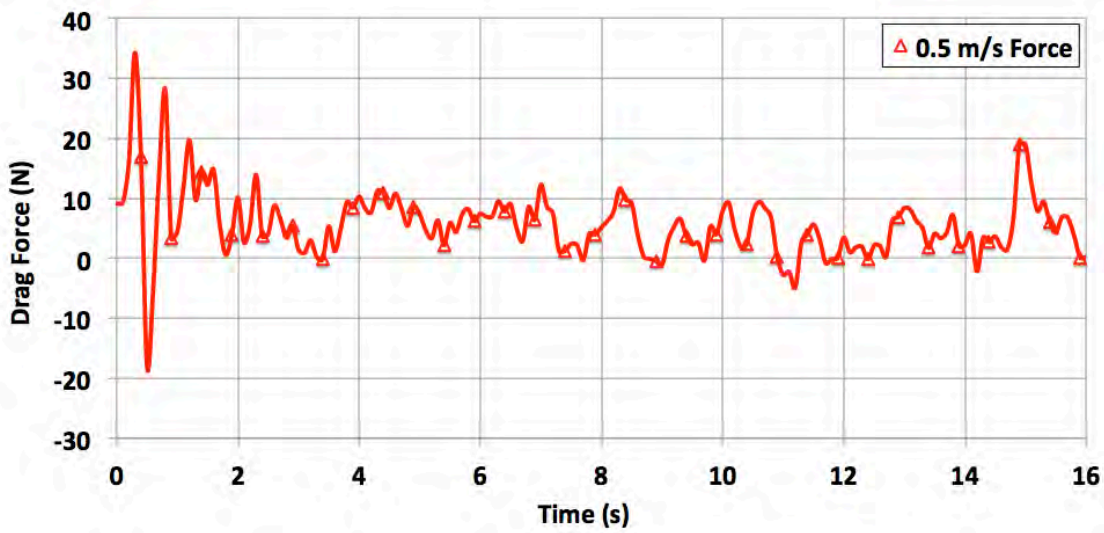

Figure 8. Composite Plate Drag Force at 0.5 m/s Fluid Velocity.

With project parameters fully defined, it was necessary to modify the base model to reflect the tow tank simulation. Using Design Modeler, the cube was replaced with a plate and aluminum support that matched the dimensions of the empirical test. Unlike the base model, which only had motion on one side and facilitated use of shell elements, this comparative model required a fully defined solid domain to determine motion on all sides. The fluid domain was extended to match tow tank width and overall height modified to reflect water depth and therefore negate drag of the support through air while simplifying the model. It was impractical to model the full length of the tow tank so the upstream length was sized to ensure fully developed flow conditions were achieved prior to plate contact. Lastly, the fluid domain was separated using a series of Boolean subtractions to facilitate using a hex dominant mesh.

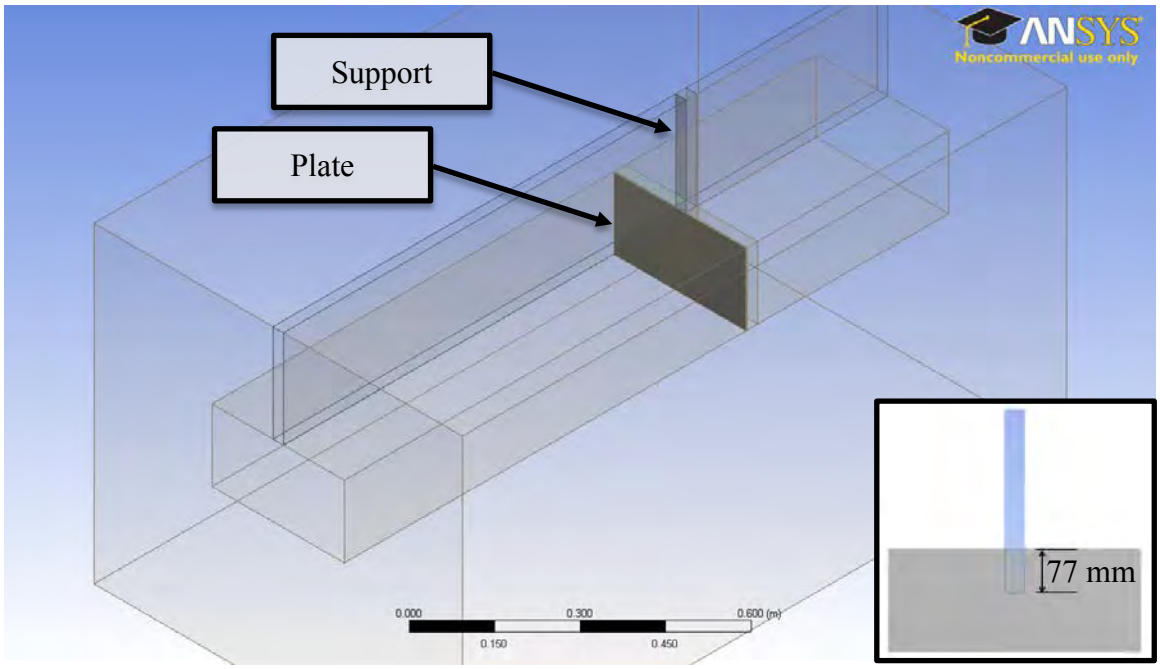

Figure 9. Analytical Model Geometry with Rear View Callout.

Meshing was completed using the same techniques as the base model (Appendix A) and was sized to facilitate node-to-node contact between all FSI interfaces. Utilizing a combined four-division sweep and 1 cm element face sizing methods, a hex-dominant structural mesh was created that resulted in a combined 2,844 nodes and 14,759 elements for both plate and support (Figure 10). The fluid mesh incorporated the same methods and sizing for all surfaces sharing an interface with the structural domain. Fluid surfaces in contact with the structural faces, as well as other boundaries were meshed with a hex-dominant sweep method, medium relevance sizing and default settings. The combined fluid mesh totaled 83,893 nodes and 45,220 elements (Figure 11).

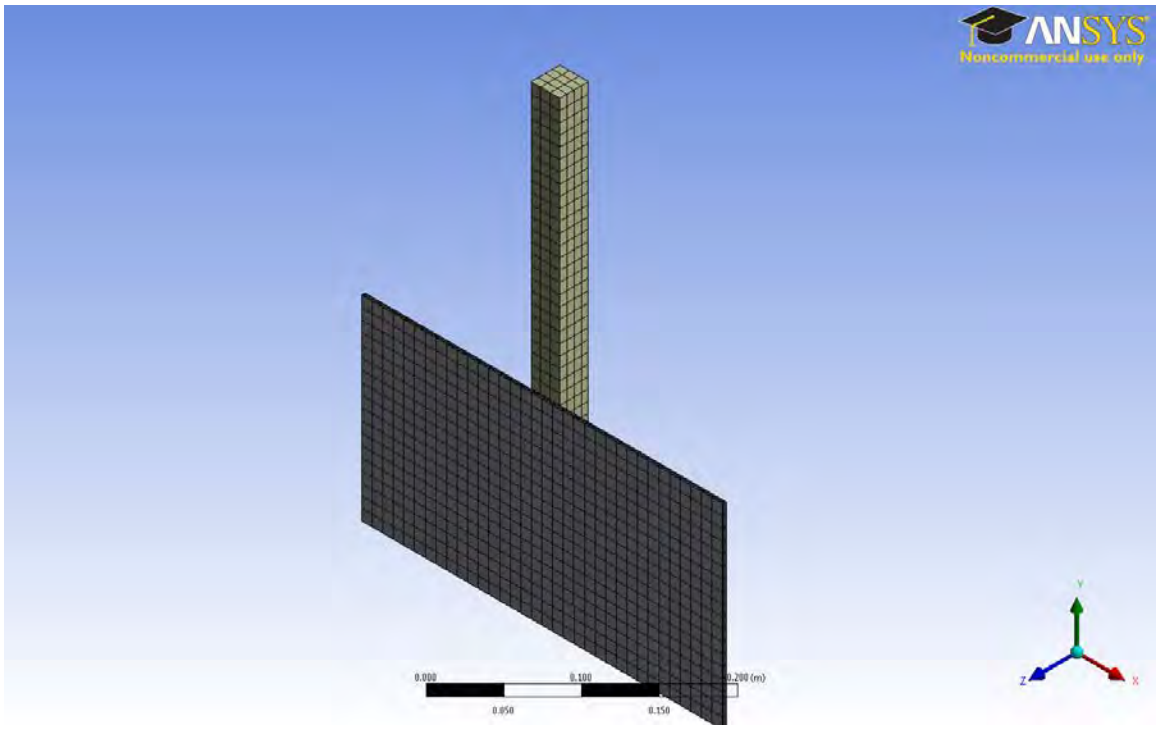

Figure 10. Analytical Comparison Model Structural Mesh.

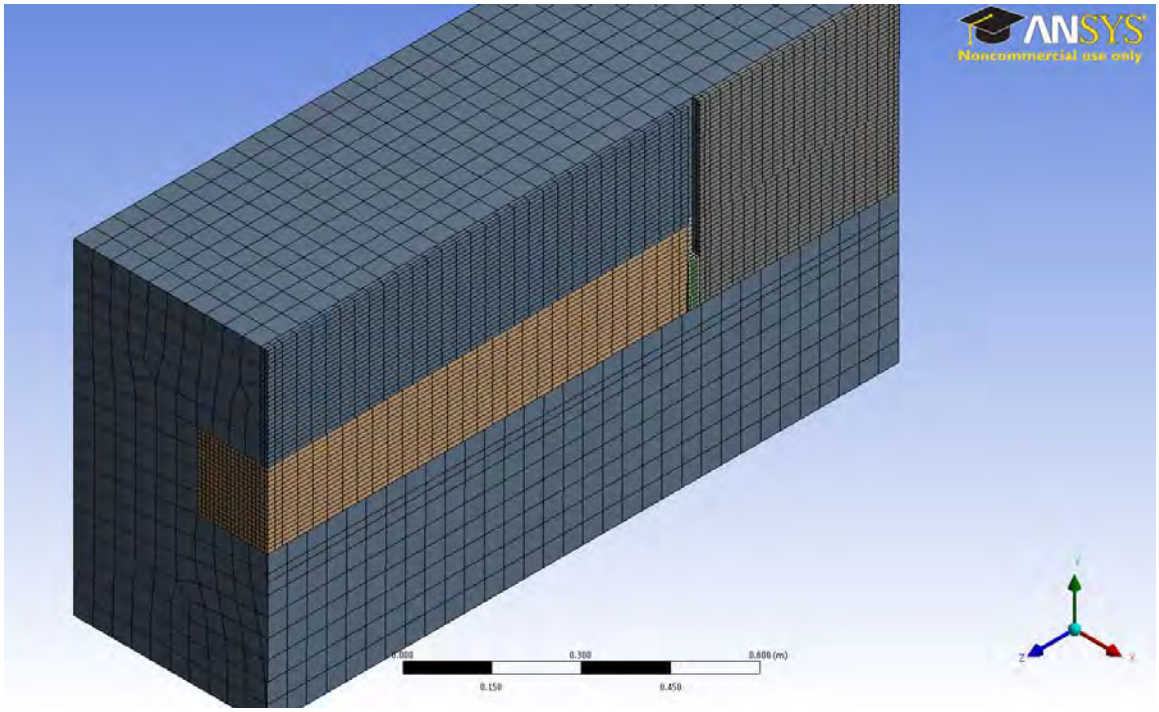

Figure 11. Analytical Comparison Model Fluid Mesh Cross-Section.

The final setup was completed in CFX-Pre and configured inlet and outlet boundaries and set a constant acceleration from 0 to 0.05 seconds and a constant 0.5 m/s velocity thereafter. Another significant difference between the base model and the analytical comparison model was the inclusion of a free surface. The top was configured to represent a free surface by setting the upper most fluid boundaries to be an opening with zero pressure (Figure 12). This model also retained the same 0.01-second time step as used in the base model.

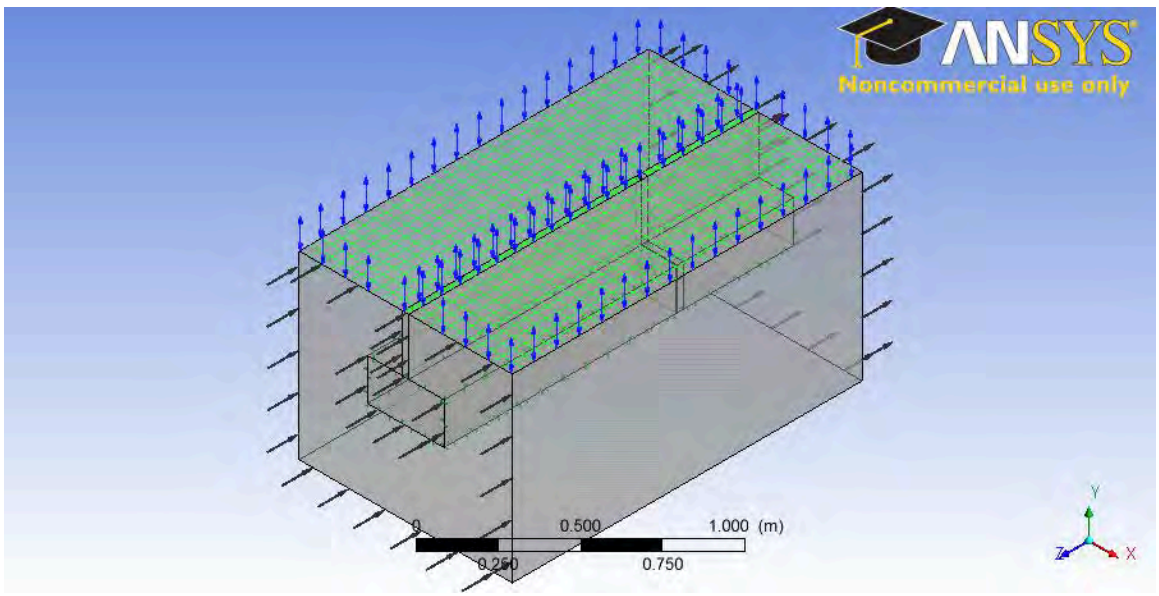

Figure 12. Analytical Comparison Model, CFX-Pre.

The simulation was then submitted to HPC where it was solved using a 12-node cluster with 8 GB of memory. Post processing was also completing with HPC using CFX-Post. Using the function calculator in CFX-Post, a drag force expression for the plate was made that allowed for plotting and evaluation. Drag force for the support was determined and found to be negligible by comparison. However, inclusion of the support allowed the entire plate to deflect which had a significant effect on drag and improved overall accuracy of this model. Since the tow tank carriage assembly load cell acts only in the horizontal plane, drag in the horizontal z-direction was determined and plotted against time (Figure 13).

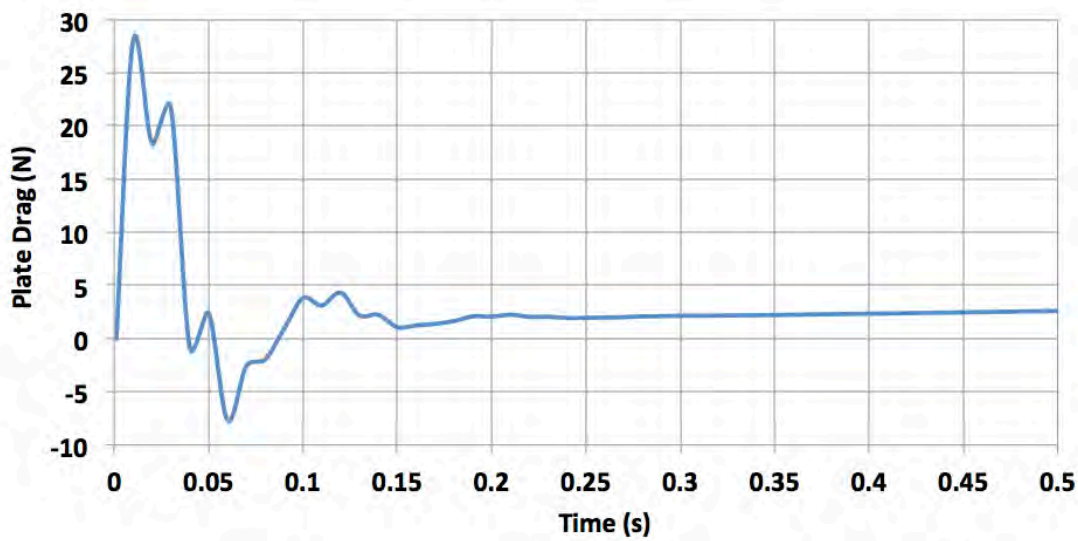

Figure 13. Analytical Plate Drag Force at 0.5 m/s Fluid Velocity.

The analytical results shown in Figure 13 show several oscillations followed by a steady increase in drag force values while the empirical results (Figure 8) seem to have more oscillations throughout the entire test run. However, both models captured a large initial peak in both positive and negative directions and similar steady state values (Table 1). Although the analytical and empirical drag force plots appear to be very different, comparing both analytical and empirical models shows similar results in maximum, minimum and steady state values. Even though the analytical model did not capture the precise oscillations, it predicted a transient peak drag force to within 20 percent. Additional data points from the empirical model were not available for review at this time.

Table 1. Analytical to Empirical Drag Force Comparison.

	Max. Transient (N)	Min. Transient (N)	Steady State (N)
Analytical Model	27.97	-7.66	5.44
Empirical Model	34.26	-17.99	4.85

The most likely cause for difference between the two models was the inlet velocity profile, which was unknown for the empirical test. It is virtually impossible for any motor to instantaneously achieve its final running speed, and even when it reaches that speed, there will be oscillations in final RPM until a steady state value is achieved. Also, plate deflection varies during the test, which affects drag and could affect motor response resulting in oscillations sensed by the load cell. The empirical model was also subject to wave action during the trial and friction losses from the track.

The analytical model could be improved with additional data from the empirical trial. A more accurate inlet velocity profile would dramatically improve results. This could easily be obtained with a high-speed camera and fixed length measurements along the tow tank.

Regardless of oscillation frequency, the empirical peak values were very similar to those calculated in the analytical model. The similarity between empirical and analytical models verifies the ability to accurately predict peak transient stresses for a composite material using computational modeling of FSIs.

THIS PAGE INTENTIONALLY LEFT BLANK

IV. COMPUTATIONAL MODELS

A. BASE MODEL: CONSTANT ACCELERATION FOR 0.5 SECONDS

To facilitate proper evaluation for a large spectrum of transient flow conditions and geometric variants, a base model was selected and analyzed. The base model started with the one-meter submerged cube detailed in Chapter II. Using shell elements for the structural domain, material properties of 2,000 kg/m^3 and 20 GPa were given for density and Young's modulus respectively. These properties were chosen as they well represent an E-glass fiber reinforced composite frequently used in research and industrial applications.

The fluid domain was sized sufficiently to ensure the development of the complete inlet velocity profile and to minimize interference from remaining sides of the fluid domain. The fluid domain extended one meter beyond the cube from the top, side and rear faces and two meters from the front face. Full-slip boundary conditions were also applied to all exterior surfaces of the fluid domain in order to further mitigate boundary layer effects from the fluid domain onto the cubic structure.

The base model considered transient fluid flow at the inlet under a constant acceleration for the first 0.5 seconds until a terminal velocity of 2 m/s was reached at which point the fluid velocity remained constant for the duration of the simulation (Figure 14). A time step size of 0.01 seconds was used for plotting the results. The inlet transient velocity profile, shown in Figure 14, yielded highly stable results and allowed for a wide range of variables without significant modifications to the ANSYS model between variations. Lastly, 2 m/s is an easily attainable test speed and could facilitate a comparison of analytical to empirical data.

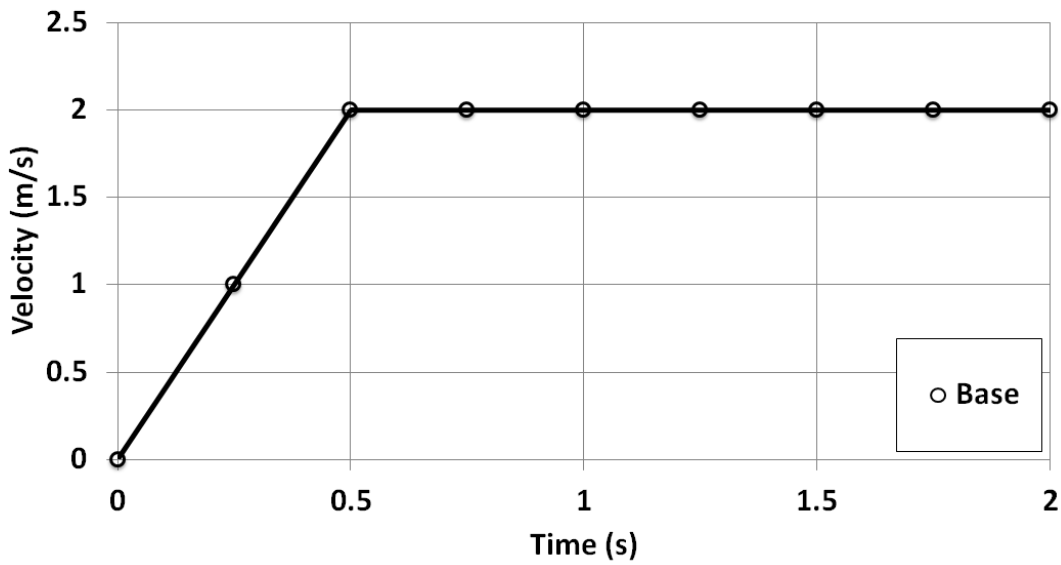

Figure 14. Base Model Inlet Velocity Profile.

B. VARIATION IN CONSTANT ACCELERATION

The inlet velocity profile used in the base model was formulated from the equation y = 4x for [0,0.5] seconds. As the first parametric study, it was necessary to establish the effects of different fluid acceleration rates on the composite material. Two cases were selected that increased and decreased the acceleration rate by a factor of two. The first case, 2 m/s at 0.25 seconds, represented a flow that was twice as fast as the base model. This was achieved by determining an inlet velocity profile from the equation y = 8x evaluated for [0,0.25] seconds until a maximum steady state speed of 2 m/s was achieved. The second case, 2 m/s at 1 second, was half as fast the base and modeled from the equation y = 2x evaluated for [0,1] seconds until a maximum steady state speed of 2 m/s. Figure 15 displays the inlet velocity profile for both acceleration variants and the base model.

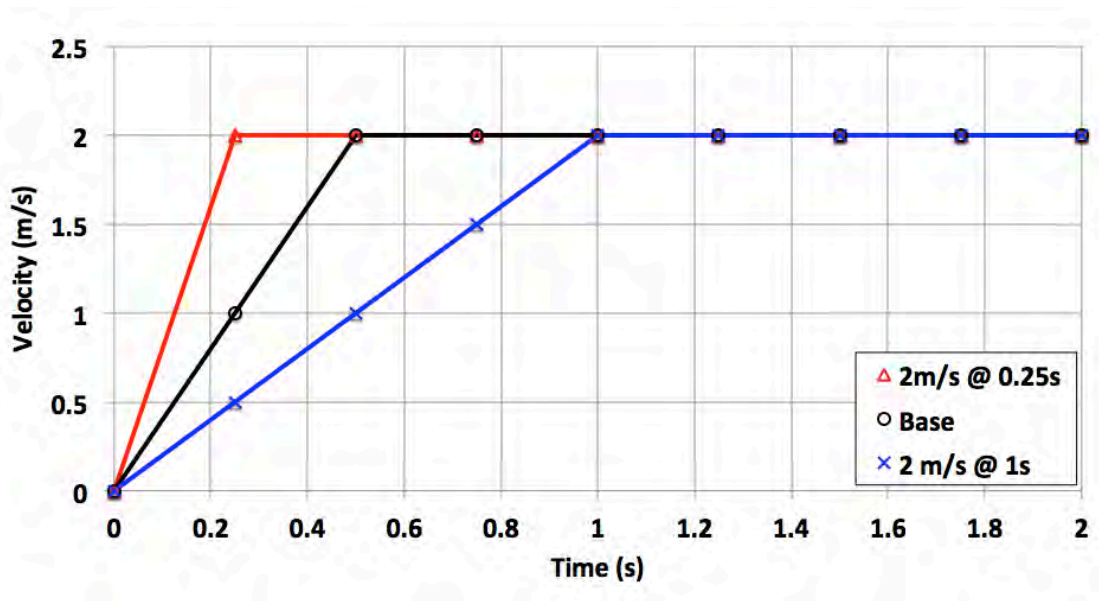

Figure 15. Variation in Constant Acceleration Inlet Velocity Profile.

C. VARIATION IN TERMINAL VELOCITY

Having simulated changes in acceleration, the next step in the study was to determine the effects of changes in terminal velocity. Using a similar approach to the one in the previous section, two cases were modeled that simulated terminal velocities higher and lower than the base model utilizing the same inlet acceleration equation of y=4x. The first case extended the acceleration domain to [0,0.63] second and a terminal velocity of 2.5 m/s. The second narrowed the domain to [0,0.38] second and a resulted in a terminal velocity of 1.5 m/s; both terminal velocity and base model profiles are shown in Figure 16.

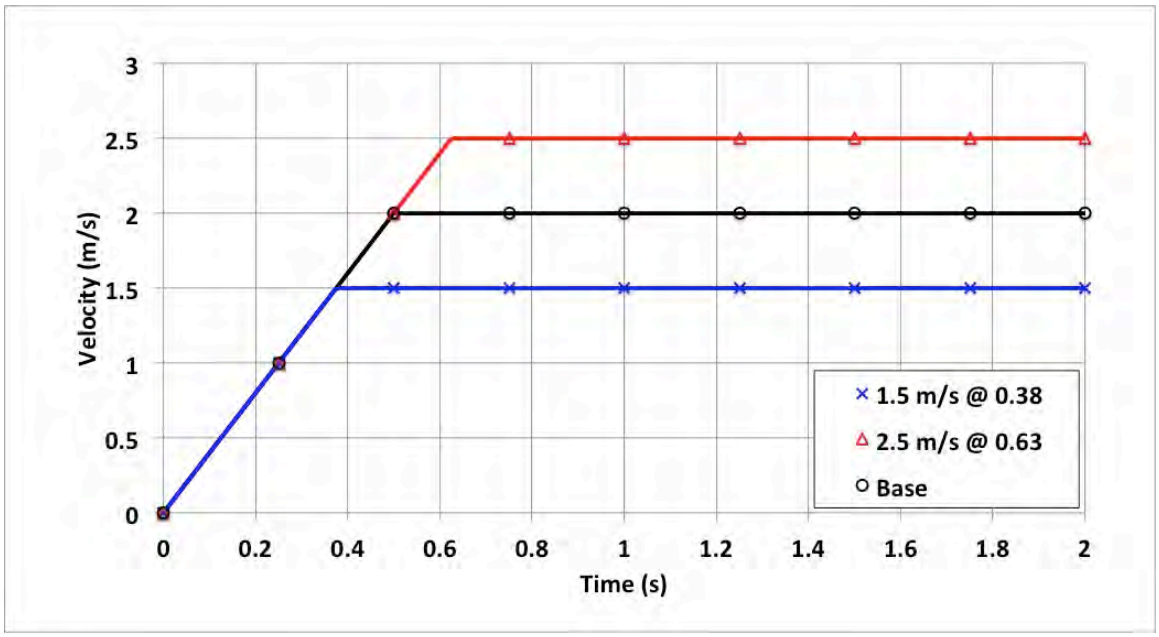

Figure 16. Variation in Terminal Velocity Inlet Velocity Profile.

D. STEP ACCELERATION

The step acceleration case represented a combination of the changing terminal velocity and acceleration rate profiles previously discussed and forced the material to respond to interruptions in constant acceleration. This prompted the structural domain to respond to incremental increases in velocity and be subject to shorter periods of constant acceleration. The first case, 4-step, simulated four periods of constant velocity at 0.5, 1, 1.5 and 2 m/s while the second case, 2-step, held velocity constant at 1 and 2 m/s. In both cases the mid-step acceleration was constant. Figure 17 shows both 4-step and 2-step inlet velocity profiles compared to the base model. Although all simulations completed the full two seconds, only the transient portion is shown.

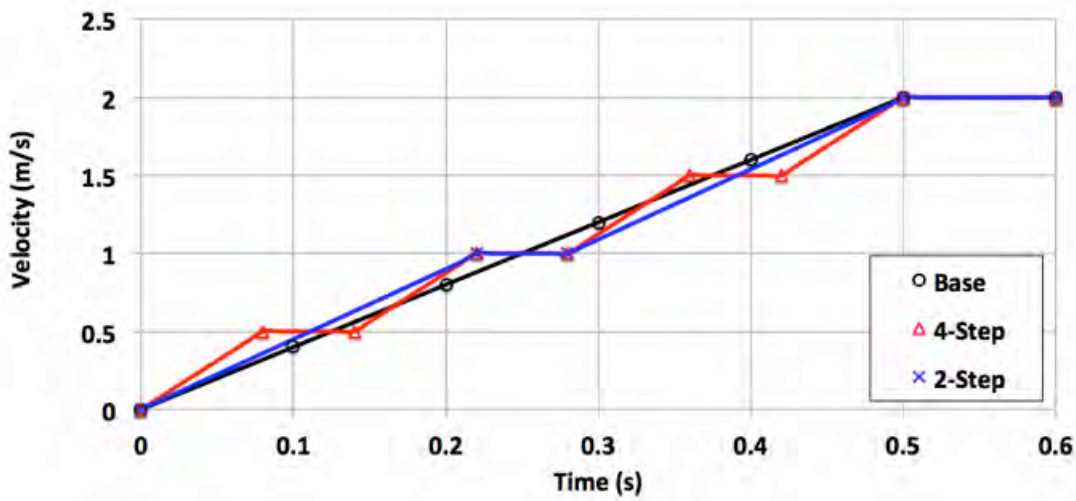

Figure 17. Step Acceleration Inlet Velocity Profile.

E. SIMULATED ACCELERATION

Real world acceleration is rarely constant and thus the next cases represented an inlet velocity profile similar to that of a ship accelerating from rest. The first case modeled a monotonically increasing acceleration and the second was monotonically decreasing (Figure 18). Together they show the effects of nonlinear acceleration during the period of velocity variation. Both simulations completed the 2-second run although only the pertinent sections are shown in Figure 18.

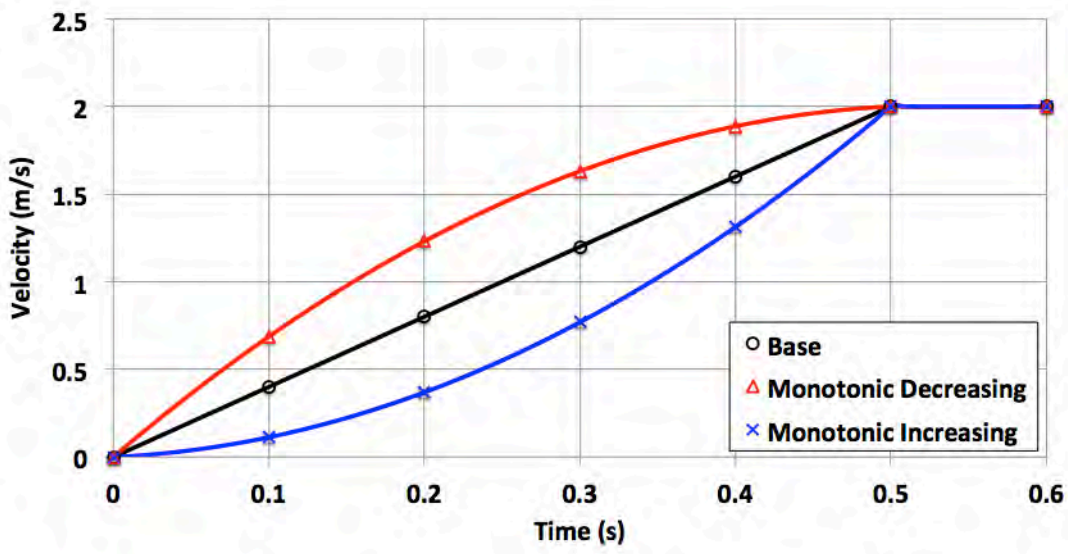

Figure 18. Simulated Acceleration Inlet Velocity Profile.

F. GEOMETRIC VARIATION

The next study involved geometric changes to evaluate structural resistance. While flat plates in flow are useful for study and finite approximations, far more complex geometry is easily expected in ship design. Therefore, it was important to gain an understanding of how changes in geometry would affect the stresses induced by the flow.

The first geometry variant was a reduction in cube size by half, from one meter to 0.5 meters on all sides. This would result in less deformation to the flexible composite plate (Figure 19).

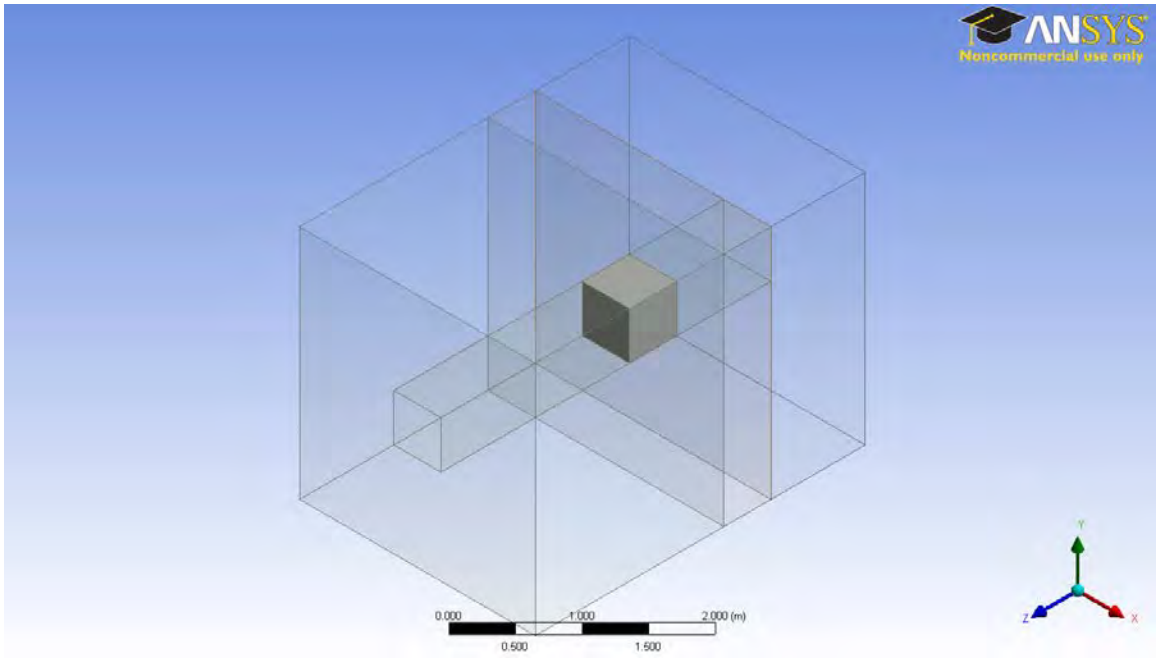

Figure 19. Cube, 0.5 Meter.

The next geometric shift was the transition from cubic to cylindrical. In this case a flat-faced one-meter diameter cylinder replaced the cube (Figure 20), which allows for an even distribution of support provided by the fixed side to the fluid-structure interface. The final geometric variant replaced the flat interface with a semi-spherical one-meter radius dome as the interface (Figure 21).

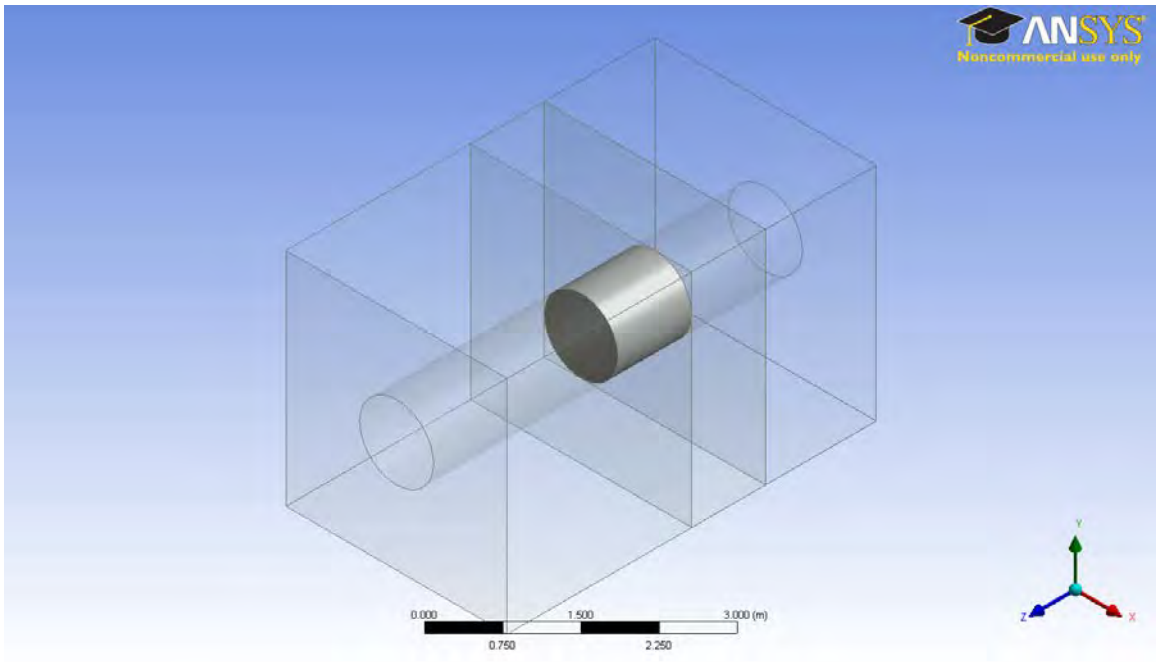

Figure 20. Cylinder, Flat Face.

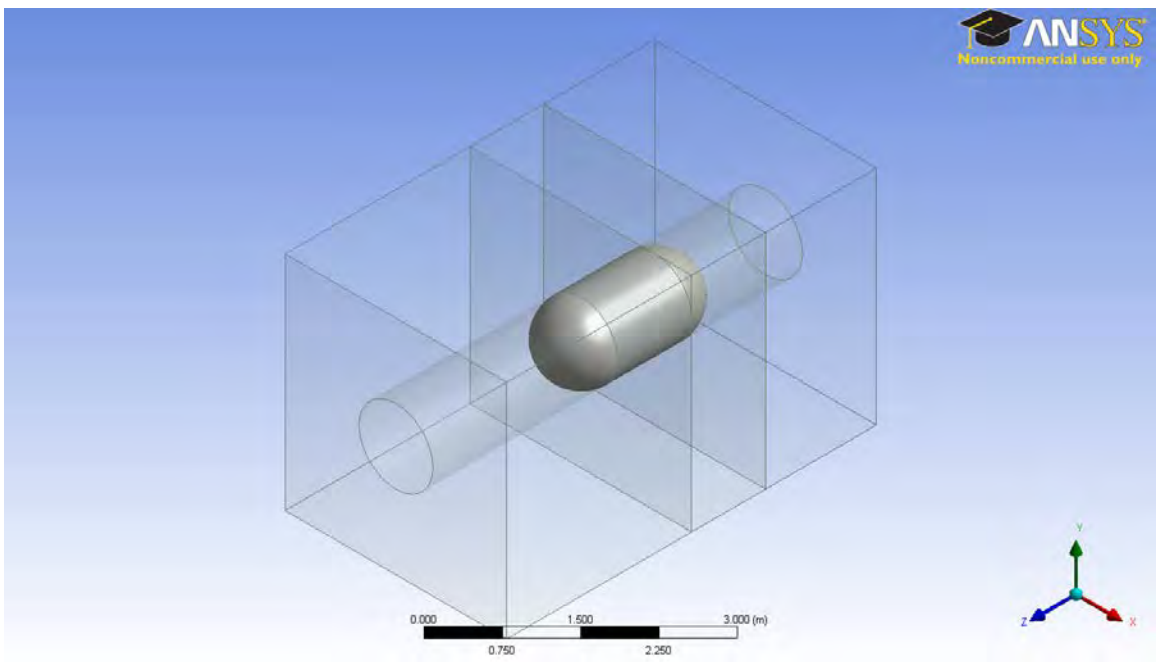

Figure 21. Cylinder, Dome Face.

G. MATERIAL PROPERTY VARIATION

The final cases compared to the base model included changes to the composite material properties. By changing density and Young's modulus, an evaluation of their effect on structural response to an accelerating fluid can be made. These cases also included a free surface to increase their applicability from a design application perspective. There were no additional changes made from the base model to include inlet velocity profile. Material properties for these three models are presented in Table 2.

Table 2. Variation in Material Property.

	Base	2000/50	2000/100	3000/50
Density (kg/m3)	2,000	2,000	2,000	3,000
Young's modulus	50	50	100	50

H. DEPTH VARIATION

Having completed the full range of inlet velocity changes it was necessary to add another variable for comparison, one that would include another element of ship design. The boundary conditions used in the base model represent a submerged cube in an infinitely large fluid domain, similar to an underwater vehicle, in which the fluid is evenly forced around the object on all sides. To enable application to surface vessels, a free surface was modeled in ANSYS by configuring the upper fluid boundary to OPENING with opening pressure: 0 Pa. All depth simulations included the free surface and retained the same inlet velocity profile as the base model.

The first depth case, set at one meter, was identical to the base model with the only change being the addition of a free surface. This allowed for a direct comparison to depict the effects of the free surface. The second and third cases increased the depth to two and three meters respectively. Figure 22 shows the inclusion of the free surface and two-meter depth increase.

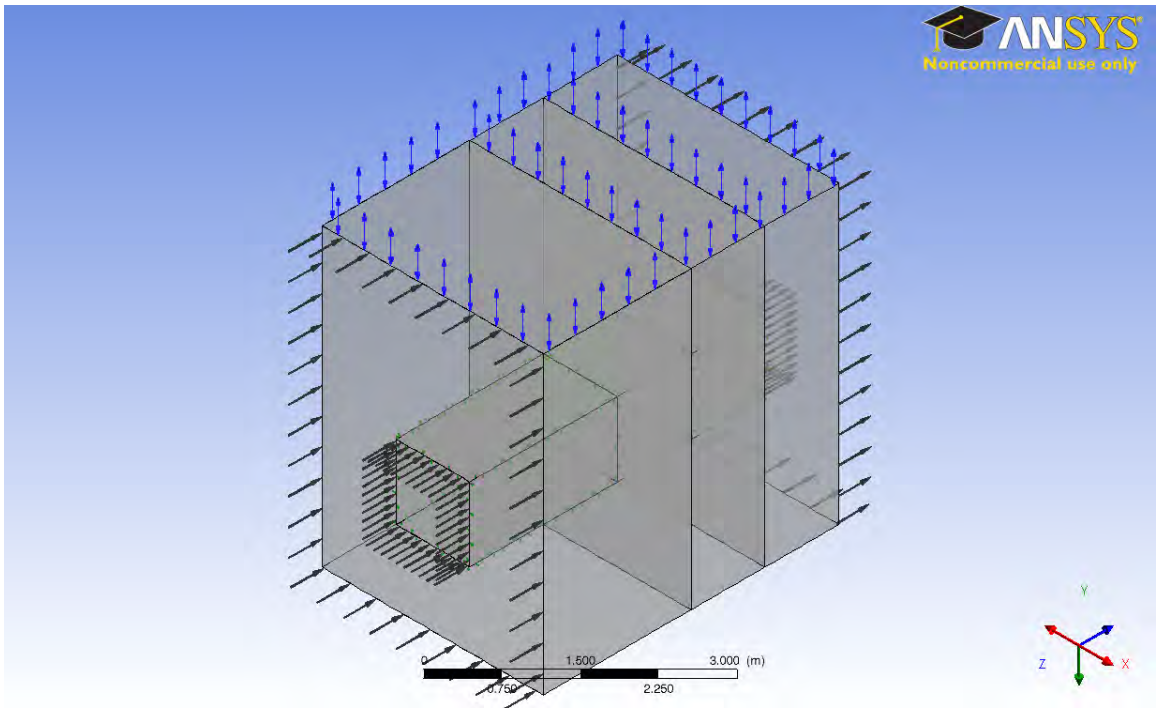

Figure 22. Cube at 2 Meters Depth.

V. RESULTS

A. BASE MODEL: CONSTANT ACCELERATION FOR 0.5 SECOND

The base model was run and data selected for six nodal locations, one being the center (Figure 23). These points were selected for analysis based on symmetric results about the cube face. At each node values for acceleration, displacement, elastic equivalent strain, von Mises stress, and pressure were selected. Interface average pressure and pressure at the center node were also selected for each time step.

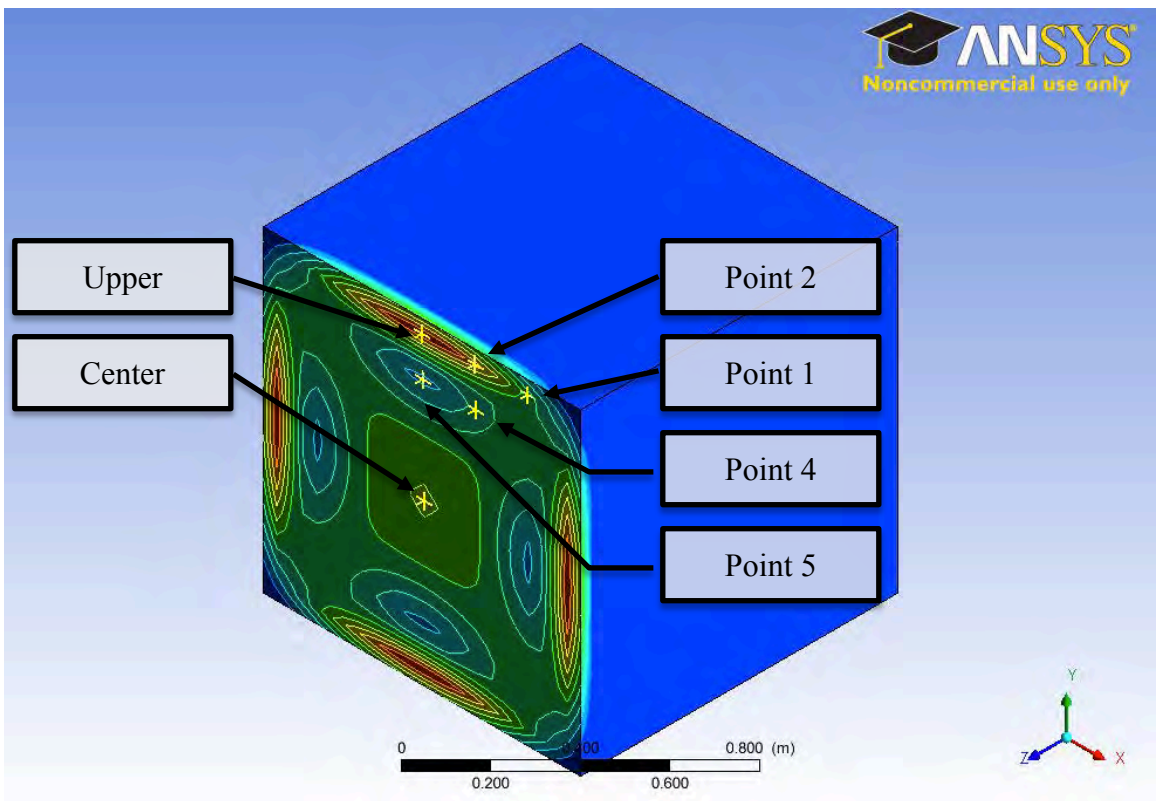

Figure 23. Nodal Data Sample Locations.

In order to determine the maximum stress in the structural domain caused by transient flow, it is necessary to first verify the location of peak stress. This was accomplished by completing a node – node comparison of recorded values. As shown in Figure 23, five nodal locations and the center node were selected based on symmetry

about the face. Strain versus time was then plotted for the six selected nodes of the base model (Figure 24). This data shows that the upper node, comparatively, had the highest recorded strain value. This process was repeated for von Mises stress and displacement; stress correlated with strain and the upper node had the maximum value compared to other locations on the cube face while maximum values for displacement occurred at the center. The upper node peak stress was also compared to similar locations at the remaining three edges. All four locations had equal results and further verified symmetry about the interface.

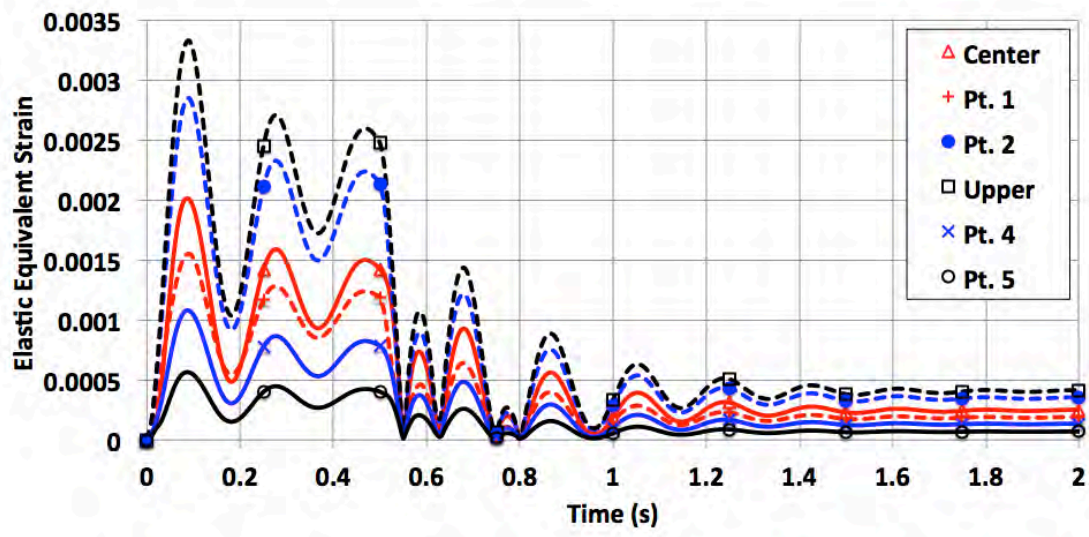

Figure 24. Base Model 6-Node Strain Comparison.

Peak (absolute) nodal data for all sample locations (Figure 23) were recorded in Table 3 for displacement, equivalent elastic strain and von Mises stress. Steady state values were determined by averaging results from each time step for the final 0.25 seconds of the trial and also recorded in Table 3. By comparing maximum to steady state values, a ratio of transient to steady state forces can be determined and a direct comparison of various simulations can be completed.

The highest stress and strain occurred at the upper node, which is expected based on the resistance offered by the fixed side. Although points 1 and 2 yielded higher ratios, this is insignificant because their values are much smaller and peak stresses are the primary concern.

Displacement and acceleration were also considered and compared side by side to stress and strain but this comparison added little value. Since acceleration has a steady state value of near zero, no valid comparison of the ratio can be made. Displacement was considered; and although it has a measurable steady state value, the maximum ratio did not occur at the center node but rather at point 1. This ratio, while higher, is insignificant because maximum and steady state values are less than half of the center node and provide an erroneous data point for a quantitative comparison. Additionally, peak values for stress and strain occurred at the same time step as displacement, as expected.

Table 3. Base Model 6-Node Evaluation.

	Point 1	Point 2	Upper	Point 4	Point 5	Center
	Elastic Equivalent Strain					
Maximum	0.001553	0.002849	0.003328	0.001079	0.000564	0.002008
Steady State	0.000189	0.000350	0.000409	0.000134	0.000070	0.000248
Ratio	8.20	8.13	8.12	8.04	8.02	8.09
	Von Mises Stress (MPa)					
Maximum	31.1	57.0	66.6	21.6	11.3	40.1
Steady State	3.8	7.0	8.2	2.7	1.4	5.0
Ratio	8.20	8.13	8.12	8.04	8.02	8.09
	Displacement (mm)					
Maximum	0.609	1.261	1.477	13.817	16.408	44.700
Steady State	0.072	0.153	0.181	1.704	2.025	5.538
Ratio	8.37	8.19	8.18	8.11	8.10	8.07

To further understand the response of the plate to a transient flow, an intermediate variable that relates the fluid input to a structural response must be considered. In this case both (nodal) acceleration and displacement were considered. Both variables are dependent upon the force of fluid acting upon the plate, which is dependent upon fluid velocity. Figure 25 shows acceleration and displacement of the center node.

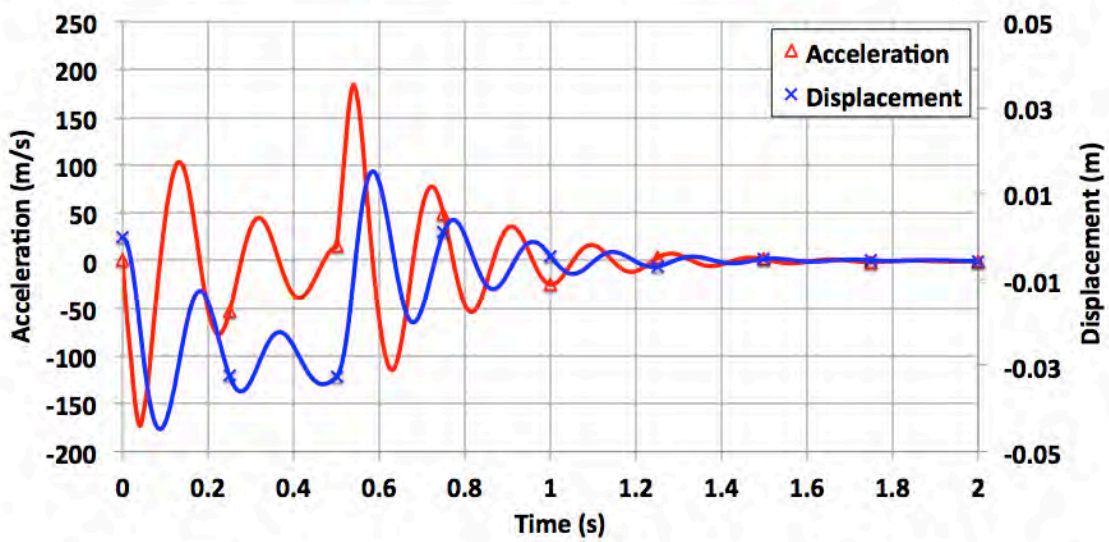

Figure 25. Base Model Center Node Acceleration Versus Displacement.

Plate displacement corresponded closely to acceleration with expected minimal lag between the two variables. There was an average 0.04 sec delay of local maximum and minimum displacement values to acceleration values. This delay further validates the FSI model and proves that the transfer of forces was independent of time step and related to actual plate response to the fluid flow. Peak values for structural stress and strain occur during times when displacement is at either a local maximum or minimum. Lastly, at 0.5 seconds, the fluid acceleration suddenly changes to zero (Figure 14) and there was an immediate response in structural nodal acceleration as well as in displacement.

Hydrodynamic pressure was the final data point evaluated from the base model and evaluated at both the center node and also averaged over the entire flexible interface

for all the time steps (Figure 26). The center node received the highest peak and steady state forces, even when compared to the interface average. As expected, the average pressure plot closely matched the center node plot.

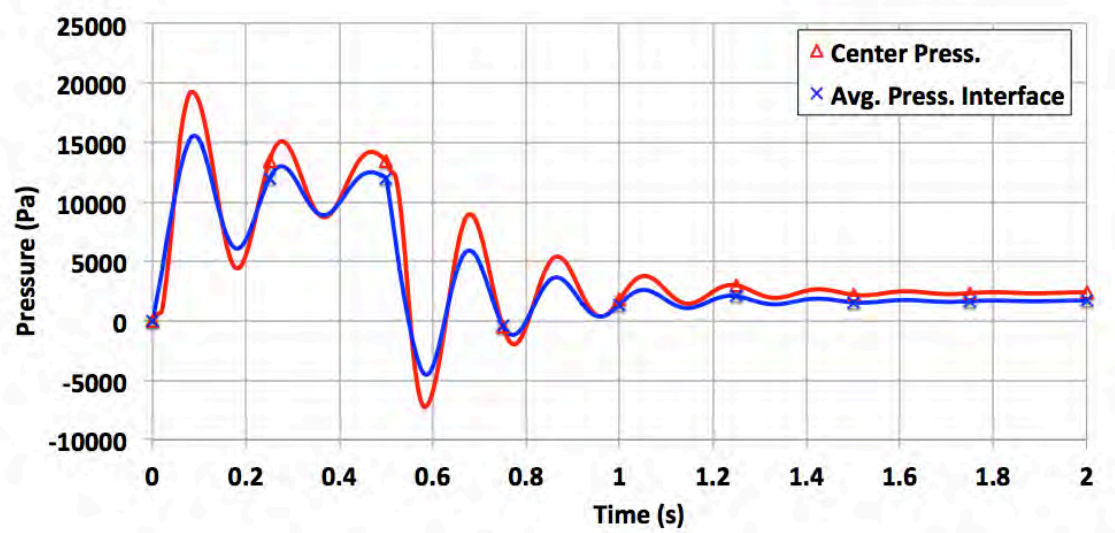

Figure 26. Base Model, Pressure at Center Versus Average Pressure at Interface.

The same quantitative comparison used for structural forces was applied to pressure, the maximum, steady state, and their ratios were determined (Table 4). In this case, the average pressure had the higher ratio, although the center node had the highest value.

Table 4. Base Model Hydrodynamic Evaluation.

	Avg. Pressure At Interface (Pa)	Pressure At Center (Pa)
Maximum	15,574.00	19,162.80
Steady State	1,688.65	2,373.36
Ratio	9.22	8.07

Stress, strain and displacement transient values exceeded steady state values by a factor of eight; however, this is closely linked to the applied boundary conditions and

must be carefully observed. The base model was a symmetric cube in a symmetric fluid domain with symmetric boundary conditions, and it is therefore logical for both structural and fluid forces to be symmetric about the face. The base model is a suitable for comparison in cases where both geometric and boundary condition symmetry are retained (all cases except depth variation) and thus further evaluation of nodes other than center and upper have been omitted. Additionally, cases sharing geometry and boundary conditions will also have the same stress and strain distribution as shown in Figure 23.

Prior to the study of depth variation case, a base model was revised to include a free surface and additional data points along the vertical plane of the interface were selected for comparison.

B. VARIATION IN CONSTANT ACCELERATION

The first case evaluated was the comparison of two constant acceleration models. The base model achieved a terminal velocity of 2 m/s at 0.5 second and the comparative models achieved the same speed in 0.25 second and 1 second. Since all three models shared the same boundary conditions, only data from the upper and center structural node was evaluated. Elastic equivalent strain, von Mises stress, displacement, and pressure were plotted for both cases against the base model (Figure 27, 28, 29, and 30).

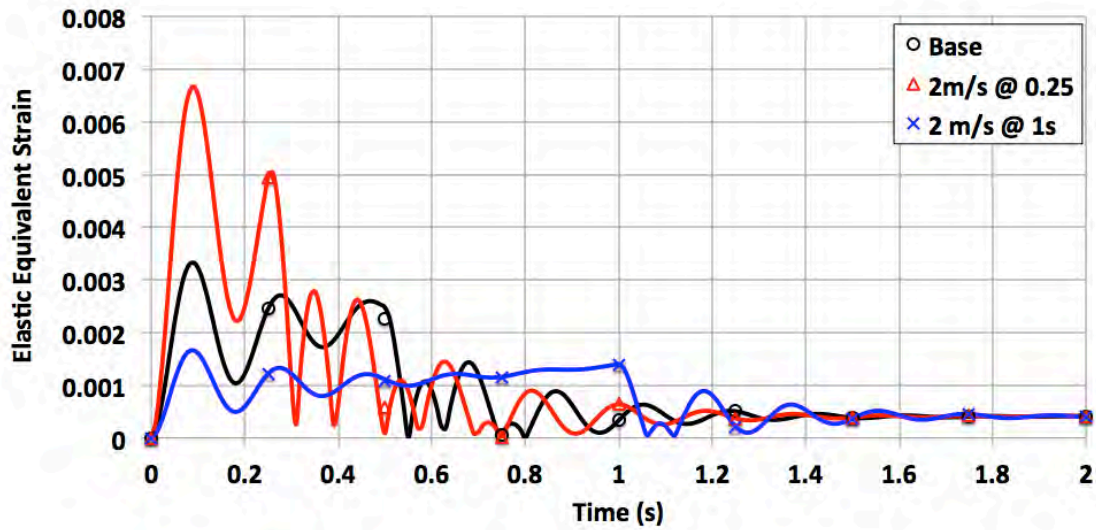

Figure 27. Variation in Constant Acceleration, Strain at Upper Node.

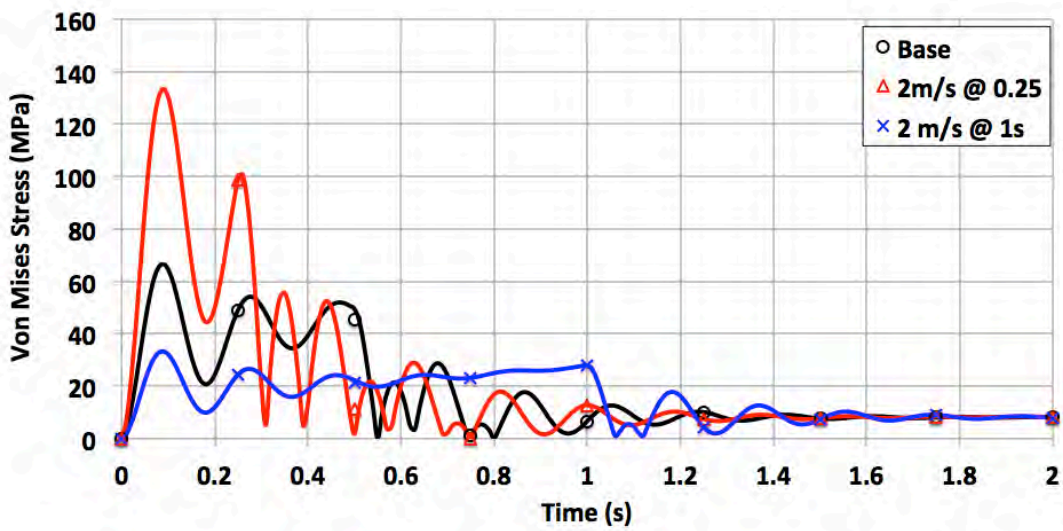

Figure 28. Variation in Constant Acceleration, Stress at Upper Node.

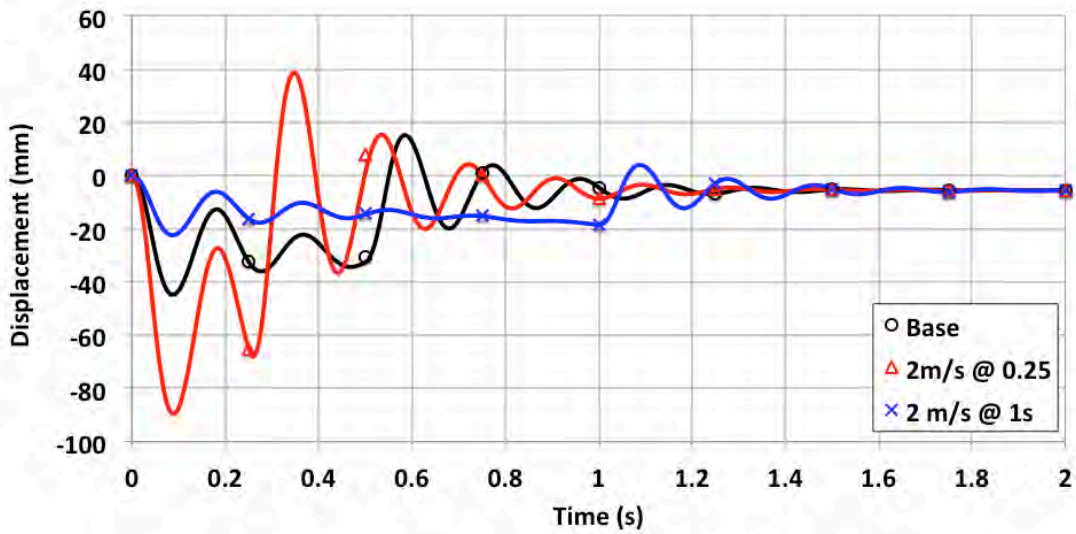

Figure 29. Variation in Constant Acceleration, Displacement at Center Node.

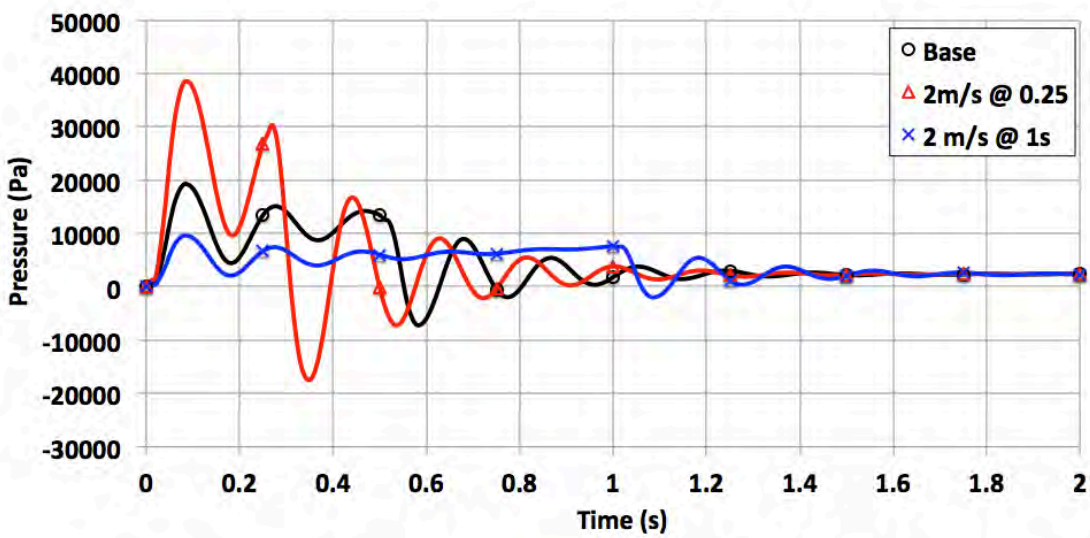

Figure 30. Variation in Constant Acceleration, Pressure at Center Node.

Peak stress and strain values were recorded at 0.09 seconds during the first inward oscillation of the interface regardless of the rate of the constant acceleration, which correlates with the times for maximum displacement and is expected. The peak values were compared to the steady state value assumed to be the last 0.25 seconds of the run (Table 5).

Table 5. Variation in Constant Acceleration, Case Summary.

	2 m/s @ 0.25s	Base	2 m/s @ 1s
	Elastic Equivalent Strain		
Maximum	0.006667	0.003328	0.001663
Steady State	0.000414	0.000410	0.000410
Ratio	16.11	8.12	4.05
	Von Mises Stress (MPa)		
Maximum	133.3	66.6	33.3
Steady State	8.3	8.2	8.2
Ratio	16.11	8.12	4.05
	Displacement (mm)		
Maximum	89.573	44.700	22.331
Steady State	5.590	5.538	5.543
Ratio	16.02	8.07	4.03
	Pressure (Pa)		
Maximum	38,459.20	19,162.80	9,596.10
Steady State	2,373.36	2,373.36	2,378.10
Ratio	16.09	8.07	4.03

These results show the acceleration rate has a significant contribution in the amplitude of transient stress. The twice as fast model (2 m/s at 0.25s) showed transient stress twice as high as the base; conversely, the slower (2 m/s at 1s) model resulted in half the stress.

Another interesting observation came with the occurrences of plate oscillations. All three cases showed an initial negative displacement in response to an initial fluid

pressure and they all reached their maximum stresses at the same time. However, the 2 m/s at 1 second model showed that the magnitude of oscillation is dependent upon the slope of acceleration, which was most apparent in the oscillation decay that occurred during 0.25 to 1 second. Also, all three models showed the resumption and subsequent decay of oscillations upon reaching their respective steady sate velocity and zero acceleration.

The stress and strain ratios provided in Table 5 enable a direct comparison of peak forces. A common axis was needed for this comparison; the slope during transient acceleration was selected as the best option. Figure 31 compares ratios against slope for base, 2 m/s at 0.25s, and 2m/s at 1s simulations and includes a trendline ($R^2 = 1$).

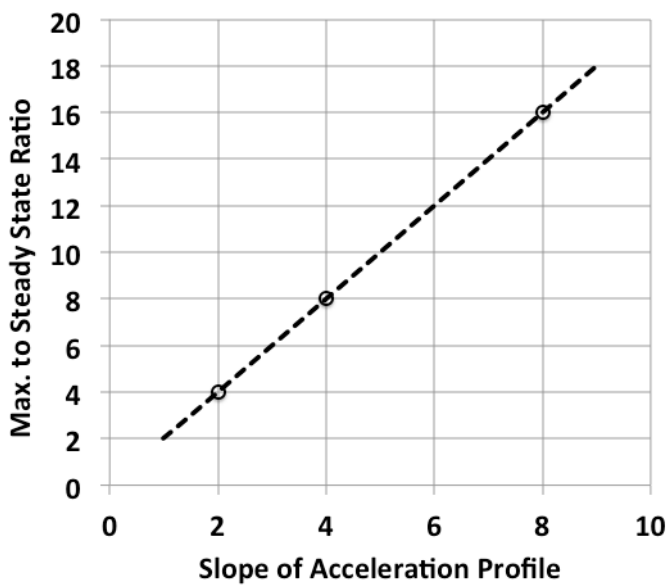

Figure 31. Variation in Constant Acceleration, Ratio Comparison.

All three simulations evaluated in this case shared identical geometry and boundary conditions and the only variant was acceleration. This profile clearly suggests a linear relationship between the rate of acceleration and the peak stresses induced therein.

C. VARIATION IN TERMINAL VELOCITY

The following cases evaluate the peak stresses induced by a change in terminal velocity. The base model reached a terminal velocity of 2 m/s and therefore suggested that simulations be run to terminal velocities of 2.5 m/s and 1.5 m/s. Figures 32, 33, 34 and 35 show plots of strain, stress, displacement and pressure for the three variations.

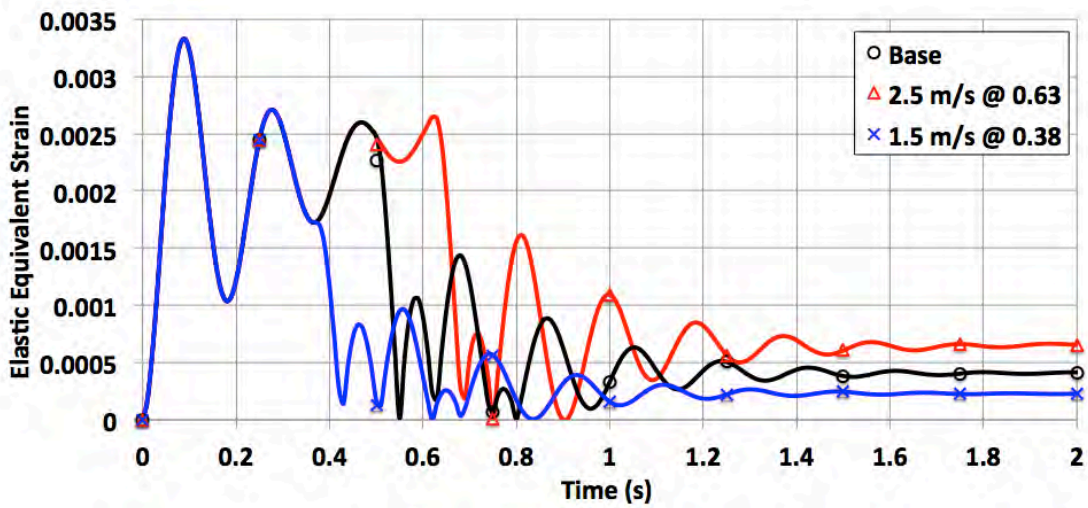

Figure 32. Variation in Terminal Velocity, Strain at Upper Node.

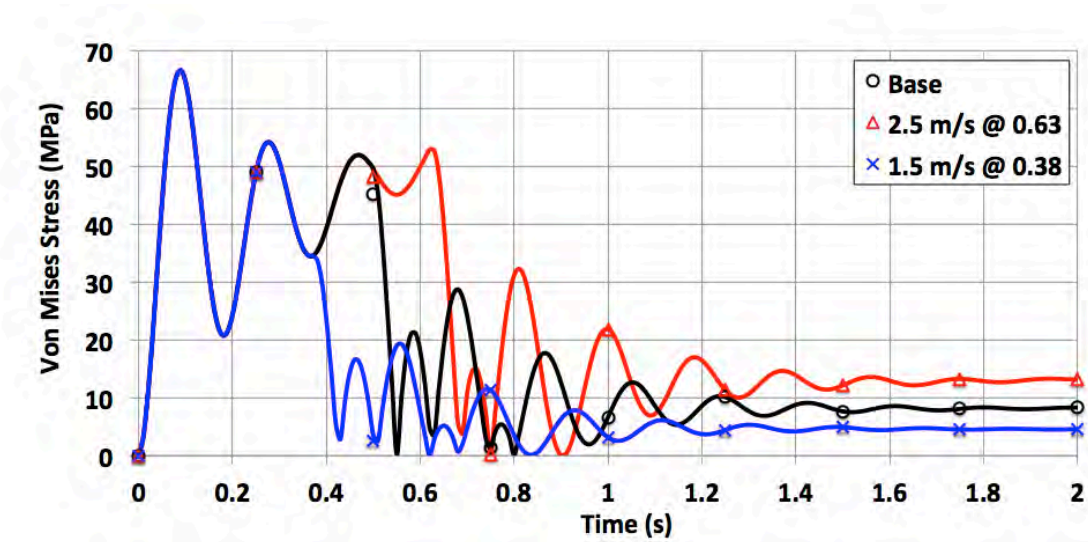

Figure 33. Variation in Terminal Velocity, Stress at Upper Node.

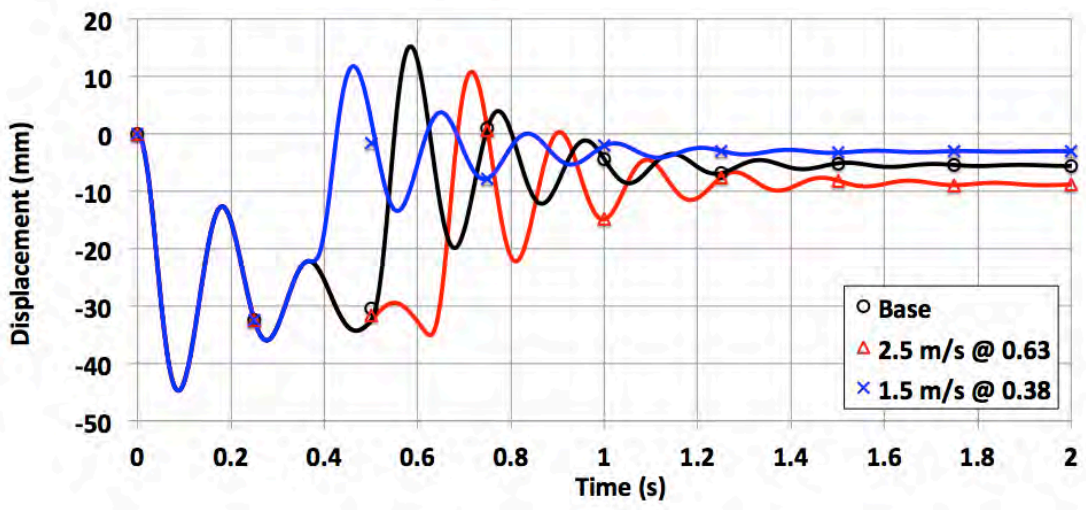

Figure 34. Variation in Terminal Velocity, Displacement at Center node.

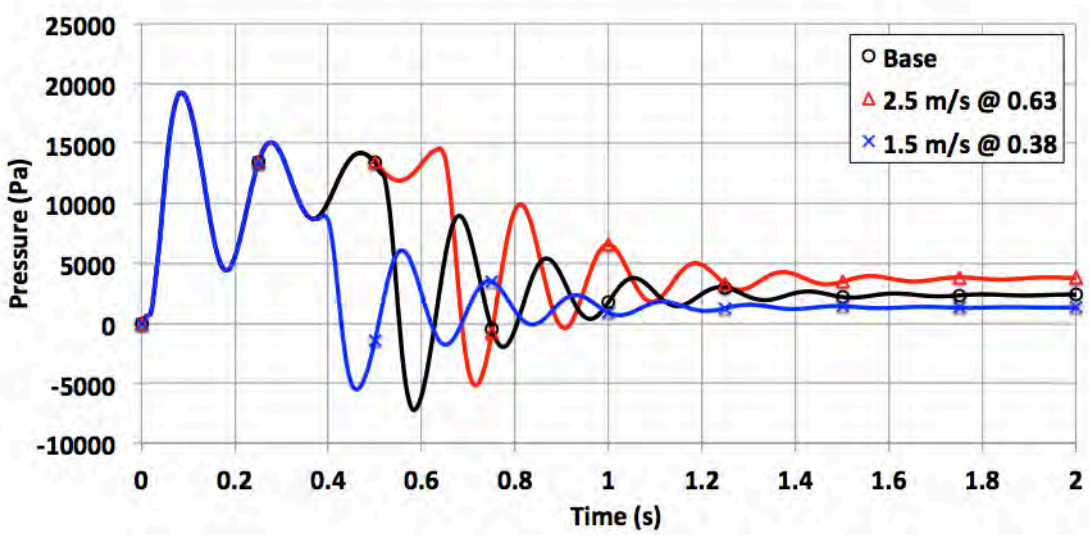

Figure 35. Variation in Terminal Velocity, Pressure at Center Node.

Peak stress and strain values were recorded at 0.09 seconds during the first inward oscillation of the interface, which correlates with the times for maximum displacement and is expected. While the peak values were identical for all three cases, the steady state values differed due to the terminal velocity. Peak values were compared to the steady state value assumed to be the last 0.25 seconds of the run (Table 6).

Table 6. Variation in Terminal Velocity, Case Summary.

	2.5 m/s @ 0.63	Base	1.5 m/s @ 0.38
	Elastic Equivalent Strain		
Maximum	0.003328	0.003328	0.003328
Steady State	0.000652	0.000410	0.000228
Ratio	5.10	8.12	14.58
	Von Mises Stress (MPa)		
Maximum	66.6	66.6	66.6
Steady State	13.0	8.2	4.5
Ratio	5.10	8.12	14.58
	Displacement (mm)		
Maximum	44.700	44.700	44.700
Steady State	8.81	5.538	3.082
Ratio	5.07	8.07	14.5
	Pressure (Pa)		
Maximum	19,162.80	19,162.80	19,162.80
Steady State	3,763.74	2,373.36	1,322.15
Ratio	5.09	8.07	14.49

The results from this case differed from the previous case in that the steady state value was the primary variable instead of varying magnitudes of peak stress. Since the 1.5 m/s at 0.38 second simulation had the lower steady state values it also resulted in the highest ratios.

This case also gives additional insight into plate oscillation in response to hydrodynamic force. As shown in Figure 34, the initial displacement occurs in the

negative direction and oscillations remain entirely negative within that domain. It is only when acceleration stops that plate oscillations secure mid-cycle and the plate responds with a positive deflection that decays to a steady state negative displacement.

Plotting peak stress ratios versus terminal velocity for each simulation and the addition of a trendline (R^2 = 0.999) allows for a direct comparison between models (Figure 36). Peak stresses occurred at 0.09 seconds prior to any change in acceleration therefore all simulations received the same peak stress. Since ratio differences were driven by steady state force values, the slower terminal velocity (and subsequent lowest steady state force values) had the highest ratios. This case shows that peak stress is independent from terminal velocity and if material selection is based on terminal velocity without consideration to transient flow conditions, material failure could be possible.

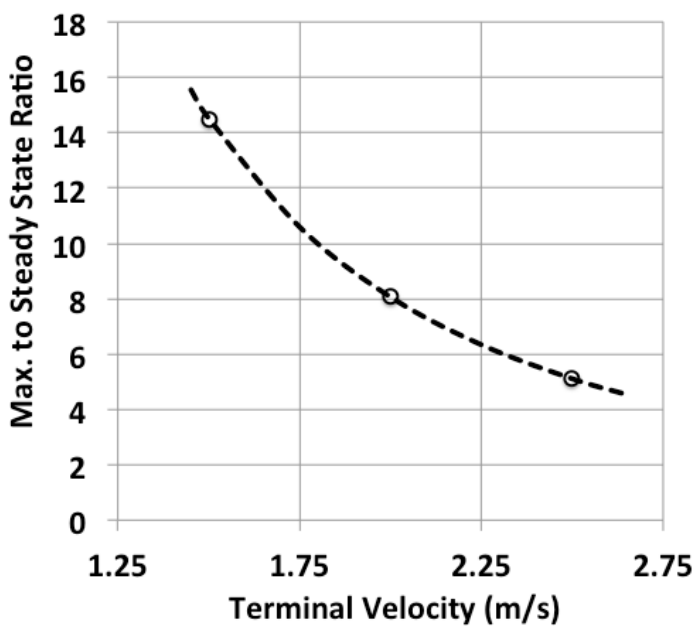

Figure 36. Variation in Terminal Velocity, Ratio Comparison.

D. STEP ACCELERATION

This case evaluated the structural response from interruptions in acceleration. The 4-step model had four periods of zero acceleration and the 2-step model had two; for

each simulation acceleration was held constant between steps. There were no changes made to the base model. Upper node stress and strain, and center node displacement and pressure were plotted for all three simulations (Figures 37, 38, 39, 40).

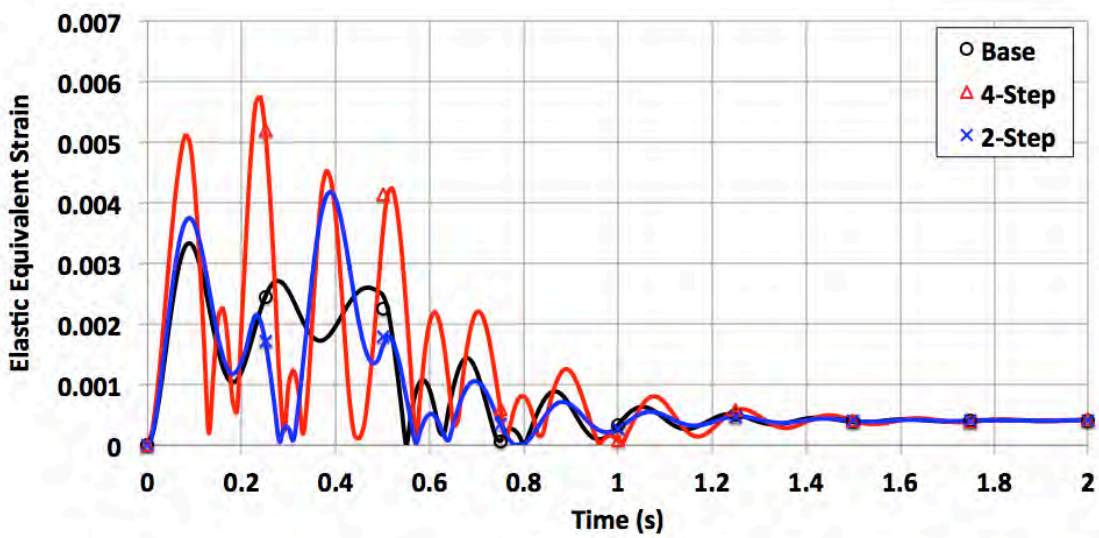

Figure 37. Step Acceleration, Strain at Upper Node.

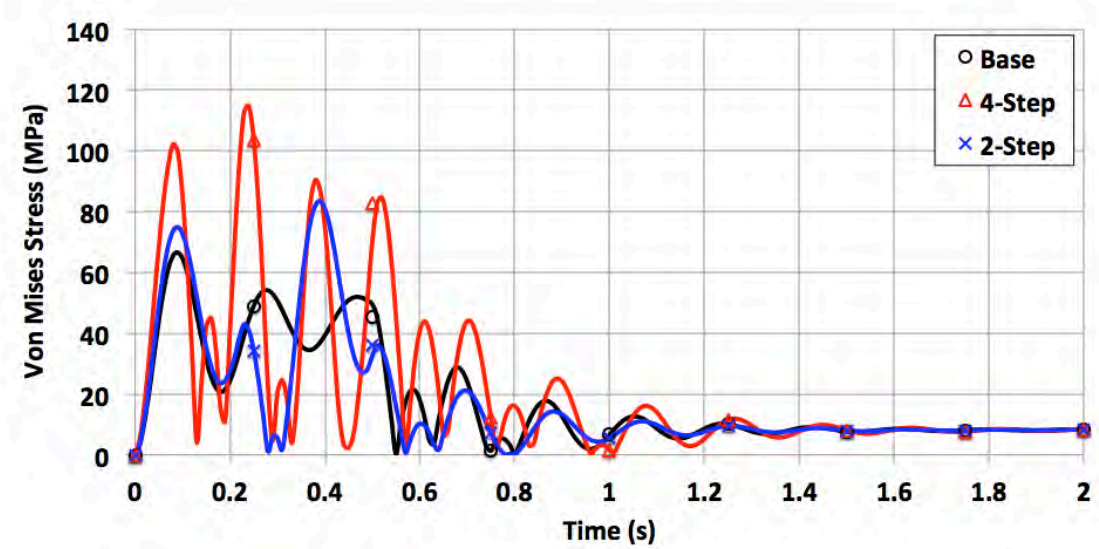

Figure 38. Step Acceleration, Stress at Upper Node.

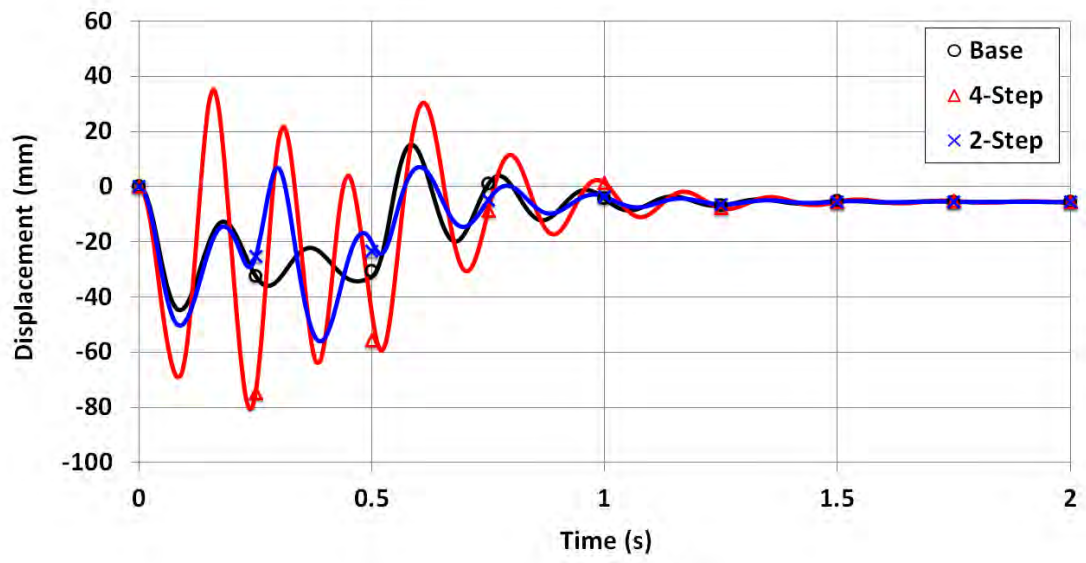

Figure 39. Step Acceleration, Displacement at Center Node.

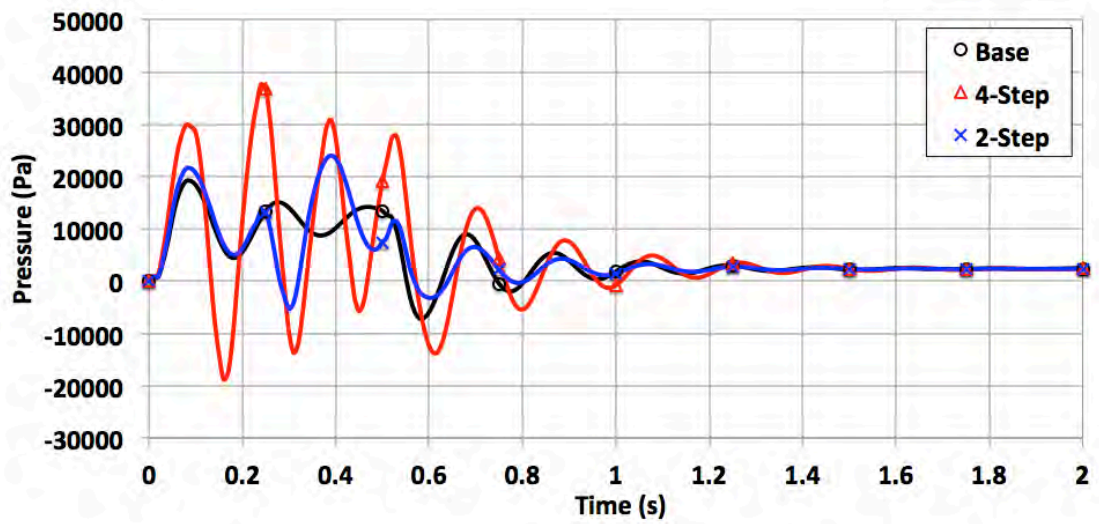

Figure 40. Step Acceleration, Pressure at Center Node.

The peak displacement occurred for all three cases during inward deflections at different times. The base model peaked at 0.09 seconds however the 4-step model peaked during the second zero acceleration period at 0.24 seconds and the 2-step model peaked halfway through the second acceleration period at 0.39 seconds. Maximum values were recorded and compared to steady state values in Table 7.

Table 7. Step Acceleration, Case Summary.

	4 Step	Base	2 Step
	Elastic Equivalent Strain		
Maximum	0.005732	0.003328	0.004173
Steady State	0.000408	0.000410	0.000408
Ratio	14.06	8.12	10.21
	Von Mises Stress (MPa)		
Maximum	114.6	66.6	83.5
Steady State	8.2	8.2	8.2
Ratio	14.06	8.12	10.21
	Displacement (mm)		
Maximum	80.894	44.700	56.079
Steady State	5.505	5.538	5.520
Ratio	14.69	8.07	10.16
	Pressure (Pa)		
Maximum	376,908.80	19,162.80	24,016.50
Steady State	2,354.92	2,373.36	2,365.17
Ratio	15.97	8.07	10.15

These results indicate that successive interruptions in acceleration can have a serious effect on transient forces. The 2-step model showed a 25 percent increase in transient stress while the 4-step model increased stress by 72 percent. Although acceleration was constant between the interruptions for each model, the three models did not share the same acceleration. The 4-step model had the highest acceleration of 6.25 m/s^2, the 2-step was second highest with 4.5 m/s^2 and the base model had an acceleration

of 4 m/s^2. As shown in previous cases, higher acceleration yields higher stresses and these simulations reaffirm this conclusion. Although previous cases also indicate that peak transient stress occurs upon initial negative displacement, both 4-step and 2-step models had peak transient stresses that occurred during the second and third inward displacements respectively (Figure 39). This indicates that interruptions in acceleration have an effect when considering peak transient stress.

Oscillatory responses of both 4-step and 2-step models showed unique results. For the 2-step model, zero acceleration periods began at 0.22 and 0.5 second and both of these times correlate to sharp increases in plate displacement (Figure 39) and sharp reductions in pressure (Figure 40). Plate response in the 4-step model indicated sharp rises in stresses that correlate with the interruptions in acceleration at 0.08, 0.22, 0.36 and 0.5 seconds. Both models showed signs of oscillation decay similar to those observed in other cases.

Figure 41 compares peak stress ratios to the common variable of acceleration interruptions with an additional trendline (R^2 = 0.990). Ships at sea are frequently exposed to the unpredictable hydrodynamic forces and constantly changing acceleration associated with ocean swells and surface waves and this case adds further justification for sea state limitations actively implemented throughout the fleet.

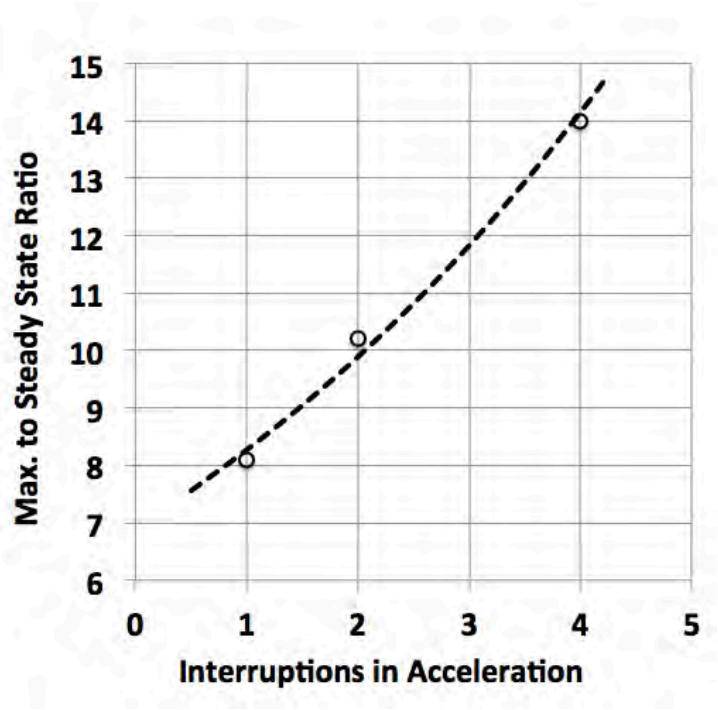

Figure 41. Step Acceleration, Ratio Comparison.

E. SIMULATED ACCELERATION

This case evaluates monotonic changes in acceleration compared to the base model. The monotonic increasing simulation closely resembles the profile of an accelerating ship where acceleration increases with time while the monotonic decreasing model is a near mirror image. Center node stress and strain, and upper node displacement and pressure were plotted for all three cases in Figures 42, 43, 44 and 45, while transient and steady state values and corresponding ratios are shown in Table 8.

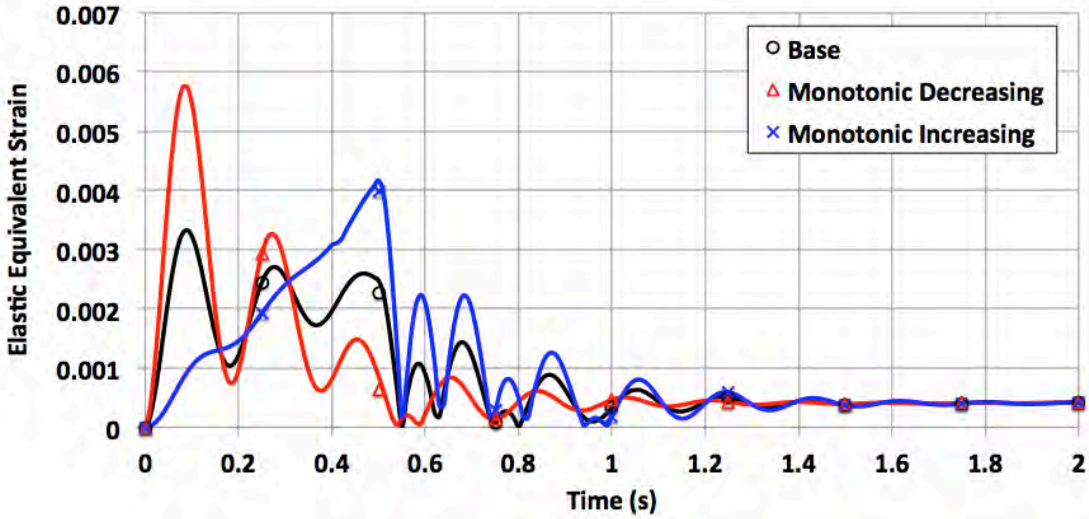

Figure 42. Simulated Acceleration, Strain At Upper Node.

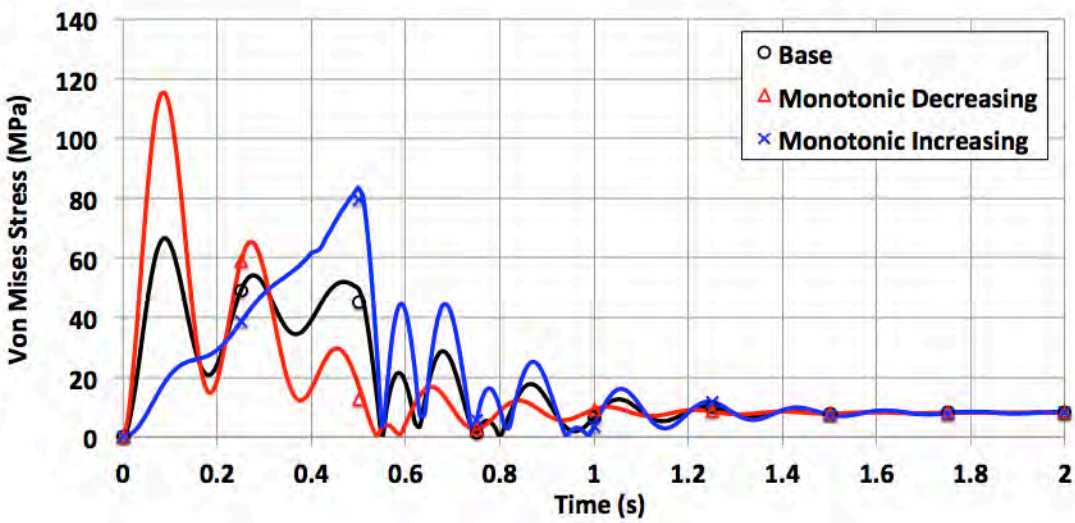

Figure 43. Simulated Acceleration, Stress At Upper Node.

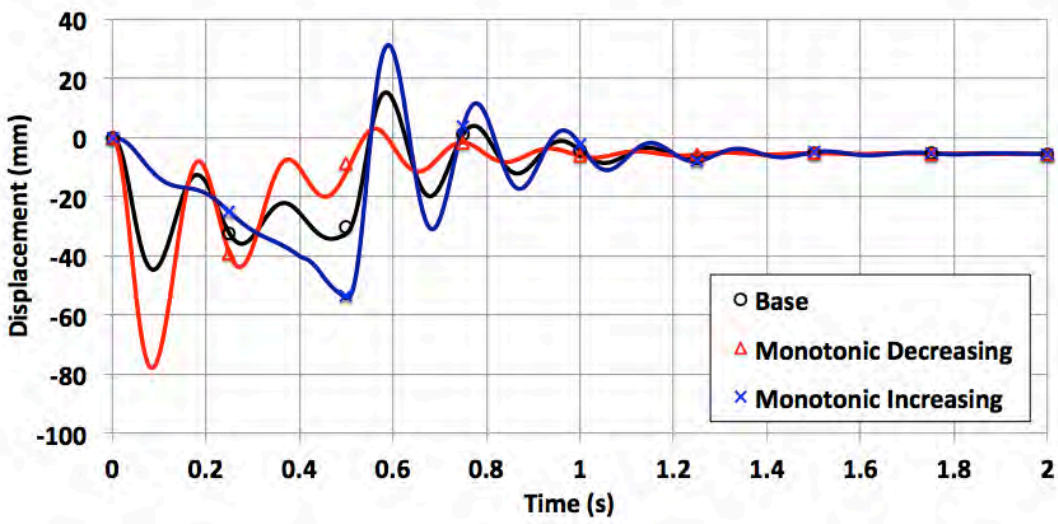

Figure 44. Simulated Acceleration, Displacement At Center Node.

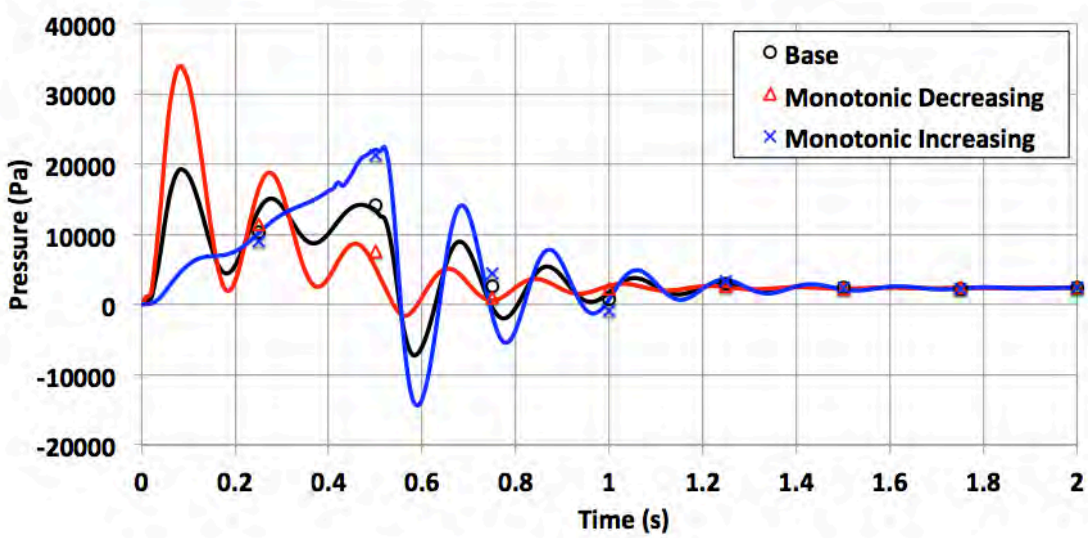

Figure 45. Simulated Acceleration, Pressure At Center Node.

The monotonic decreasing model has a near-linear acceleration for the first 0.25 seconds and the plate responds with oscillations similar to the base model, which also has a linear acceleration. However, the monotonic decreasing model has a larger slope than the base model, which results in oscillations with a higher amplitude (Figure 43). During the final 0.25 seconds of the velocity transient, acceleration slowly reduces to zero in the monotonic decreasing model. This causes the oscillations to begin damping prior to

achieving terminal velocity and results in amplitudes lower than the base model. The monotonic increasing simulation undergoes increasing acceleration that adds steadily increasing hydrodynamic forces and prevents the plate from an oscillatory response. Upon ceasing acceleration, all models respond similar to the other cases with large positive deflections and decaying oscillations.

Table 8. Simulated Acceleration, Case Summary.

	Monotonic Decreasing	Base	Monotonic Increasing
	Elastic Equivalent Strain		
Maximum	0.005743	0.003328	0.004167
Steady State	0.000411	0.000409	0.000409
Ratio	13.97	8.12	10.18
	Von Mises Stress (MPa)		
Maximum	114.9	66.6	83.3
Steady State	8.2	8.2	8.2
Ratio	13.97	8.12	10.18
	Displacement (mm)		
Maximum	77.593	44.700	54.459
Steady State	5.555	5.538	5.532
Ratio	13.97	8.07	9.84
	Pressure (Pa)		
Maximum	33,953.90	19,162.80	22,393.00
Steady State	2,379.06	2,373.36	2,370.38
Ratio	14.27	8.07	9.44

As Table 8 shows, the monotonic decreasing model had the largest ratios of peak to steady state stresses. This is expected based on the initial linearity of the fluid acceleration and having a greater slope than the base model. The monotonic decreasing and base models reach peak displacements in the negative direction at 0.08 and 0.09 second respectively. The monotonic increasing model reached a maximum inward displacement at 0.5 second and ratios were higher than the base simulation because its slope was higher during the second half of the transient. Figure 46 shows a side-by-side transient to steady state ratio comparison.

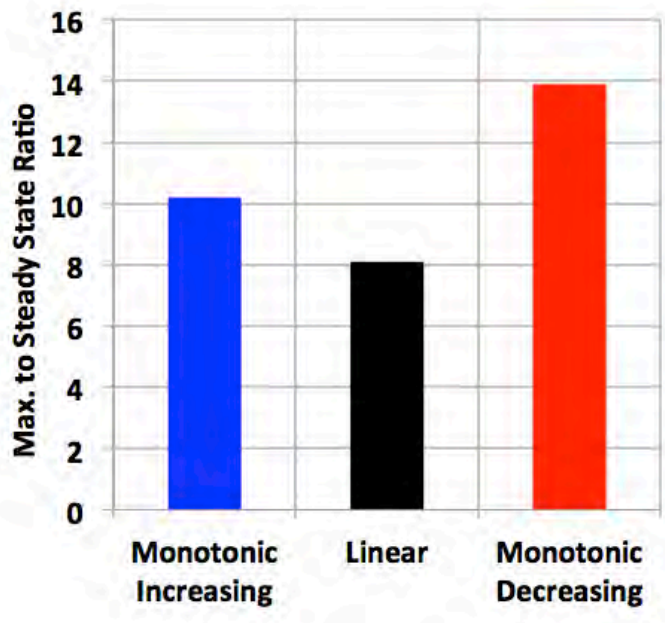

Figure 46. Simulated Acceleration, Ratio Comparison.

When both models are combined they portray a transient velocity curve with an inflection point and reduced acceleration slopes at each end. This combination brings the advantages of each curve and avoids the initial transient oscillation while encouraging rapid oscillation decay prior to reaching steady state velocity. This type of transient velocity curve is also most representative of a ship at sea and proves that the attributes inherent to a transient acceleration are beneficial for the structure.

F. GEOMETRIC VARIATION

These cases investigate the effects of geometry on peak stresses. To maintain continuity all cases were again compared to the base model and received the same inlet velocity profile, attaining 2 m/s at 0.5 seconds. The first model was the cube sized down by one-half (cube 0.5), the second was a flat face cylinder (flat face), and the third was a dome-faced cylinder (cylinder).

Stress distribution for the base model and previous simulations were identical based on geometric and boundary condition symmetry and shown in Figure 23, however the geometric changes of this case require verification of peak stress location. The peak stress location for cube 0.5 (Figure 47) matched the base model location and peak stress for the flat face was also near edge but symmetric around the diameter (Figure 48). The cylinder had a peak stress near the center of the dome (Figure 49). Finally, all models had a peak displacement located in the center of the face. Peak node stress and strain, and center node displacement and pressure results were also plotted for all three cases (Figures 50, 51, 52, and 53).

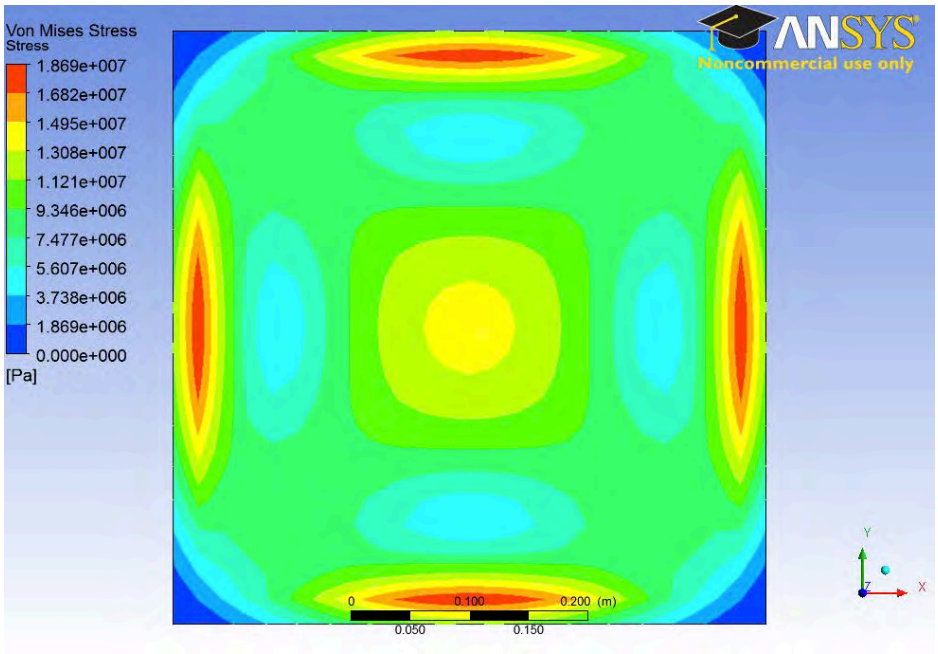

Figure 47. Geometric Variation, Cube 0.5 Peak Stress Location.

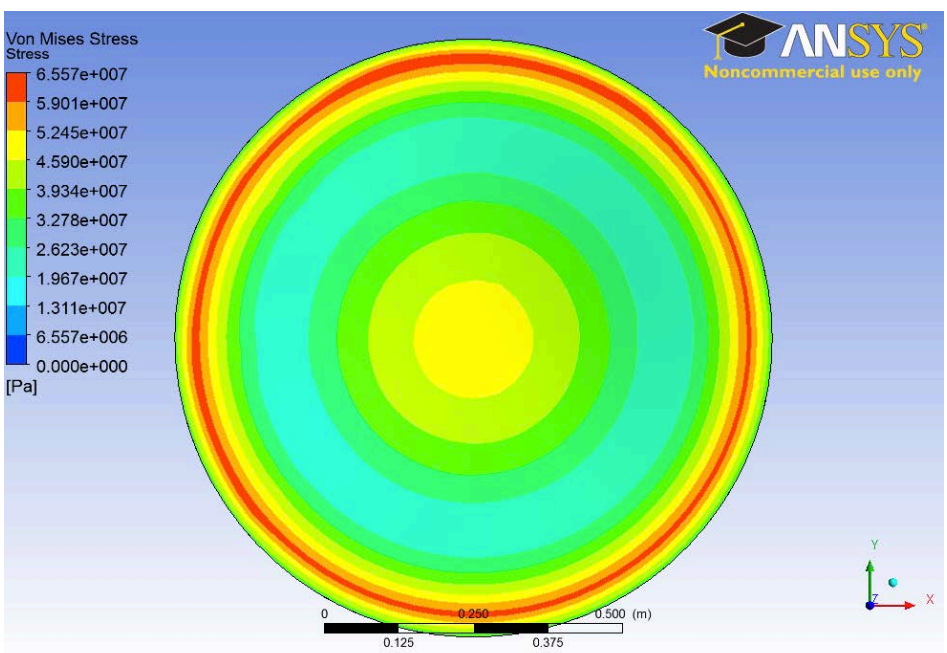

Figure 48. Geometric Variation, Flat Face Peak Stress Location.

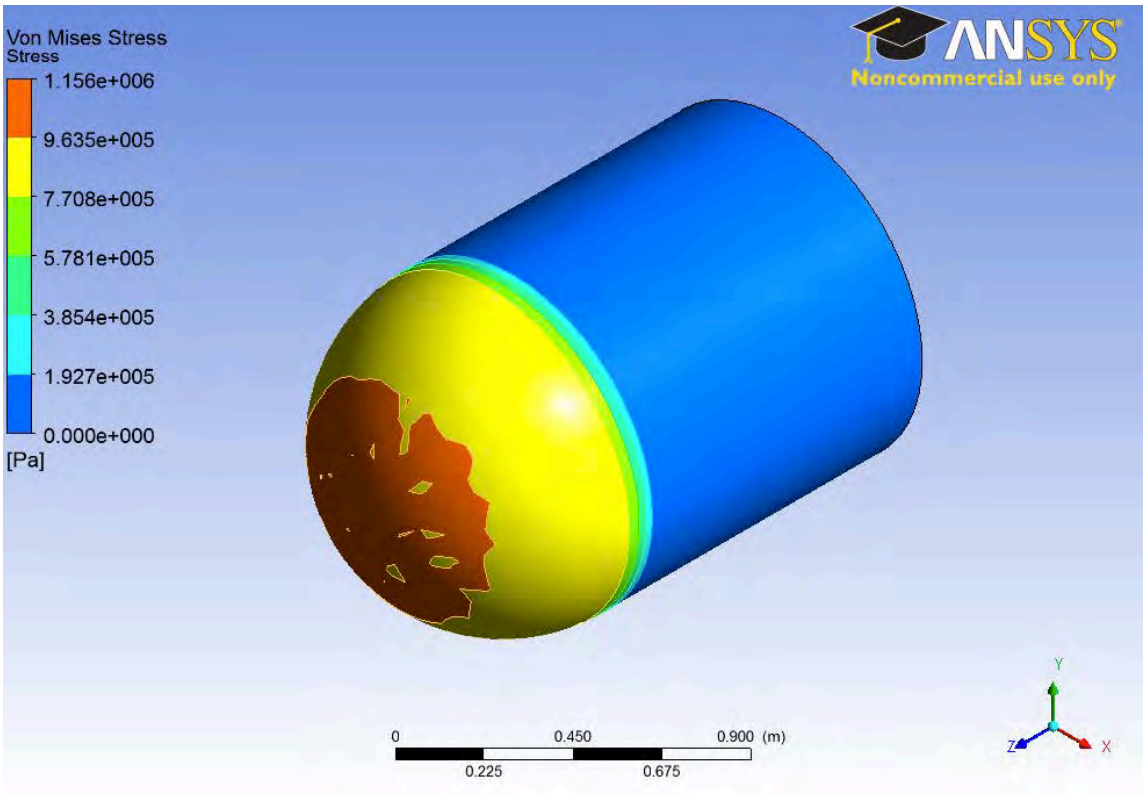

Figure 49. Geometric Variation, Cylinder Peak Stress Location.

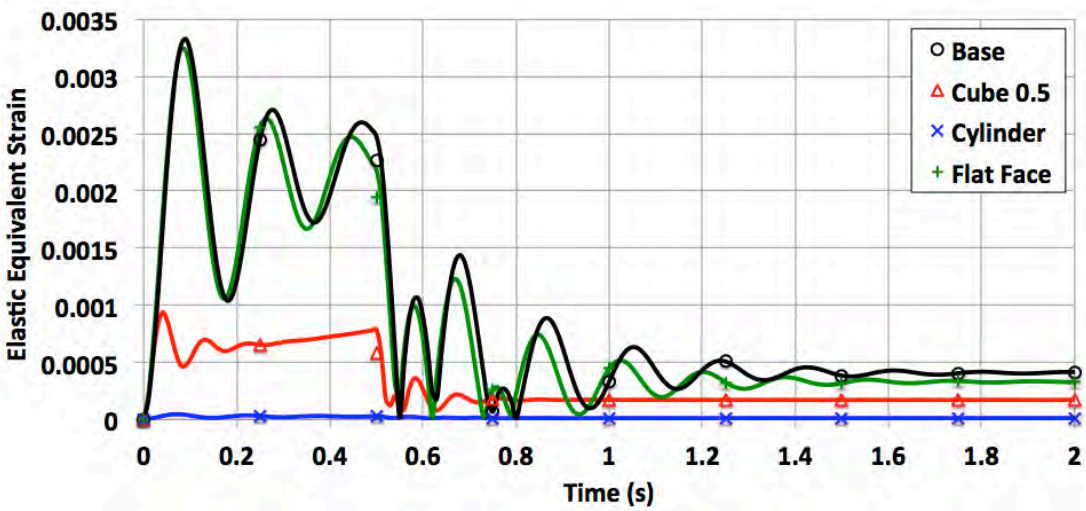

Figure 50. Geometric Variation, Strain at Peak Node.

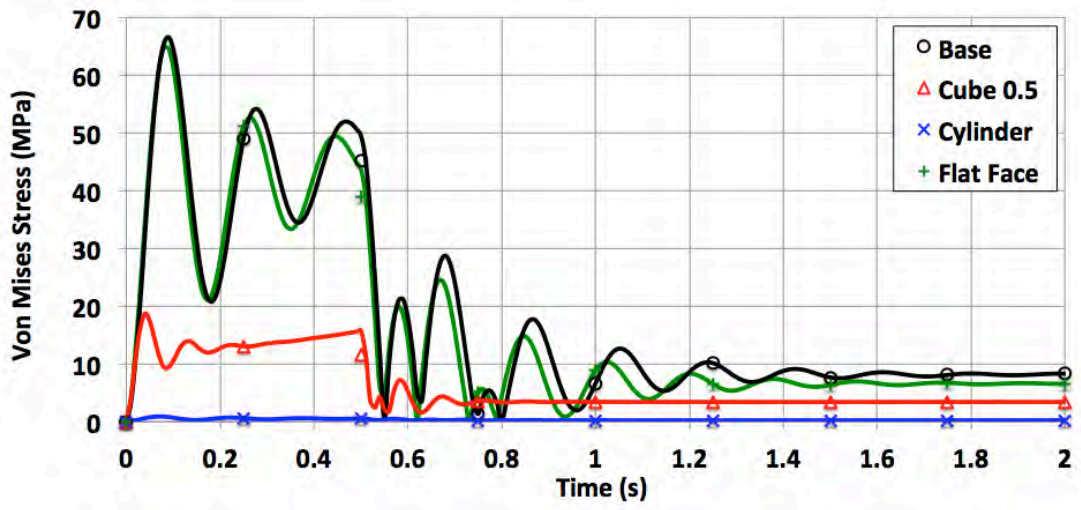

Figure 51. Geometric Variation, Stress at Peak Node.

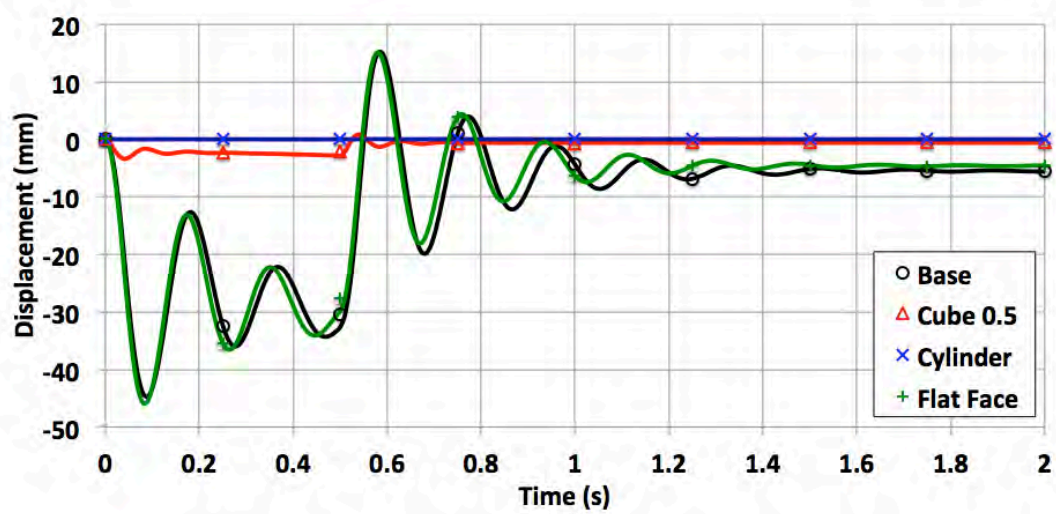

Figure 52. Geometric Variation, Displacement at Center Node.

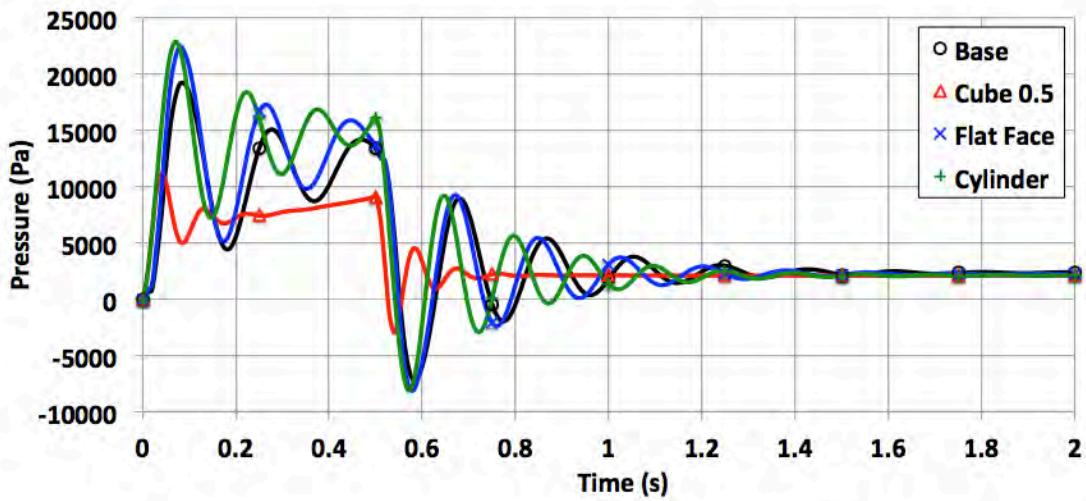

Figure 53. Geometric Variation, Pressure at Center Node.

Of the four models compared in this case, the base model experienced the highest peak stresses at approximately the same time as the flat face (cylinder) model and these were only slightly higher. Although both models were one meter wide, the base model had a slightly larger surface area and received more hydraulic force than the flat face model. Both models had similar oscillatory responses to changes in velocity that correspond with previous cases.

The cube 0.5 had significantly reduced stresses in all areas compared to the base model. The reduced size of the cube offered additional support by the fixed sides and further reduced displacement compared to the base model. Additionally, the surface area is one quarter of the base model and therefore exposed to less fluid pressure as shown in Figure 53. In this model displacement was independent of fluid acceleration and max displacement was reached at 0.04 seconds vice 0.09 seconds for the base model. Oscillations were also significantly reduced and quickly decayed due to the minimal deflection.

The last model under consideration was the one-meter diameter cylinder with a 0.5-meter dome on the front side. This geometry provided significantly lower stresses

than anything evaluated in previous models. The curved dome adds structural rigidity and minimizes hydrodynamic forces. Oscillations were seen when plotted alone, but they are negligible in comparison to any of the other cases.

Table 9. Geometric Variation, Case Summary.

	Cylinder	Flat Face	Base	Cube 0.5
	Elastic Equivalent Strain			
Maximum	0.000045	0.003230	0.003328	0.000934
Steady State	0.000012	0.000329	0.000409	0.000170
Ratio	3.91	9.80	8.12	5.47
	Von Mises Stress (MPa)			
Maximum	0.9	64.6	66.6	18.7
Steady State	0.2	6.6	8.2	3.4
Ratio	3.91	9.81	8.12	5.47
	Displacement (mm)			
Maximum	0.032	45.789	44.700	3.423
Steady State	0.008	4.621	5.538	0.630
Ratio	3.78	9.91	8.07	5.43
	Pressure (Pa)			
Maximum	22,906.00	22,484.30	19,162.80	11,113.60
Steady State	2,115.86	2,237.21	2,373.36	2,106.89
Ratio	10.83	10.05	8.07	5.27

From the calculated transient to steady state ratios in Table 9, the cylinder had the largest pressure ratio but the lowest force ratios. This is because the dome has the largest

surface area exposed to the fluid but also significantly higher structural rigidity and better flow characteristics. Cylinder steady state displacement was 8 μm compared to 5 mm for the base model. The cube 0.5 had smaller ratios than the base model and proved that smaller objects have a smaller relative surface area for hydrodynamic forces and additional rigidity. The flat front model ratios were slightly higher than the base model and the magnitude of forces involved were similar to the other cases discussed.

The cube 0.5 and cylinder also provide unique perspectives on peak stress ratios. The two models both share increased structural rigidity. The cylinder is reinforced by properties inherent to a sphere and the cube due its increase edge stiffness with respect to surface area. Applied fluid forces are dependent on surface area and in this case the cylinder has the largest surface area of 1.57 m^2. However, it resulted in the lowest stresses of any of the cases presented. The base and flat front models have areas of 1 m^2 and 0.785 m^2 respectively, and receive comparable peak stress ratios. Cube 0.5 has a surface area of 0.25m^2, is one quarter the size of the cube, yet has a peak stress ratio of 32 percent lower than the base, most likely due the steady state displacement being one-ninth of the base. The advantages of a curved surface cannot be understated with respect to structural integrity and its widespread use in naval and aeronautical applications is justified.

G. MATERIAL PROPERTY VARIATION

This case presented three different representative composite materials subject to the same boundary conditions and acceleration profile as the base model. The base model was configured for a density of 2000 kg/m^3 and Young's modulus of 20 GPa, while the first and second cases changed Young's modulus to 50 GPa and 100 GPa respectively and the third changed density to 3000 kg/m^3 and Young's modulus to 50 GPa. Figures 54, 55, 56 and 57 plot upper node stress and strain, and center node displacement and pressure versus time.

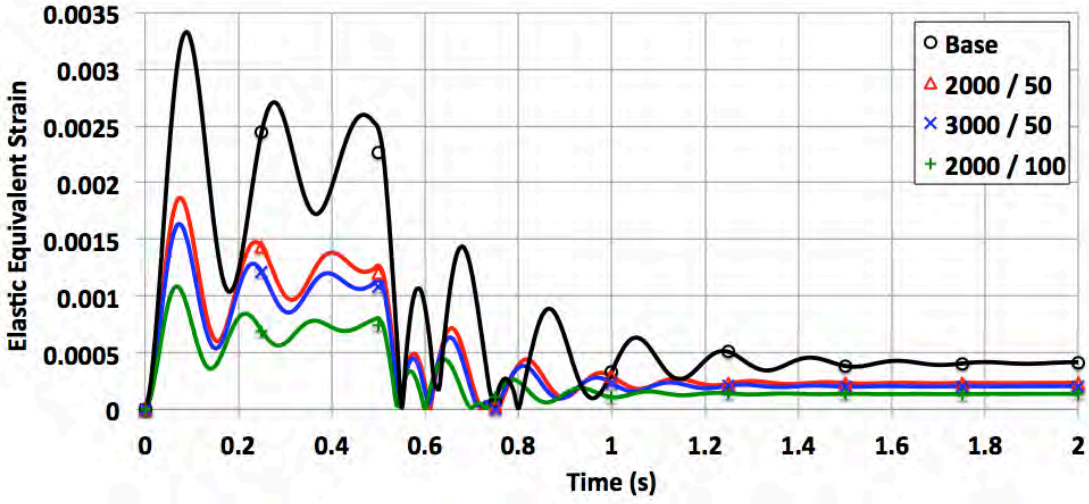

Figure 54. Material Property Variation, Strain at Upper Node.

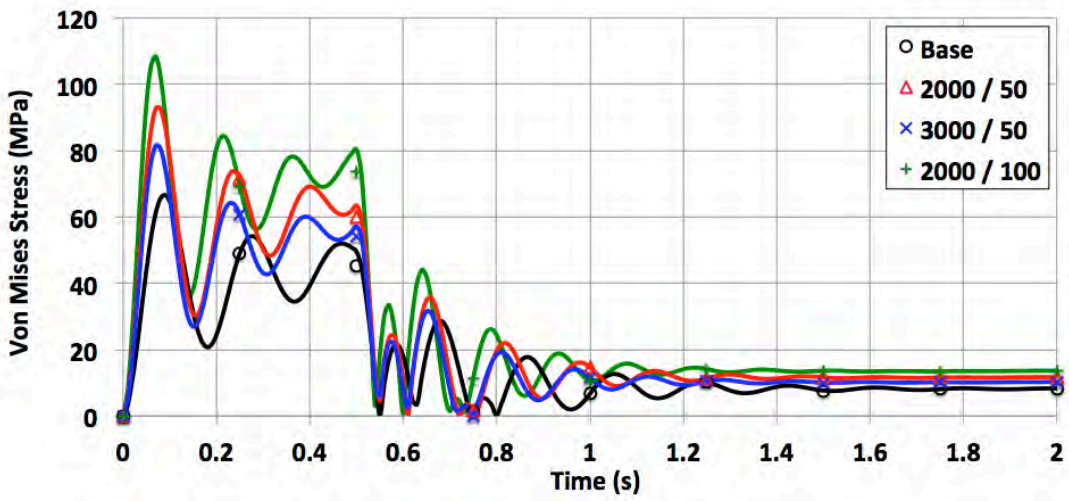

Figure 55. Material Property Variation, Stress at Upper Node.

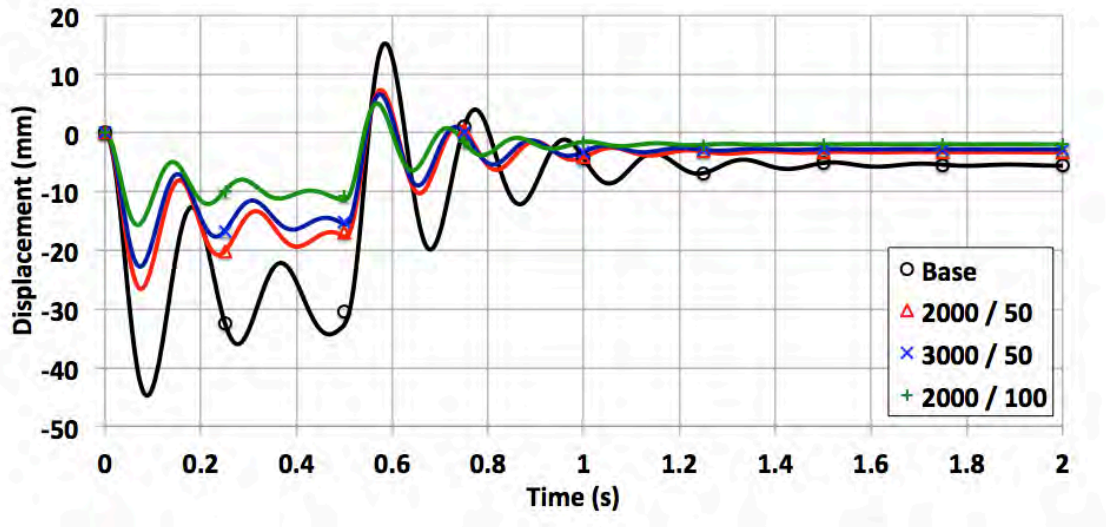

Figure 56. Material Property Variation, Displacement at Center Node.

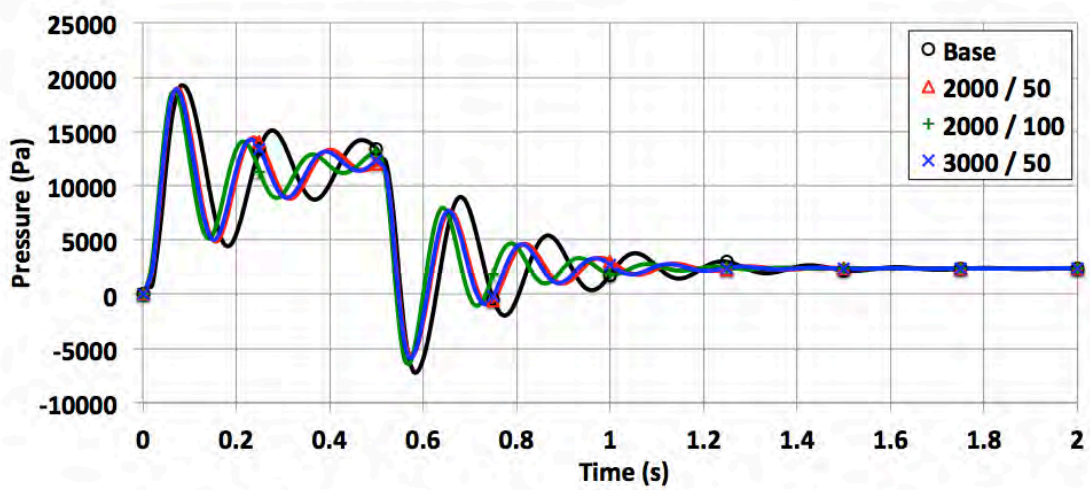

Figure 57. Material Property Variation, Pressure at Center Node.

Peak stresses for the base model occurred at 0.08 seconds while all others occurred at 0.07 seconds. Oscillatory response was similar to the base model for all cases although the three comparative cases showed increased damping in the final 0.25 seconds of acceleration, which correlates with the lower initial displacements. Peak forces were recorded and compared to steady state values averaged over the final 0.25 seconds of the simulation (Table 10).

Table 10. Material Property Variation, Case Summary.

	2000 / 50	2000 / 100	Base	3000 / 50
	Elastic Equivalent Strain			
Maximum	0.001853	0.001084	0.003328	0.001629
Steady State	0.000232	0.000136	0.000409	0.000204
Ratio	7.97	7.99	8.12	7.99
	Von Mises Stress (MPa)			
Maximum	92.6	108.3	66.6	81.4
Steady State	11.6	13.6	8.2	10.1
Ratio	7.97	7.99	8.12	7.99
	Displacement (mm)			
Maximum	26.385	15.696	44.700	22.731
Steady State	3.324	1.977	5.538	2.857
Ratio	7.94	7.94	8.07	7.95
	Pressure (Pa)			
Maximum	18,897.60	18,686.30	19,162.80	18,859.60
Steady State	2,383.58	2,383.25	2,373.36	2,381.51
Ratio	7.93	7.84	8.07	7.92

The base model had slightly higher ratios than the other cases. However, there were differences in which cases had peak values, indicating that steady state values had sufficient difference to influence a ratio analysis. The three cases with 2000 kg/m^3 density and varying Young's modulus show a reverse correlation between stress and strain. The base model (Young's modulus: 20 GPa) had the lowest peak stress of 66.6 MPa and the highest strain 0.003328 while model 2000/100 had the highest stress of

108.3 MPa and lowest strain of 0.001084. This aptly displays the relationship between stress and strain. Strain values indicate deformation per unit length whereas stress indicates the force per unit area. The 2000/100 model had a higher Young's modulus than the base model and is therefore stiffer. The resistance to displacement results in a smaller resultant strain but is also prone to a larger stress from the applied pressure as it resists bending. In comparison, the base model works in an opposite manner. Because it is more flexible, it receives higher strains, larger displacements and lower stresses. The remaining model of equal density, 2000/50, performed as a compromise between the 2000/20 (base) and 2000/100 models. The stiffness of the 2000/50 model produced stress, strain and displacement between the base and 2000/100 models as indicated by Figures 54, 55 and 56.

The final model in this case, 3000/50, increased the density to 3000 kg/m^3 and is best suited for a comparison with the 2000/50 model. Both materials had the same Young's modulus leaving density as the remaining variable, best described by its units of kg/m^3 or the amount of material per cubic meter. The 3000/50 model comparatively had more material to assist bending resistance and therefore resulted in lower peak values for stress, strain and displacement.

The design implications of these results indicate a delicate balance between displacement, peak stress and weight. There is no clear winner in that each material has its advantages and disadvantages. Of the materials presented here, the base model has the largest displacement and lowest peak stress, which would not be suitable for large ship hull applications but could be useful as an airfoil where flexibility is acceptable and reduced weight is required. As previously mentioned, the base model closely resembles E-glass which is a fiberglass material often used in avionics. The 3000/50 model performed opposite of the base model and received higher stresses at the expense of reduced displacement and increased weight. Lastly, the force ratios resulting from a transient fluid acceleration are nearly constant throughout the models, which mean material selection is almost entirely application based.

H. DEPTH VARIATION

The simulations represented here include an additional depth variable for comparison to the base model. The 1-meter model mirrors the base model except with the inclusion of a free surface, while the 2-meter and 3-meter models include the free surface and also increase distance from the free surface by two and three meters respectively. The dimensions and boundary conditions on exterior sides of the fluid domain were constant and therefore horizontal symmetry about the center vertical plane is preserved. Addition of the free surface eliminates vertical plane symmetry and several data points along the center vertical plane of the cube required comparison (Figure 58).

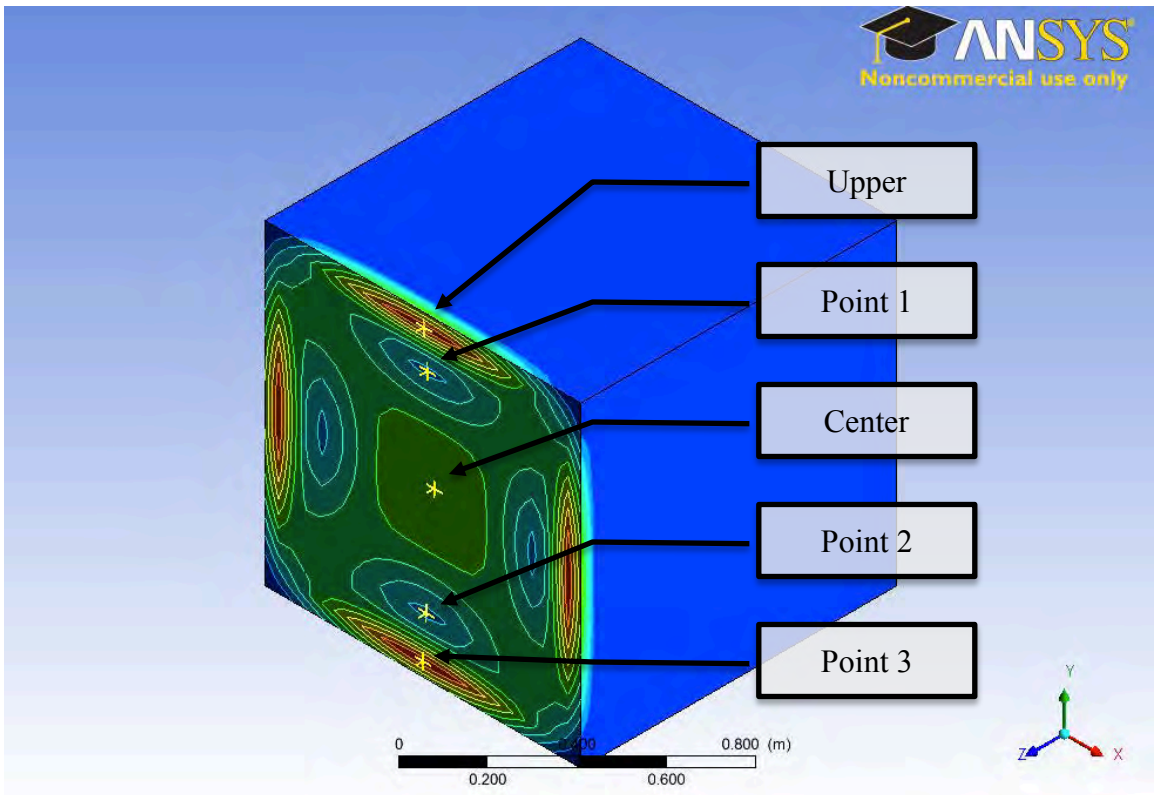

Figure 58. Depth Variation, Nodal Evaluation Points.

Base model results revealed that boundary conditions preserved fluid and structural domain symmetry. Fluid pressures were highest at the inlet and decreased as velocity around the cube increased which Bernoulli [9] has proven to be a fundamental component in fluid theory. Stress also remained symmetric at the interface, which was

expected due to the FSI. Figure 59 shows the fluid pressure along the center plane with a callout for interface stress at the peak force time of 0.09 seconds.

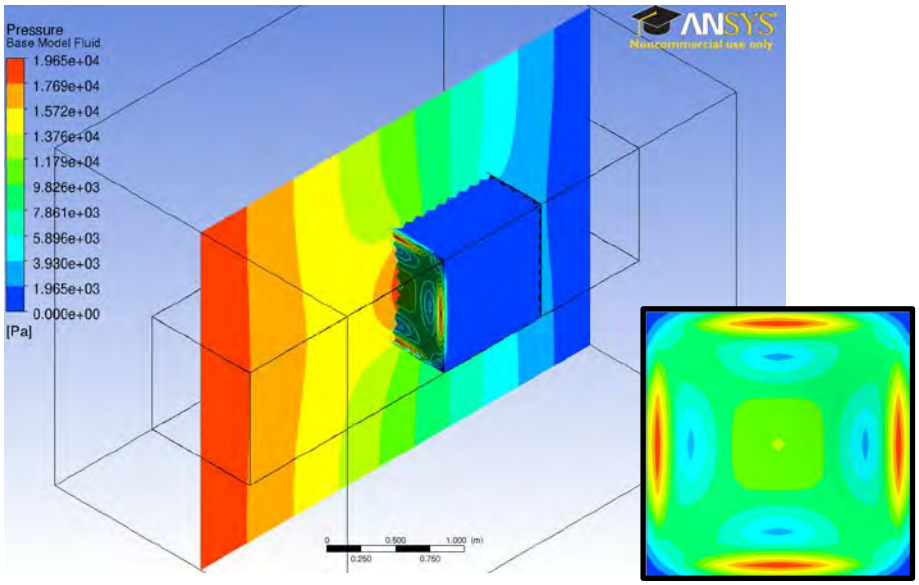

Figure 59. Base Model, Peak Pressure with Interface Stress Callout.

Although the time for peak pressure occurred only slightly before the base model at 0.07 seconds, the 1-meter model resulted in a far different response due to the significant effects of the free surface. Fluid along the upper half moved freely and resulted in much lower pressures above the cube. This also reduced the hydraulic forces applied to the interface, which reduced material stress (Figure 60).

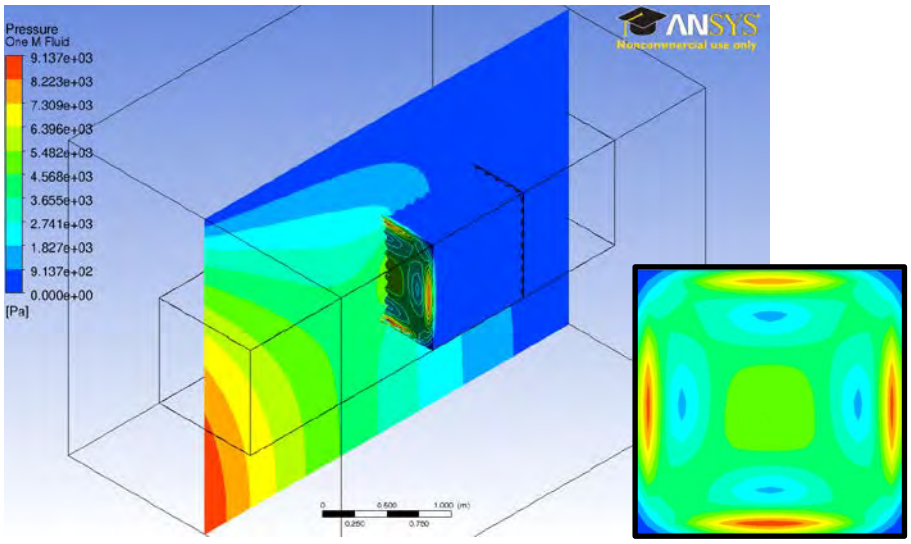

Figure 60. 1-Meter Model, Peak Pressure with Interface Stress Callout.

While the base model represented an infinite depth and 1-meter model the shallowest depth, they established a trend that both 2-meter and 3-meter model results followed. The 2-meter and 3-meter model showed increased fluid pressure in the region above the plate indicating that the depth rise increased plate pressure and interface stress. Peak fluid and stress pressures are shown in Figure 61 for the 3-meter model at the peak time of 0.08 seconds.

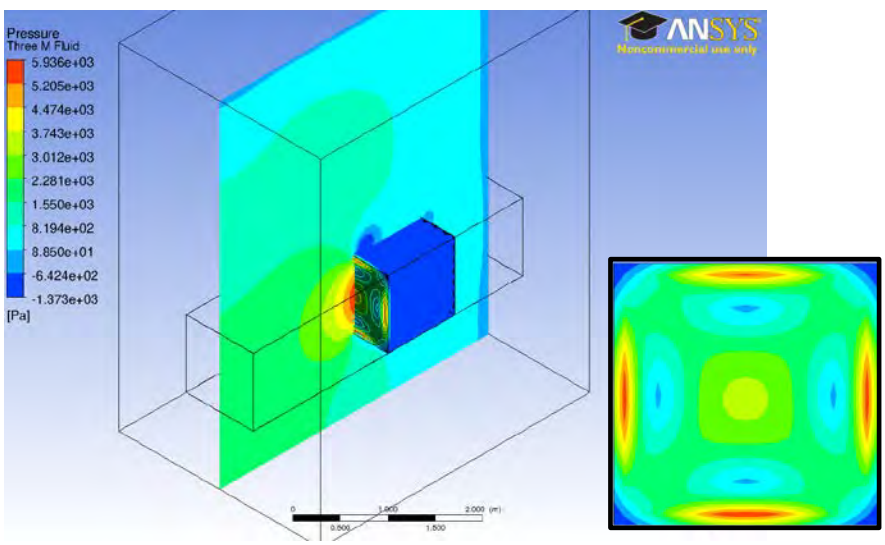

Figure 61. 3-Meter Model, Peak Pressure with Interface Stress Callout.

In order to evaluate the effects of depth on the interface, average interface pressure was selected to assess hydrodynamic forces over the entire interface. Figures 62, 63, 64 and 65 show strain, stress, and displacement for the upper node and average pressure over the interface. Figures for point 1, center, point 2 and point 3 forces are shown in Appendix D.

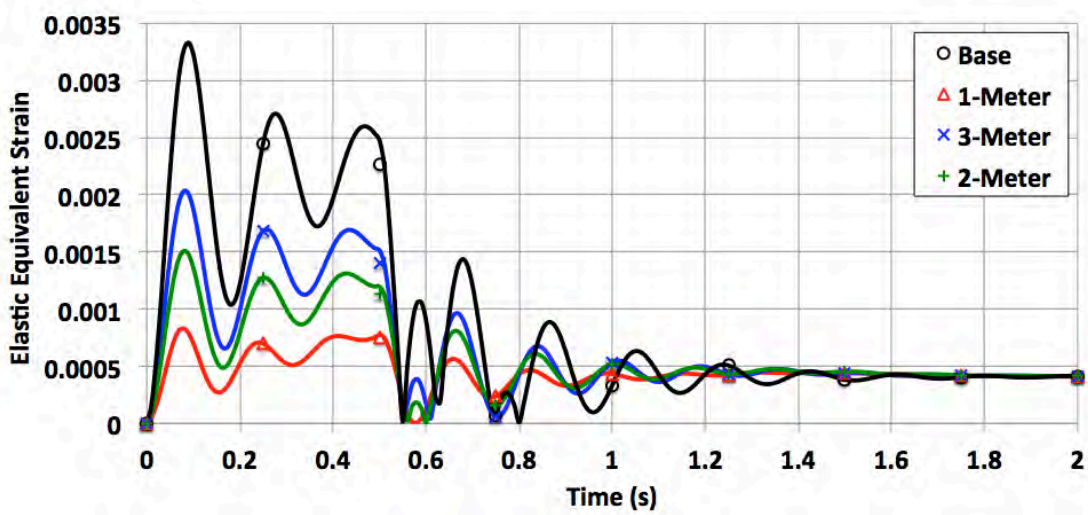

Figure 62. Depth Variation, Strain at Upper Node.

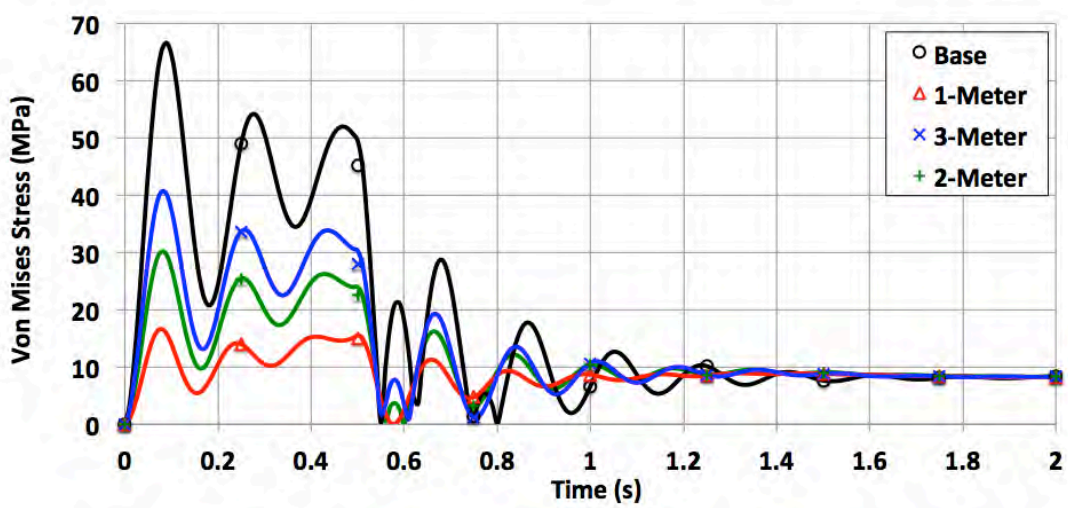

Figure 63. Depth Variation, Stress at Upper Node.

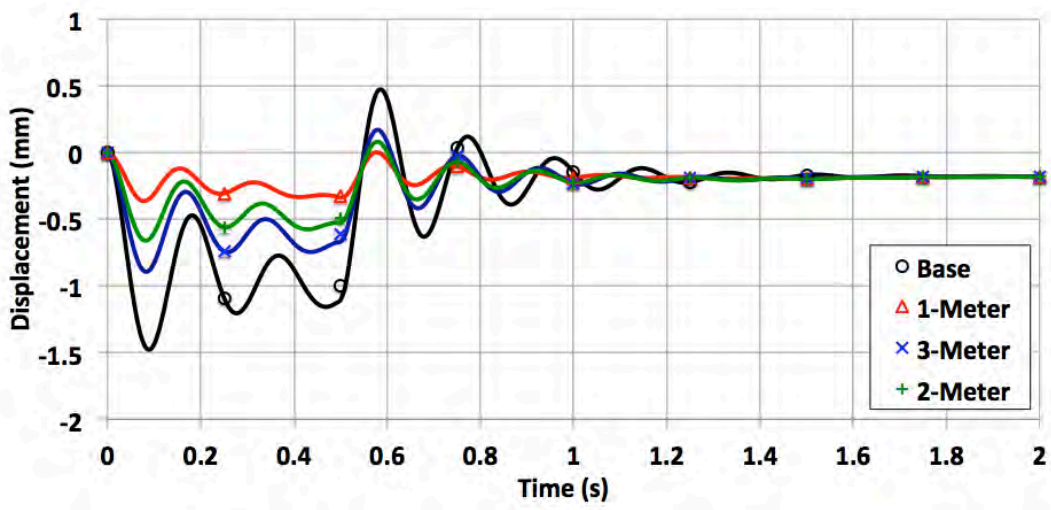

Figure 64. Depth Variation, Displacement at Upper Node.

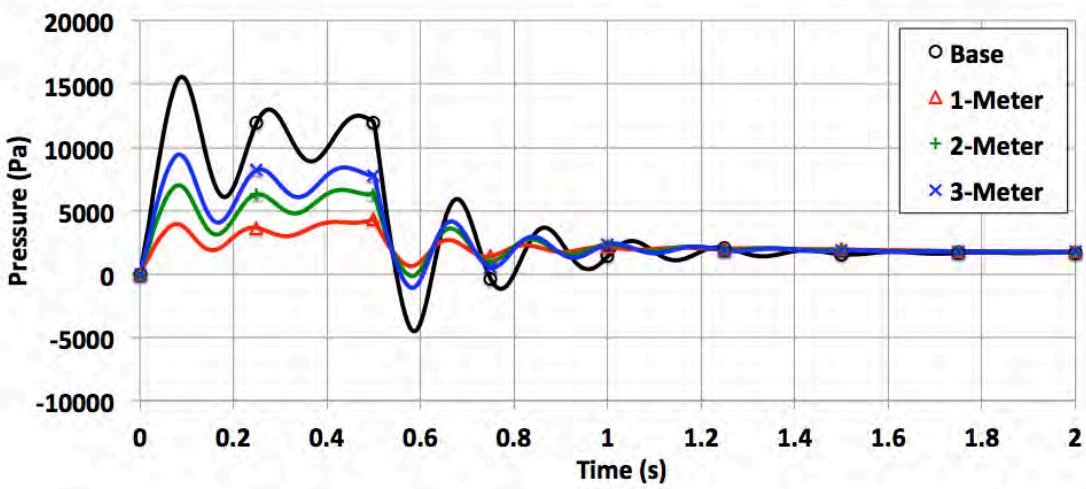

Figure 65. Depth Variation, Average Pressure at Interface.

The transient pressure profiles (Figure 65) depict the large effects of having a free surface. In the base model, symmetric boundary conditions force fluid to flow evenly about all sides of the cube and result in a greater applied pressure. The 1-meter model represents the shallowest case; the largest portion of fluid is allowed to pass over the top of the cube, resulting in the lowest pressures. Both 2-meter and 3-meter models further verify this principle and have higher pressures than the 1-meter model but lower than the base model.

Stress, strain and displacement responded as seen in previous cases with peaks corresponding to oscillations at the onset and securing of acceleration. The 1-meter model showed decaying oscillations that correlate with a reduced initial displacement. The 1-meter model oscillation decay closely resembled those seen in the variation in constant acceleration, 2 m/s at 1s case.

A maximum to steady state value comparison was also completed to facilitate a comparison of the base, 1-meter, 2-meter and 3-meter models. Abbreviated tables comparing upper node stress ratios and displacement across the four models are provided in Tables 11 and 12. Previous cases have shown that stress and strain have exactly the same ratios and have therefore been combined in Table 11. Detailed information of all maximum and steady state forces for all sample locations is presented in Appendix D. Table 13 lists the maximum and steady state average pressure ratios at the interface.

Table 11. Depth Variation, Stress and Strain Ratio Case Summary.

	Base	1-Meter	2-Meter	3-Meter
Upper	8.12	2.01	3.61	4.91
Upper-Mid	8.02	2.16	3.82	5.11
Center	8.09	2.18	3.87	5.19
Lower-Mid	8.03	2.17	3.79	5.09
Lower	8.12	2.26	3.75	5.02

Table 12. Depth Variation, Displacement Case Summary.

	Base	1-Meter	2-Meter	3-Meter
Upper	8.18	2.00	3.60	4.91
Upper-Mid	8.10	2.02	3.62	4.92
Center	8.07	2.12	3.75	5.04
Lower-Mid	8.10	2.24	3.75	5.02
Lower	8.18	2.31	3.76	5.03

Table 13. Depth Variation, Average Pressure at Interface Case Summary.

	Average Pressure At Interface (Pa)			
	Base	1-Meter	2-Meter	3-Meter
Maximum	15,574.0	4,292.4	7,008.8	9,409.7
Steady State	1,688.6	1,771.0	1,752.7	1,746.6
Ratio	9.22	2.42	3.99	5.38

These ratios correlate with the conclusions observed from corresponding figures of this section. The base model received the highest force ratio and was symmetric about the center. The 1-meter model the smallest ratio at the upper sample point and increased along the face. Ratio trends for 2-meter and 3-meter models also tracked accordingly with depth. These results indicate that increased depth dampens free surface effects and increases applied hydrodynamic forces.

In this case, all simulations resulted in steady state displacement values within +/- 0.1 mm across selected nodes in the vertical plane, which allows normalization of peak displacement data and a graphical displacement representation. In order to complete a symmetric analysis about the horizontal center, additional sample locations were taken at

one-sixth meter intervals along the vertical centerline. Steady state values were then subtracted from maximum displacement values and plots of normalized displacement versus sample locations were generated for the four models (Figure 66). The maximum and minimum vertical axis positions represent the extreme upper and lower interface edges where the applied boundary conditions require zero displacement. The normalized displacement curves represent an exaggerated cross-section view of maximum interface deflection.

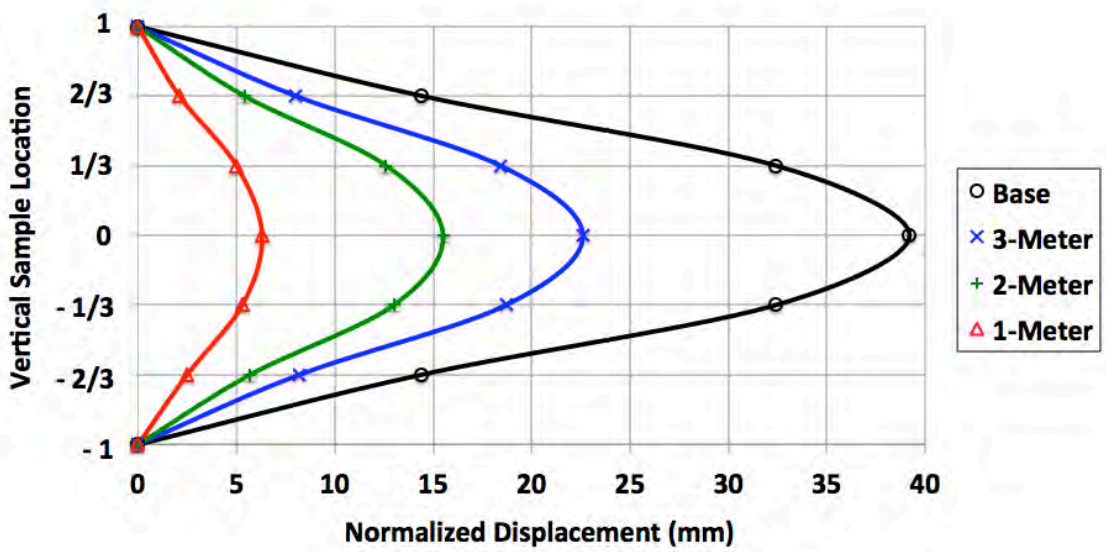

Figure 66. Depth Variation, Normalized Interface Displacement.

The 1-meter model indicates a slight reduction in displacement at the two thirds interface location and correlates with previous observations concerning the force reduction near the free surface. Additionally, the base model was determined to be symmetric in horizontal and vertical planes and also correlates with the displacement curve. However, a numerical representation provides a more accurate view of comparative model interface displacement. Using a linear approximation between sample node locations, the area for each displacement curve was calculated and then further separated into upper and lower regions about the horizontal center plane (Table 14).

Table 14. Depth Variation, Centerline Displacement Area (mm^2).

	1-Meter	2-Meter	3-Meter	Base
Upper	3.42	8.58	12.57	22.13
Lower	3.65	8.81	12.73	22.13
Delta	-0.23	-0.23	-0.16	0

The results shown in the Table 14 mathematically verify earlier observations. Base model displacement proved to be symmetric about the center horizontal plane and matched calculated ratio symmetry. The 1-meter simulation showed less displacement in the upper half compared to the lower half that is indicative of lower hydrodynamic forces in the upper half and further verified by a constant decreasing trend in displacement ratios. This trend continued in the 3-meter model and an upper-lower delta between those determined in 1-meter and base models was observed. Although the 2-meter model yielded the same delta as the 1-meter model, hydrodynamic forces in the upper region were still lower (Appendix D) and validate free surface effects.

Together these simulations reveal the drastic pressure-reducing effects of surface proximity. The 1-meter model peak stress ratios were one quarter that of the base model indicating that materials used in surface ships are less prone to transient acceleration stress than for subsurface vessels.

While the 1-meter model proves useful for surface verification, the base model has comparative value for subsurface applications as well. Base model configurations reflected those of an object at infinite depth. However, a direct comparison was impossible without additional information. Sun's [10] PhD dissertation investigated energy scavenging from tidal forces and reported that normalized velocity deficits in the water column decrease to near zero as depth exceeds seven meters. To verify Sun's conclusion three additional models were completed simulating depths at 5, 7 and 9 meters and resulted in stress ratios of 6.80, 7.51 and 7.76 respectively. Figure 67 plots peak stress ratios versus depth for 1-meter, 2-meter 3-meter, 5-meter, 7-meter and 9-meter simulations with an additional trendline ($R^2 = 0.999$). When placed at seven meters as

suggested by Sun, the base model was within seven percent of the trendline predicted by this study. This reduces to four percent at nine meters and finally three percent at 12 meters.

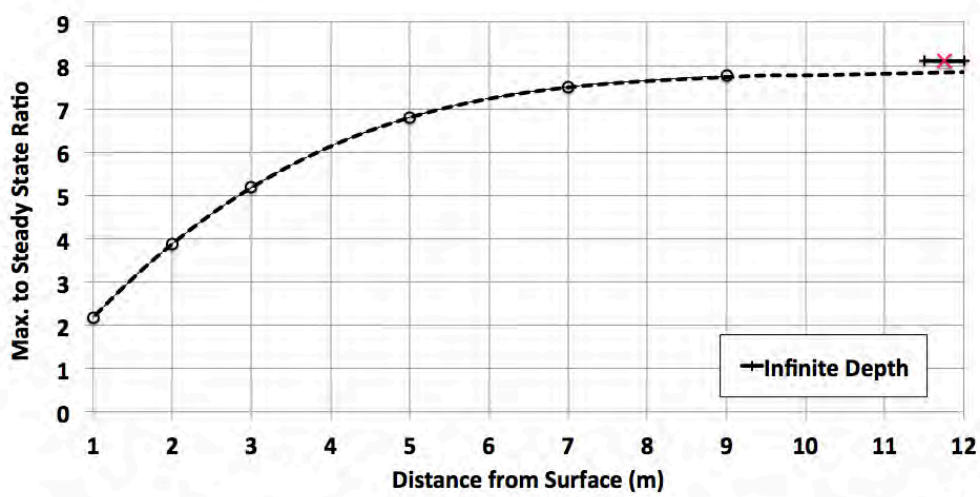

Figure 67. Depth Variation, Ratio Comparison.

This data suggests that transient acceleration stress ratios are increasing to a depth of seven meters and upon exceeding that depth stress ratios become constant and are solely dependent on the acceleration profile. As previous cases have demonstrated, different acceleration profiles can have significantly higher stress ratios; however, this case has revealed that at greater than seven meters the ratio can be assumed constant for a given acceleration profile.

VI. CONCLUSIONS AND RECOMMENDATIONS

A. CONCLUSIONS

The base model was the primary comparative simulation for all cases and received a maximum peak stress of 66.6 MPa, displacement of 44.7 mm, pressure of 19.1 kPa and strain of 0.0033. The peak transient force was determined to be eight times larger than the steady state force, which validates the initial concerns presented in this report. The maximum fluid pressure occurred at 0.09 seconds, which corresponds with the first negative oscillation peak.

Oscillatory patterns were established with the base model and compared to the other cases. The base model responded to a transient acceleration with a series of negative plate oscillations that began with the onset of acceleration and decayed as long as acceleration was constant. Immediately following the transient period, velocity became constant and oscillations peaked in the positive direction and decayed to steady state values. Most cases presented herein tracked base model oscillations and showed large negative initial displacements that decayed with time and then peaked again when constant velocity was achieved. However, the 4-step simulation resulted in the peak stress of 114.6 MPa and a ratio of 14.06 that occurred at 0.24 seconds (vice 0.09 seconds for base model) and during the second period of zero acceleration. This shows the relative significance of successive acceleration periods combined with increased acceleration rates as they cause stress levels far higher than expected.

The highest transient stress occurred in the 2 m/s at 0.25s simulation, which peaked at 0.09 seconds with 133.3 MPa. Conversely, the lowest peak transient stress occurred in the cylinder model with 0.9 MPa at 0.08 seconds. Additionally, the variation in terminal velocity cases indicate that transient peak stress is independent of terminal velocity but rather dependent upon the acceleration rate as shown by the variation in constant acceleration models. The depth variation cases clearly indicate that hydraulic force increases with depth. When considered together, these data points suggest that the

forward center-most region of a submarine operating at depth depicts the maximum conditions susceptible to the hydraulic forces induced by rapid transient accelerations.

Throughout the study, most cases performed as expected when compared to the base model and was most obvious in the linear relationship between the constant acceleration simulations. However, the peak transient forces determined when terminal velocity is lowest pose the greatest risk for oversight because the expected steady state stress is 14.5 times lower than the peak stress as shown in the 1.5 m/s at 0.38 simulation. The 2000/100 composite material model predicted a peak transient stress of 108.3 MPa for a constant acceleration with a terminal velocity of 2 m/s. If this material were to be used for structural design in a slow speed application based solely on steady state velocity stress, failure could be possible under these specific conditions.

Although varying degrees of peak transient stress ratios were determined while conducting this research, every simulation evaluated showed increased hydraulic forces experienced during a transient fluid velocity. This validates the necessity to include this unique focus area in certain maritime design applications. Unmanned underwater vehicles (UUVs) can readily incorporate the use of composite materials. The UUVs generally travel at slow speeds below five knots (2.5 m/s) and could be exposed to similar acceleration transients as those modeled in this research, especially step acceleration and monotonic acceleration cases. The results of this study indicate the need to include transient forces in the design process and the operating conditions of a UUV present the optimal transient velocity profiles under which these conditions might apply.

Although not a focal point for this report, the base model peak transient force was also compared to the average transient force from 0 – 0.5 seconds resulting in a peak-to-mean force ratio of 1.61. Additionally, the highest peak-to-mean force ratio was the monotonically decreasing model with a value of 2.66, while the lowest ratio was the Cube 0.5 model which had a 1.41 ratio. The average peak-to-mean force ratio for all cases considered herein was 1.88, excluding depth variation cases because the maximum force did not occur at the center. Despite the huge dissimilarity between simulations and

their application, Tehrani, Rakheja and Sedaghati [3] determined a peak-to-mean ratio of 1.57 which was similar to base model results and the global average determined in this research.

B. RECOMMENDATIONS

A good engineering practice is to verify analytical results with an empirical model. The NPS tow tank verification, discussed in Chapter II, presented a foundation for the opportunity to replicate structural response using a computer simulated FSI. However this comparison, while valid, had fundamental differences between empirical and analytical models (such as fluid motion versus solid body motion) that could not readily be overcome. Although the submerged stationary cube evaluated here cannot be physically replicated, empirical testing would be possible with minimal adjustments to this model. Addition of a fixed support extending from the rear face of the cube could connect the cube to a solid exterior surface and facilitate empirical testing in a wave tank capable of achieving transient fluid velocities. Utilizing the composite-fiber feature offered by ANSYS to better replicate E-glass could also enhance results acquired from the analytical model.

This research has generated a foundation for E-glass performance; completing simulations on a wider range of materials (steel or aluminum) could produce similar peak transient force profiles that would be useful to designers. Finally, this research only predicted the results from transient acceleration, and transient deceleration forces could be modeled for comparative severity.

THIS PAGE INTENTIONALLY LEFT BLANK

APPENDIX A. BASE MODEL GENERATION

Base model development began with opening a new Workbench project and addition of a transient structural and fluid flow (CFX) work processes to the project schematic. The transient structural geometry and setup cells were shared with their corresponding cell in CFX (Figure 68). This connection establishes the strongly coupled interaction between solid and fluid domains.

Figure 68. ANSYS Workbench, 2-Way FSI Connection.

The next step was addition of material properties in transient structural. Since the base model predicted the performance of E-glass, a composite material with structural properties closely represented by one with a density of 2000 kg/m^3, Poisson ratio of 0.3 and Young's modulus of 20 GPa were added to the transient structural engineering data cell (Figure 69).

	A	B	C	D
1	Contents of Engineering Data		Source	Description
2	Material			
3	Plate			
4	Structural Steel			Fatigue Data at zero mean stress comes from 1998 ASME BPV Code, Section 8, Div 2, Table 5-110.1
*	Click here to add a new material			

Properties of Outline Row 3: Plate

	A	B	C	D	E
1	Property	Value	Unit		
2	Density	2000	kg m^-3		
3	Isotropic Elasticity				
4	Derive from	Young's Mo...			
5	Young's Modulus	2E+10	Pa		
6	Poisson's Ratio	0.3			
7	Bulk Modulus	1.6667E+10	Pa		
8	Shear Modulus	7.6923E+09	Pa		

Figure 69. E-Glass Engineering Data.

Two commonly used methods for geometry fabrication and integration within ANSYS are SolidWorks and ANSYS Design Modeler. SolidWorks is fully capable Computer Aided Drafting software useful for generating complex 3D geometries and predicting motion and fluid flows [11]. Design Modeler provides similar 3D geometric fabrication and is already embedded within the ANSYS architecture. The strongly coupled solid and fluid domains and ability to readily modify an existing geometry made Design Modeler an appropriate choice for this study.

The base model structure was a 1 m^3 box surrounded by one cubic meter of fluid on the back and sides, and two meters extending forward. The solid body was created by definition of lower- and upper-diagonal coordinates and configured to be a surface body with zero thickness. To facilitate mesh generation, subtraction of solid from fluid geometries was necessary and completed by conducting several Boolean subtractions. A refined mesh at the fluid-solid interface was necessary to support FSI and therefore the fluid domain was further separated into outer and inner regions corresponding to the size of the solid (Figure 70).

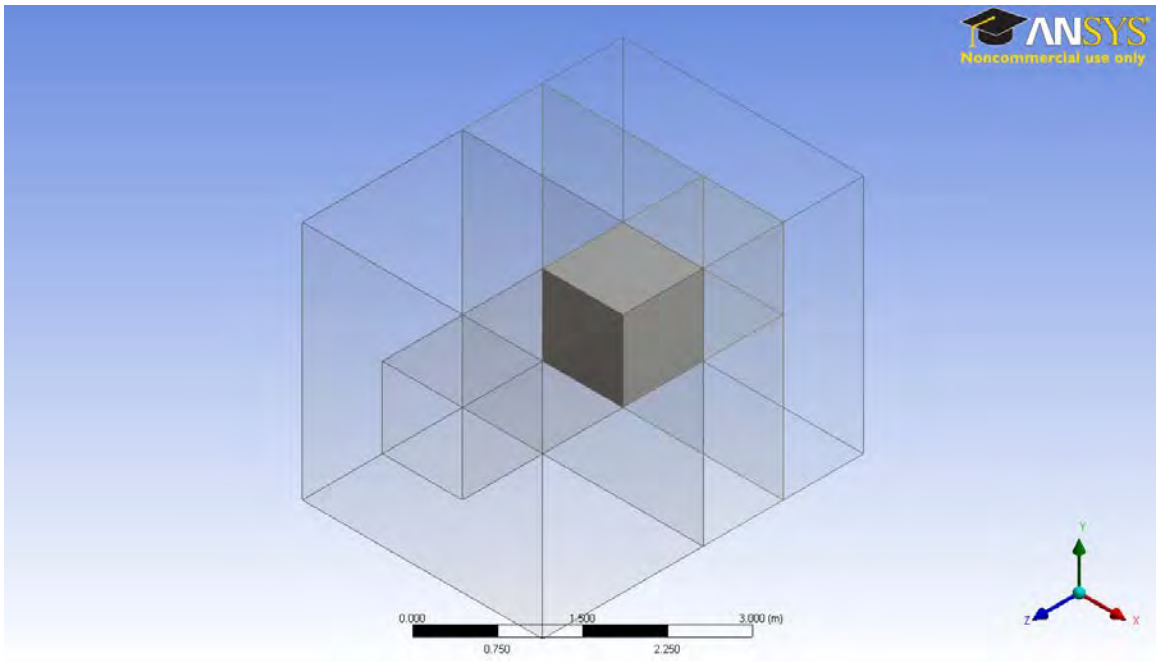

Figure 70. Base Model Geometry.

Following geometry fabrication, model creation proceeded into the transient structural model cell where the structural domain was defined. The cube was modeled as a surface body and given an additional shell element configuration. Surface bodies reduce problem complexity, add stability to the mathematical solver and reduce run times while maintaining accuracy [2]. The shell element was assigned by inserting *kepyopt.matid, 3, 2* into a Command ADPL prompt for the surface body. The density of water is approximately 1000 times larger than air and its resistance was expected to have a negligible contribution to accuracy. This assumption eliminated the need for fully defined 3D structural model and its exclusion drastically simplified the simulation.

Meshing was completed using a quadrilateral dominant automatic method with meshing parameters shown in Figure 71, and resulted in 3,458 nodes and 3,456 elements. The end result created a 24 x 24 grid of elements 0.04167 cm in length. Additional settings include selection of the front face as an Interface boundary and the remaining five sides as fixed supports (Figure 72).

Sizing	
Use Advanced Size Function	On: Proximity
Relevance Center	Fine
Initial Size Seed	Active Assembly
Smoothing	Medium
Transition	Fast
Span Angle Center	Fine
Proximity Accuracy	0.5
Num Cells Across Gap	50
Proximity Min Size	Default (4.1771e-002 m)
Max Face Size	Default (0.208850 m)
Growth Rate	Default
Minimum Edge Length	1.0 m
Inflation	
Patch Conforming Options	
Advanced	
Defeaturing	
Statistics	
Nodes	3458
Elements	3456
Mesh Metric	None

Figure 71. Transient Structural Mesh Configuration.

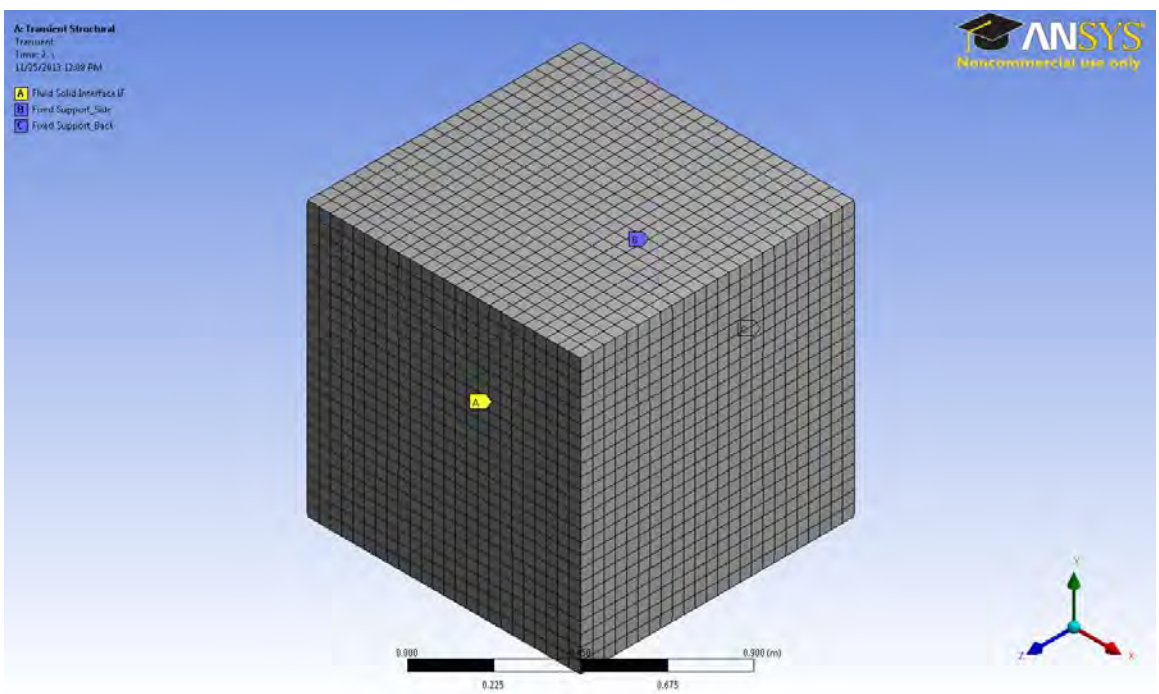

Figure 72. Transient Structural Mesh.

Base model creation continued in CFX-Pre with fluid domain mesh generation, which required several operations unique to various portions of the fluid domain. The exterior fluid region was meshed with a Sweep method and hex-dominant assignment. Since the interior fluid region contacted the solid body it was necessary to optimize node-to-node connectivity between the two domains. FSIs use values from fluid domain nodes and pass them to corresponding structural domain nodes. Nodal misalignment requires the solver to linearly approximate appropriate mid-node force values for opposing nodes thereby increasing solution time and adding instability. Nodal connectivity was precisely matched by meshing interior fluid domains with 0.04167 cm element length Face Sizing, which resulted in a 24 x 24 grid of elements (Figure 73). Combined inner and outer fluid domains had 110,937 nodes and 100,744 elements.

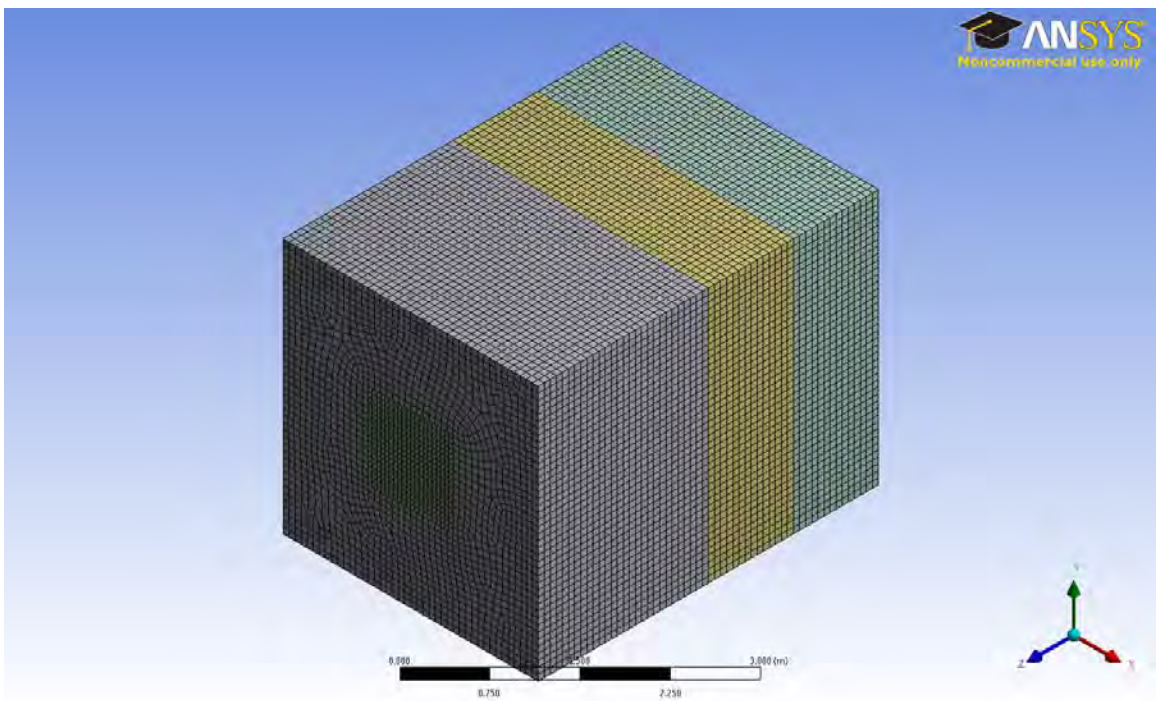

Figure 73. CFX Fluid Mesh.

The fluid domain was configured in the setup up cell of CFX. A zero reference pressure outlet boundary was assigned and an expression was used to define the inlet boundary velocity profile. The remaining default domain received full-slip boundaries, which remove the boundary layer effects of fluid domain exterior surfaces and force the

shell to respond as though immersed in a fluid domain of infinite size and depth. The final domain assignments were interface connections between the exterior and interior fluid domain (Figure 74). Fluid flow entered the field in the horizontal Z-plane and interior domain fluid flow entered the outer domain as fluid progressed around the cube. In order to allow the solver to account for this flow path, connections between the two fluid domains were entered as general force connection interfaces.

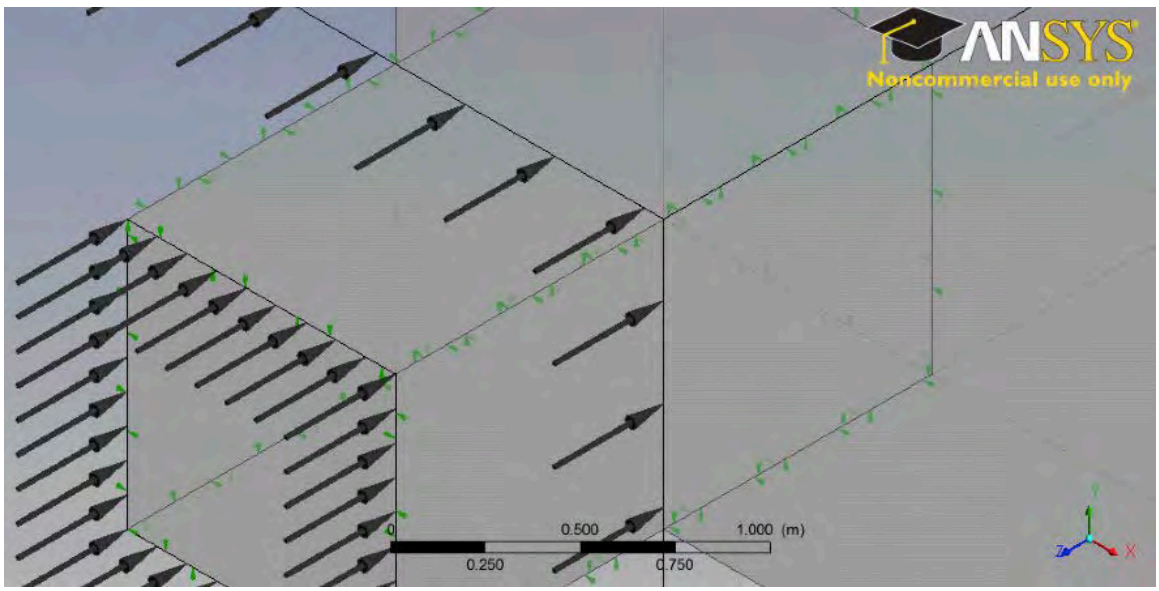

Figure 74. Fluid Domain Interior-Exterior Interface.

Additional CFX-Pre settings configure a transient analysis and periodicity for FSI data transfer to occur at every time step. The FSI boundary was given a mass flux pressure coefficient of two which added minimal mesh damping to mitigate folded mesh errors without compromising solver accuracy [12]. Setting solver residual convergence criteria to $1x10^5$ forced the solver to converge with higher accuracy and mitigated pressure coefficient damping. Finally, the interface was assigned an FSIN number, linking the fluid interface to the corresponding structural interface. Appendix B includes additional images of the CFX-Pre settings discussed in this section.

APPENDIX B. CFX-PRE SUPLEMENTAL FIGURES

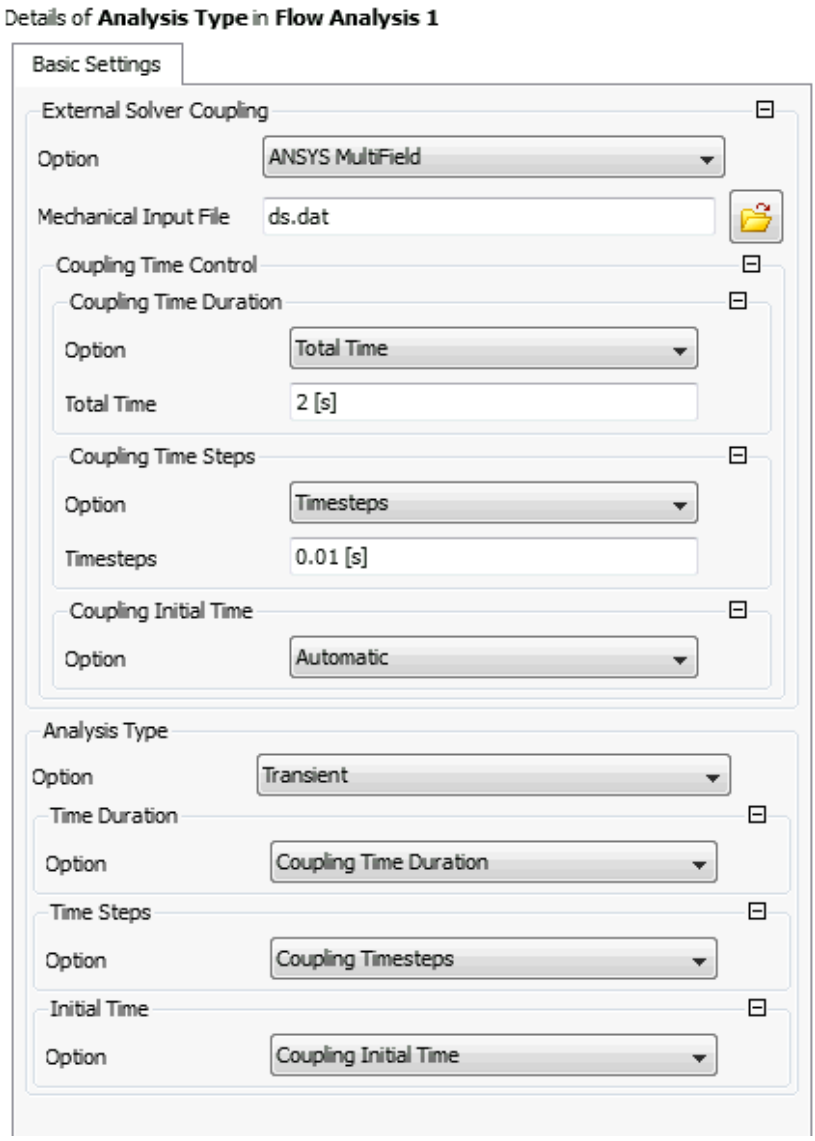

Figure 75. CFX-Pre Analysis Basic Settings Tab.

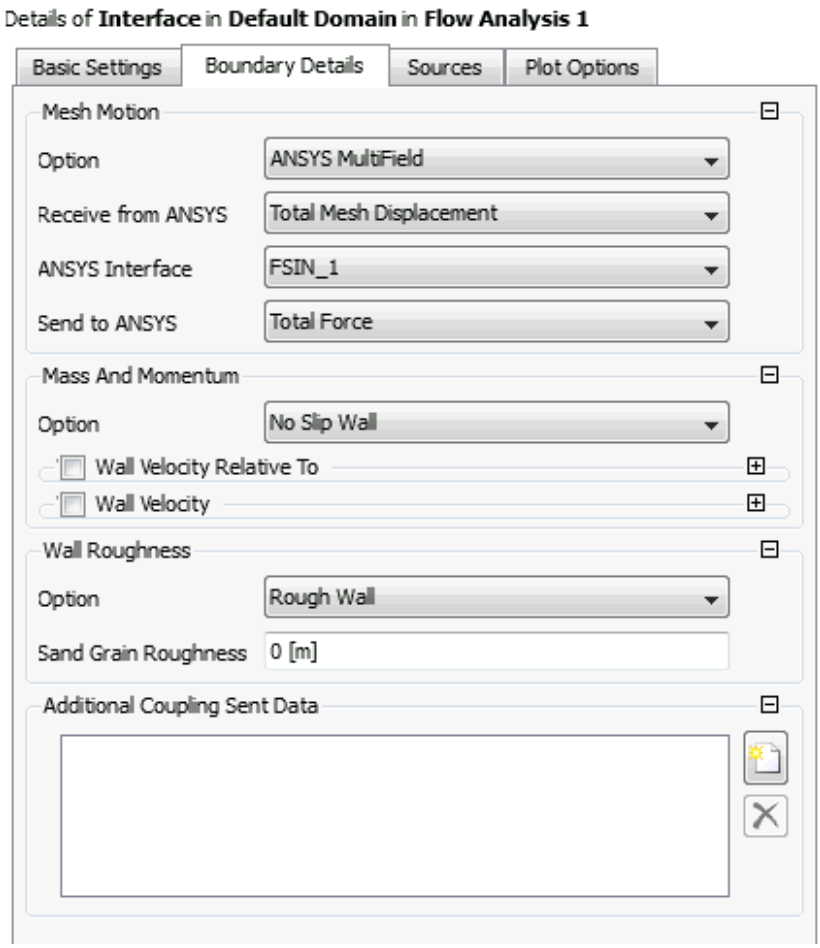

Figure 76. CFX-Pre Interface FSIN Assignment.

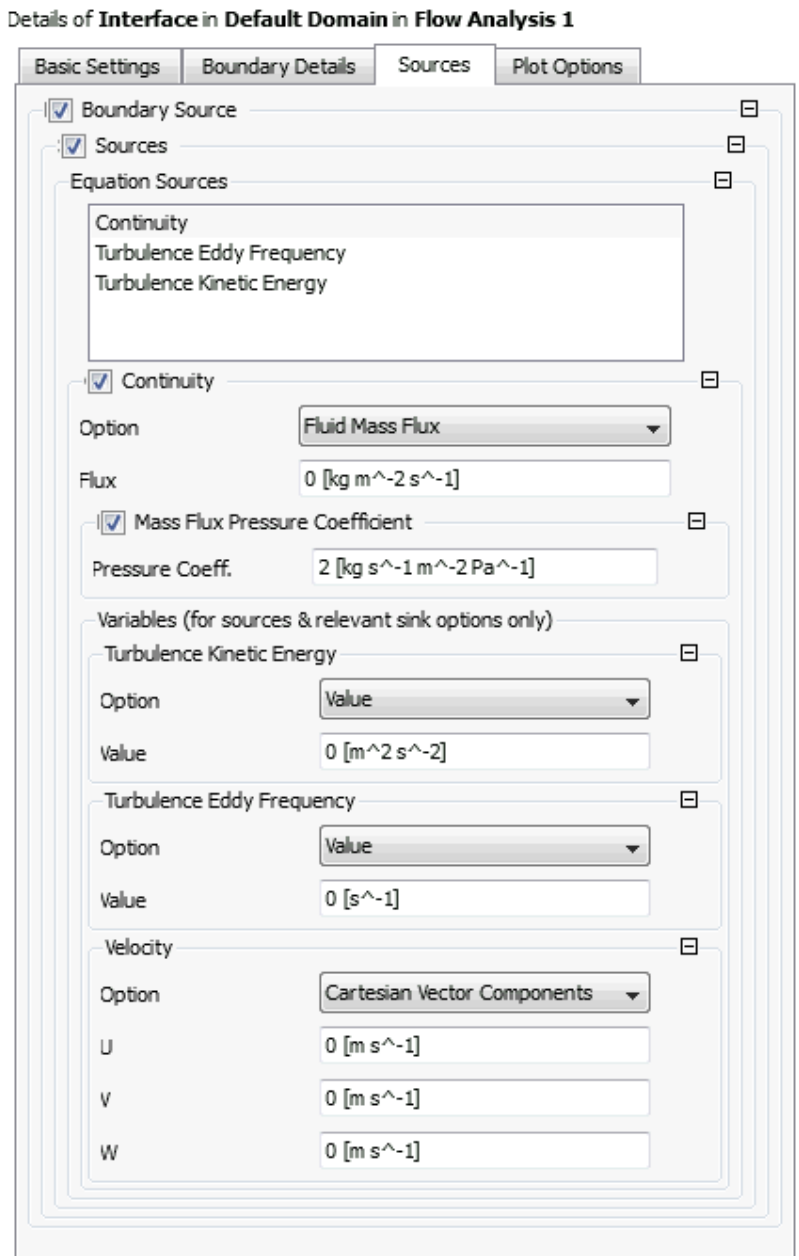

Figure 77. CFX-Pre Interface Pressure Coefficient Setting.

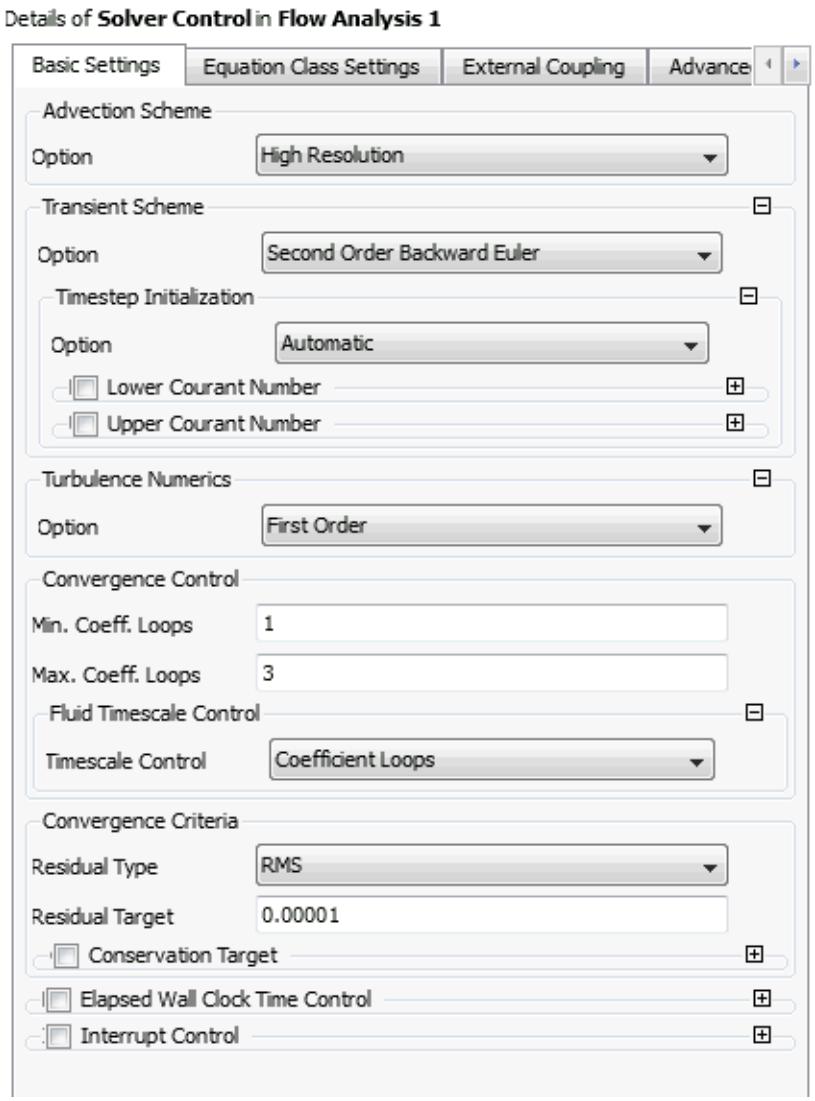

Figure 78. CFX-Pre Solver Control Settings.

APPENDIX C. SOLVING FSI SIMUATIONS WITH HPC

A. HPC AND CPU COMPARISON

Within ANSYS Workbench, analysis systems are each provided with their own solver; however, unique to FSI simulations, the independent structural solver is rendered obsolete and can be deleted from the project schematic [5]. The embedded solver within the Workbench CFX Solution cell completes the entire solution process and facilitates single-source results processing with CFX Post.

ANSYS simulations requiring FSI alternate solution data between fluid and structural domains and therefore solver run times are not necessarily dependent upon the ability to solve the mathematical problem, but rather the ability to transfer solved data between domains. The data transfer of a 12-core node on HPC proved faster than an 8-core CPU with solver run times of 16 and 24 hours respectively. However, the largest difference between HPC and CPU was most evident during post processing. ANSYS structural results are written to a single (.rst) file that averaged 2 GB for this simulation and had to be loaded in entirety for post processing in CFX-Post. The HPC node was significantly faster at loading this file than the CPU.

B. SUBMITING ANSYS SIMULATIONS WITH FSI TO HPC

Completion of an FSI simulation on HPC required use of Data (.dat) and Definition (.def) files that must be generated and copied from the correct ANSYS folder within workbench. After an ANSYS Workbench project is created and saved an additional folder (_files) is created. The Data and Definition files are located in the *Base_Model_file\dp0\CFX\CFX* subfolder. The data file contains mesh data and the Definition file stores Structural and CFX settings. The Definition file fully defines requirements for both Structural and CFX simulation components and in this application is only written after the Solver Manager is started from Workbench. Once Data and Definition files are available, they must be copied to HPC using WinSCP, which creates an interface between the local Windows operating system and HPC Linux based

operating system (Figure 79). The left side of the screen shows sample files from the local CPU while the right side shows the necessary file copied to the HPC Linux-based directory.

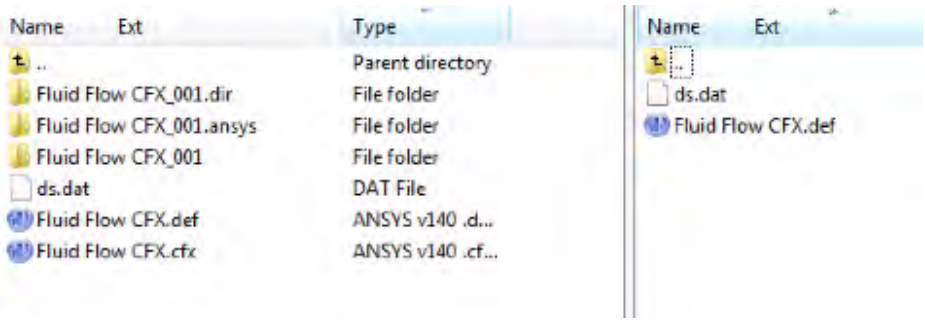

Figure 79. WinSCP Directory.

The last file necessary for solving an FSI simulation on HPC is a script (.sh) file that directs HPC to create a node for the solver to run in (Figure 80). The script file contains the commands that HPC will execute and must be tailored to suit each type of ANSYS workflow. In this case, the command to start both CFX and ANSYS (Structural) solvers is required [6]. The script also identifies the source directory and names of the Data and Definition files. The script file is a text document that can be edited directly from WinSCP and the only additional constraint is that it must be located in the same HPC directory as the Data and Definition files. McCormick's [13] thesis provides additional information on the contents of the script file, specifications about ANSYS licensing and commonly used Linux commands for HPC.

```
#!/bin/bash
# PBS cfx job submission script

#PBS -j oe
#PBS -l walltime=5:00:00:00
#PBS -l nodes=1:ppn=12
#PBS -l pmem=6GB
#PBS -m e
#PBS -M my email address
#$ -N Base_Model

#
# echo some parameters
#
echo " "
echo "hostname = `hostname`"
echo "PBS_NODEFILE = $PBS_NODEFILE"
echo "JOB_ID = $JOB_ID"
echo "PBS_O_WORKDIR = $PBS_O_WORKDIR"
echo " "
echo "PBS_NODEFILE contents:"
echo "--------------------"
cat $PBS_NODEFILE
echo "--------------------"
echo " "

source /etc/profile
module load app/ansys
module load compile/gcc
export CFX5RSH=ssh
cd $PBS_O_WORKDIR


# Create hosts list

# echo par-dist = $(cat $PBS_NODEFILE)

PAR_LIST=$(sed -e '{:q;N;s/\n/,/g;t q}'  $PBS_NODEFILE)

#
# run the cfx job
#
cfx5solve -batch -def Fluid_Flow_CFX.def -par-dist $PAR_LIST -mfx-run-mode
"Start ANSYS and CFX" -ansys-input ds.dat
```

Figure 80. Example Script File.

The final step prior to submitting the script file is reassignment of the Data file. As shown in Figure 75, the Data (ds.dat) file is automatically located when running the solver from Workbench, however when the files are moved to HPC the source location path is lost and must be redefined. To accomplish this, an X-Win32 session is opened

and CFX-Pre is launched from a new HPC node as described by McCormick [13]. Once in CFX-Pre, selecting the appropriate definition file opens an existing case. The Data file is then edited from within the Analysis Type field in the navigation pane.

Once Data, Definition and Script files are properly configured and stored in a common directory, the job is ready to be submitted. From X-Win32 the change directory command (cd) is used to navigate to the desired directory that stored the three files. The job is sent to HPC using the submit command (qsub) followed by the script file name including its file type extension.

A completed job generates a Results (.res) file and two folders with .ansys and .dir extensions (Figure 79). These files and folders store all the necessary information for post processing with CFX Post. The Results file stores CFX data for the final time step while all other CFX time step results are stored as Transient (.trn) files in the .dir folder. Loading the Results file from the Load Results option in CFX Post automatically loads all transient files as well. Structural results for all time steps are stored as a single Result (.rst) file located in the .ansys folder and are loaded similar to CFX results.

APPENDIX D. DEPTH VARIATION, NODAL DATA UPPER-MID, CENTER, LOWER-MID, AND LOWER

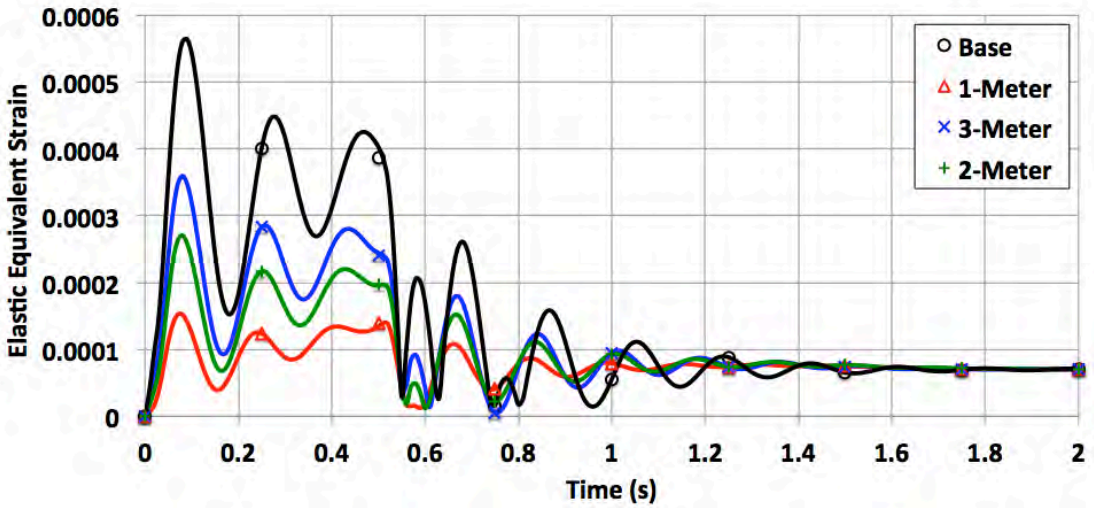

Figure 81. Depth Variation, Strain at Upper-Mid Node.

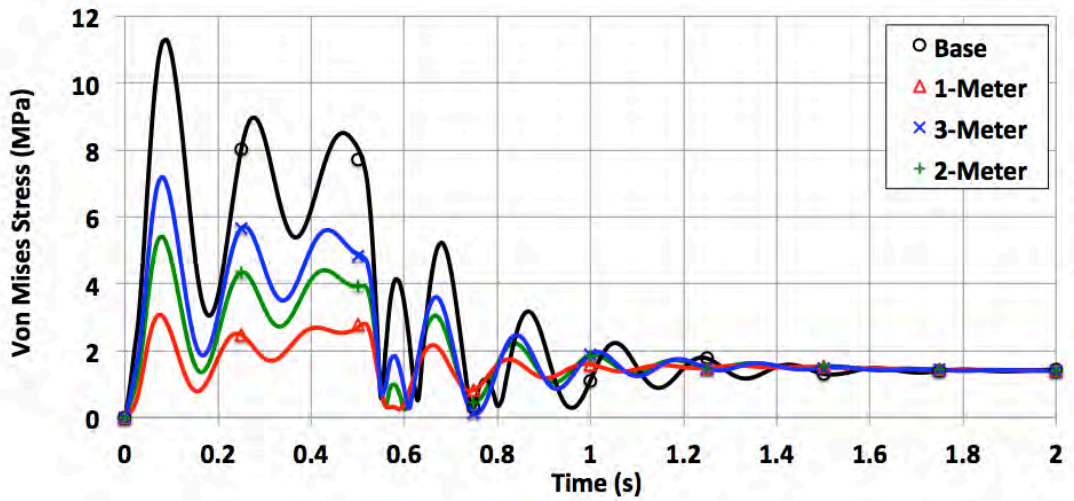

Figure 82. Depth Variation, Stress at Upper-Mid Node.

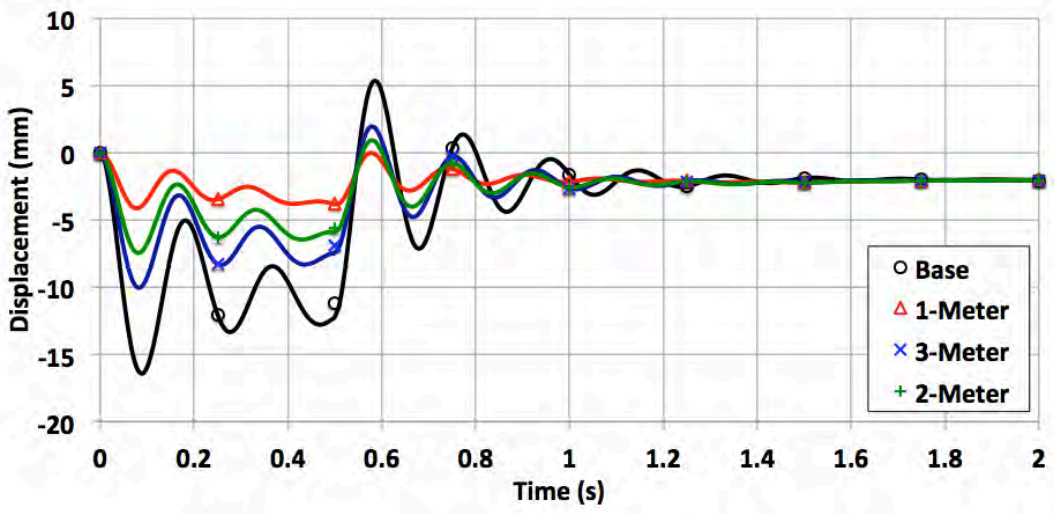

Figure 83. Depth Variation, Displacement at Upper-Mid Node.

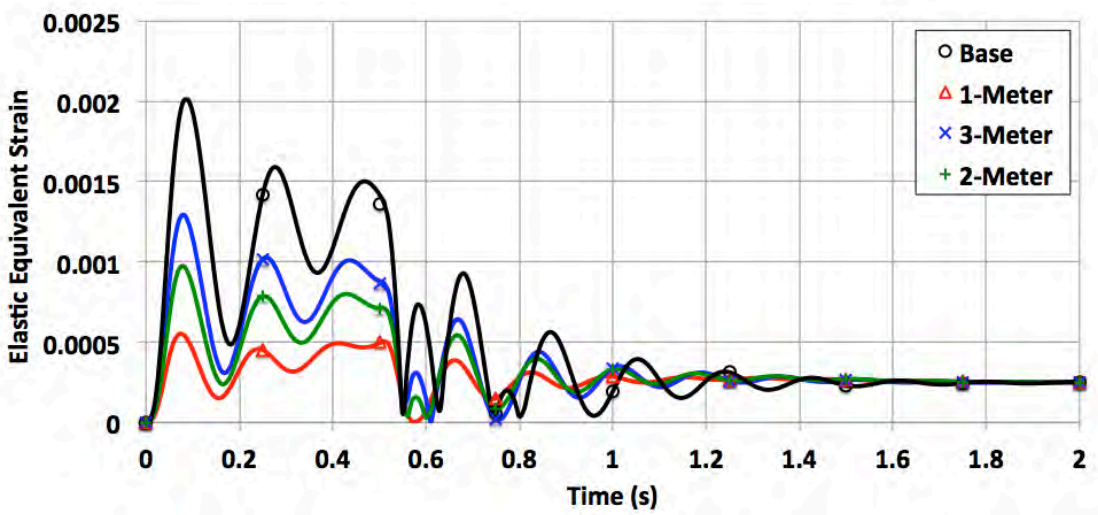

Figure 84. Depth Variation, Strain at Center Node.

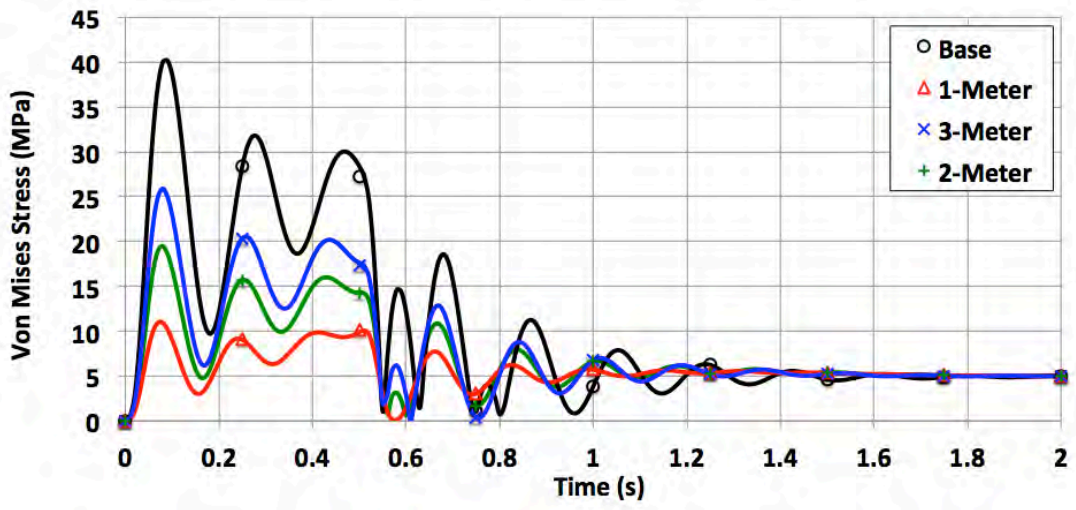

Figure 85. Depth Variation, Stress at Center Node.

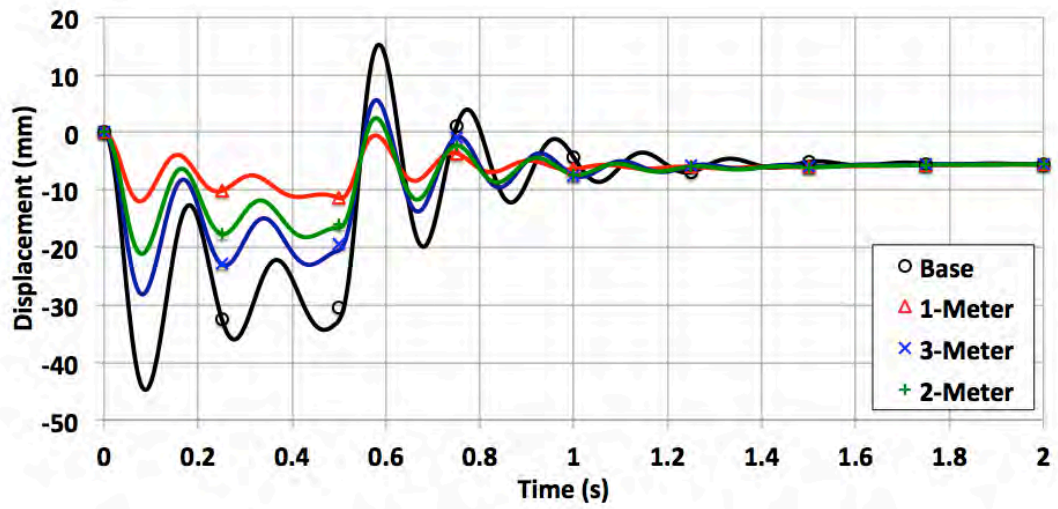

Figure 86. Depth Variation, Displacement at Center Node.

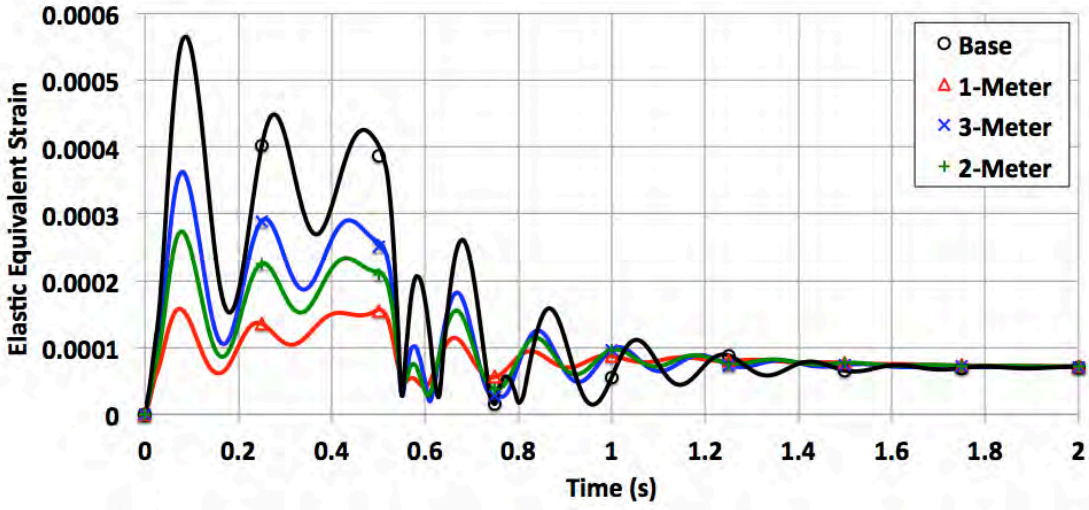

Figure 87. Depth Variation, Strain at Lower-Mid Node.

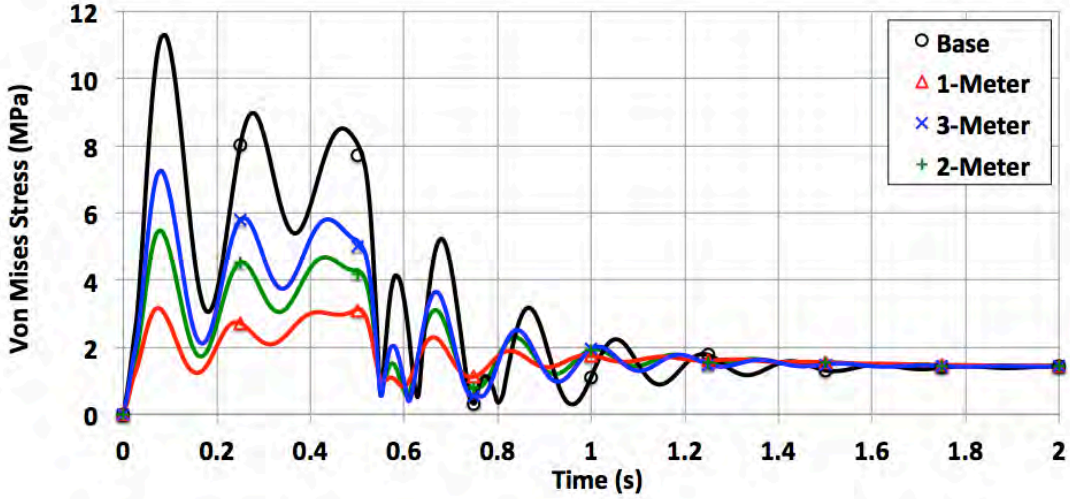

Figure 88. Depth Variation, Stress at Lower-Mid Node.

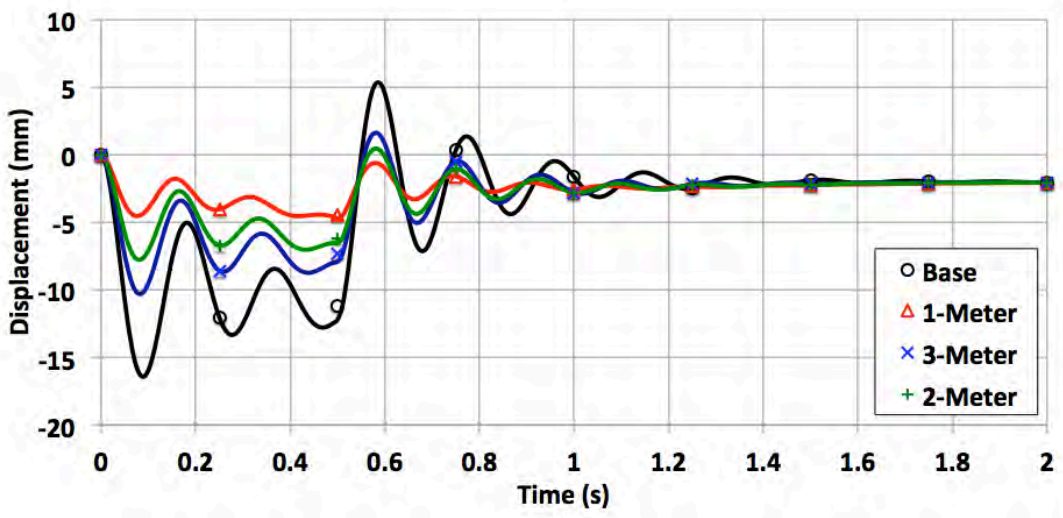

Figure 89. Depth Variation, Displacement at Lower-Mid Node.

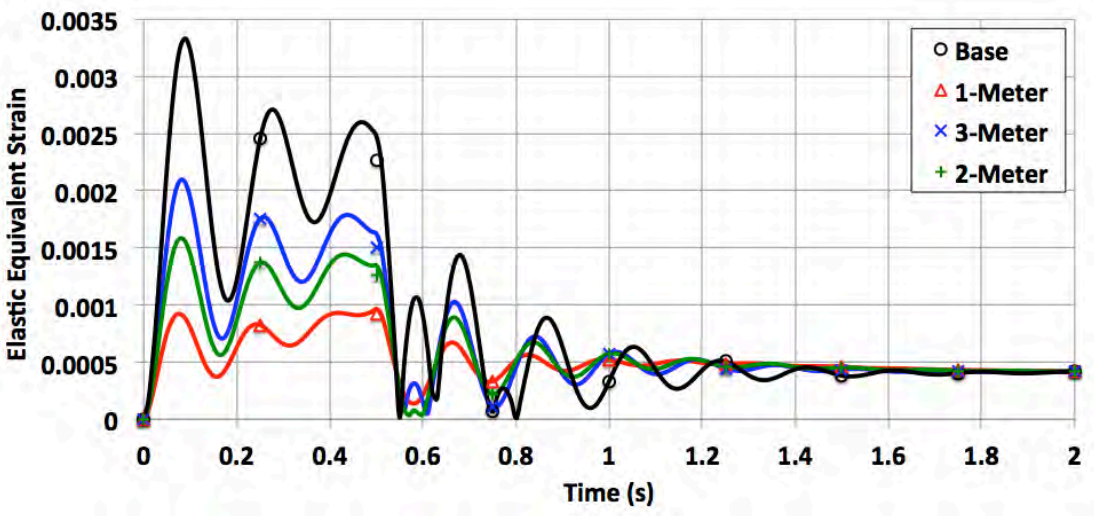

Figure 90. Depth Variation, Strain at Lower Node.

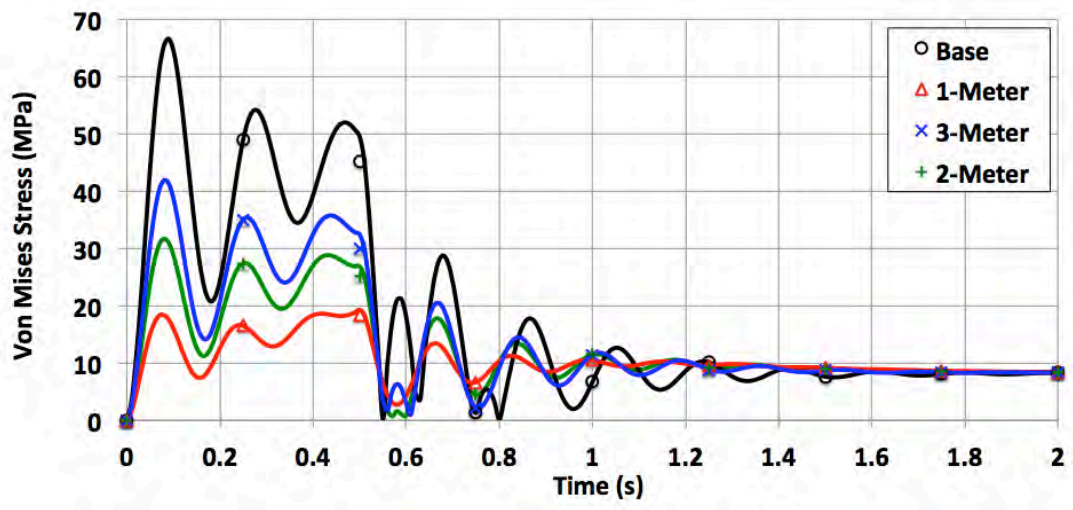

Figure 91. Depth Variation, Stress at Lower Node.

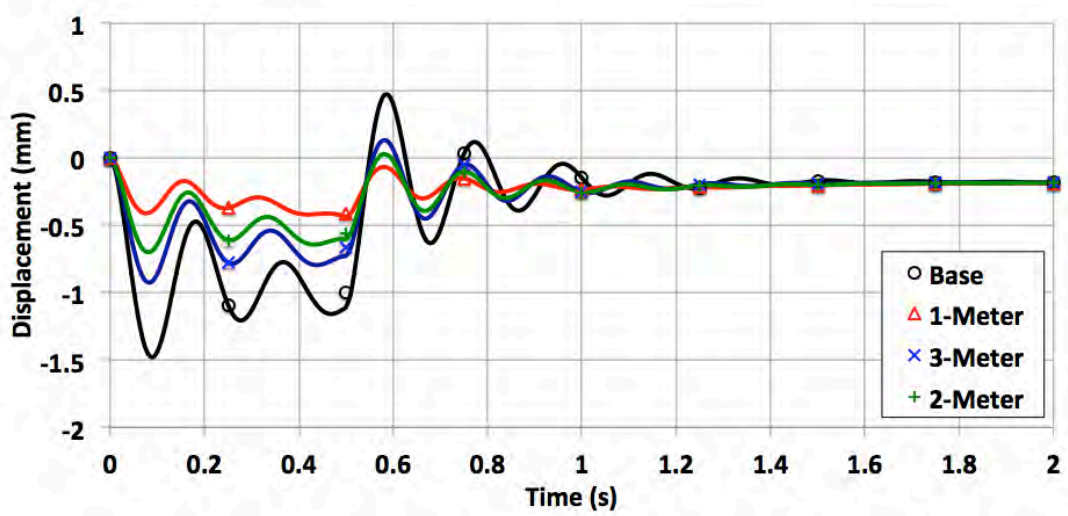

Figure 92. Depth Variation, Displacement at Lower Node.

Table 15. Depth Variation, Upper Node Case Summary.

	Base	1-Meter	2-Meter	3-Meter
	Elastic Equivalent Strain			
Max	0.003328	0.000829	0.001508	0.002033
Steady State	0.000409	0.000412	0.000418	0.000414
Ratio	8.12	2.01	3.61	4.91
	Von Mises Stress (MPa)			
Max	66.6	16.6	30.2	40.7
Steady State	8.2	8.2	8.4	8.3
Ratio	8.12	2.01	3.61	4.91
	Displacement (mm)			
Max	1.477	0.363	0.660	0.891
Steady State	0.181	0.182	0.184	0.181
Ratio	8.18	2.00	3.60	4.91

Table 16. Depth Variation, Upper-Mid Node Case Summary.

	Base	1-Meter	2-Meter	3-Meter
	Elastic Equivalent Strain			
Max	0.000564	0.000015	0.000270	0.000359
Steady State	0.000070	0.000070	0.000070	0.000070
Ratio	8.02	2.16	3.82	5.11
	Von Mises Stress (MPa)			
Max	11.3	3.0	5.4	7.1
Steady State	1.4	1.4	1.4	1.4
Ratio	8.02	2.16	3.82	5.11
	Displacement (mm)			
Max	16.408	4.121	7.446	10.021
Steady State	2.025	2.039	2.054	2.035
Ratio	8.10	2.02	3.62	4.92

Table 17. Depth Variation, Center Node Case Summary.

	Base	1-Meter	2-Meter	3-Meter
	Elastic Equivalent Strain			
Max	0.002008	0.000547	0.000974	0.001294
Steady State	0.000248	0.000251	0.000252	0.000249
Ratio	8.09	2.18	3.87	5.19
	Von Mises Stress (MPa)			
Max	40.1	10.9	19.5	25.9
Steady State	5.0	5.0	5.0	5.0
Ratio	8.09	2.18	3.87	5.19
	Displacement (mm)			
Max	44.700	11.926	21.134	28.149
Steady State	5.538	5.631	5.634	5.584
Ratio	8.07	2.12	3.75	5.04

Table 18. Depth Variation, Lower-Mid Node Case Summary.

	Base	1-Meter	2-Meter	3-Meter
	Elastic Equivalent Strain			
Max	0.000564	0.000157	0.000274	0.000363
Steady State	0.000070	0.000072	0.000072	0.000071
Ratio	8.03	2.17	3.79	5.09
	Von Mises Stress (MPa)			
Max	11.3	3.1	5.5	7.2
Steady State	1.4	1.4	1.4	1.4
Ratio	8.03	2.17	3.79	5.09
	Displacement (mm)			
Max	16.412	4.698	7.777	10.294
Steady State	2.025	2.100	2.074	2.050
Ratio	8.10	2.24	3.75	5.02

Table 19. Depth Variation, Lower Node Case Summary.

	Base	1-Meter	2-Meter	3-Meter
	Elastic Equivalent Strain			
Max	0.003329	0.000965	0.001583	0.002095
Steady State	0.000410	0.000426	0.000422	0.000417
Ratio	8.12	2.26	3.75	5.02
	Von Mises Stress (MPa)			
Max	66.6	19.3	31.7	41.9
Steady State	8.2	8.5	8.4	8.3
Ratio	8.12	2.26	3.75	5.02
	Displacement (mm)			
Max	1.477	0.436	0.699	0.923
Steady State	0.180	0.188	0.186	0.183
Ratio	8.18	2.31	3.76	5.03

THIS PAGE INTENTIONALLY LEFT BLANK

LIST OF REFERENCES

[1] Schoenster, B., Michaud, K., "LCS Program Overview," *Navy Industry International Dialogue (NIID) Program Meeting*, Washington, D.C., November 6, 2008.

[2] Lee, H., *Finite Element Simulations with ANSYS Workbench 14*, Mission, KS: SDC Publications, 2012.

[3] Tehrani, K., Rakheja, S., Sedaghati, R., "Analysis of the overturning moment caused by transient liquid slosh inside a partially filled moving tank," Proceedings of the Institution of Mechanical Engineers, Part D, *Journal of Automobile Engineering* 220: 289, March 2006.

[4] Battley, M., Allen, T., Perhson, P., Senious, I., Rosen, A., "Effects of panel stiffness on slamming responses of composite hull panels," KTH Centre for Naval Architecture, Stockholm, Sweden, 2009

[5] ANSYS, *ANSYS 14.0 CFX Tutorials*, release 14. Canonsburg, PA: ANSYS, 2011, pp 419–438.

[6] ANSYS, *ANSYS CFX-Solver Manager User's Guide*, release 14. Canonsburg, PA: ANSYS, 2011, pp 123–135.

[7] Bryan, G., "Experimental and computational fluid dynamic analysis of axial-flow hydrodynamic power turbine," M.S. thesis, Dept. Mech. Areosp. Eng., Naval Postgraduate School, Monterey, CA, 2013.

[8] Millhouse, S., "Structural forces experienced by a Flat Plate in Transient Flow," M.S. thesis proposal, Dept. Mech. Areosp. Eng., Naval Postgraduate School, Monterey, CA, forthcoming.

[9] Frank M. White, Fluid Mechanics, 7th ed., New York: McGraw-Hill Science/Engineering/Math, 2010.

[10] Sun, X., "Numerical and experimental investigation on tidal and current energy extraction," Ph.D. dissertation, University of Edinburgh, United Kingdom, 2008.

[11] ANSYS, *ICEM CFD Help Manual*, release 14. Canonsburg, PA: ANSYS, 2011, pp 13–30.

[12] ANSYS, *ANSYS CFX-Pre User's Guide*, release 14. Canonsburg, PA: ANSYS, 2011, pp 177–180.

[13] McCormick, M., “Experimental and computational modeling of an axial transonic compressor with inlet guide vanes,” M.S. thesis, Dept. Mech. Areosp. Eng., Naval Postgraduate School, Monterey, CA, 2013.

INITIAL DISTRIBUTION LIST

1. Defense Technical Information Center
   Ft. Belvoir, Virginia

2. Dudley Knox Library
   Naval Postgraduate School
   Monterey, California